Distribution Agreement

In presenting this thesis or dissertation as a partial fulfillment of the requirements for an advanced degree from Emory University, I hereby grant to Emory University and its agents the non-exclusive license to archive, make accessible, and display my thesis or dissertation in whole or in part in all forms of media, now or hereafter known, including display on the world wide web. I understand that I may select some access restrictions as part of the online submission of this thesis or dissertation. I retain all ownership rights to the copyright of the thesis or dissertation. I also retain the right to use in future works (such as articles or books) all or part of this thesis or dissertation.

Signature:

_____

Bryant Chica Date

Semiconductor Nanoparticle-Protein Hybrid Systems for Solar Hydrogen Production and Photo-Triggered Mechanistic Studies

By
Bryant Chica
Doctor of Philosophy
Chemistry

Dr. R. Brian Dyer, Advisor

Dr. Francesco Evangelista, Committee Member

Dr. Cora MacBeth, Committee Member

Accepted

Dr. Lisa A. Tedesco
Dean of the James T. Laney School of Graduate Studies

Date

Semiconductor Nanoparticle-Protein Hybrid Systems for Solar Hydrogen Production and Photo-Triggered Mechanistic Studies

By
Bryant Chica

Advisor: Dr. R. Brian Dyer

An abstract of
A dissertation submitted to the Faculty of the
James T. Laney School of Graduate Studies of Emory University
in partial fulfillment of the requirements for the degree of
Doctor of Philosophy
in Chemistry
2017

Semiconductor Nanoparticle-Protein Hybrid Systems for Solar Hydrogen Production and Photo-Triggered Mechanistic Studies

By Bryant Chica

We describe a hybrid photocatalytic system for hydrogen production consisting of nanocrystalline CdSe/CdS dot-in-rod (DIR) structures coupled to [NiFe] soluble hydrogenase I (SHI) from *Pyrococcus furiosus*. Electrons are shuttled to the catalyst by a redox mediator, either methyl viologen (MV^{2+}, E_0 = -446 mV vs. NHE) or propyl-bridged 2-2'-biyridinium (PDQ^{2+}, E_0 = -550 mV vs. NHE). H_2 production in the PDQ^{2+} system is highly efficient, with an internal quantum efficiency (IQE) as high as 77% and a TON_{SHI} of 1.1 x 10^6 under mild (RT, pH = 7.35) conditions. Detailed characterization reveals the mechanisms responsible for such high efficiencies. The high efficiency and robustness of this system enabled its use as a novel methodology for photo-triggering SHI reactivity and enabling time resolved and steady-state spectroscopic studies of the SHI active site. This enabled reproduction of previously reported active site dynamics through laser initiated chemical potential jump studies on the SHI active site. It also provided a novel method to gain insight into the reductive reactivation of the aerobically inactivated enzyme and the nature of the inactive states by systematically lowering the solution reduction potential in "light titrations". We thus establish nanocrystalline semiconductor nanostructures as powerful tools to study redox enzymes and potentially more general catalyst systems.

Semiconductor Nanoparticle-Protein Hybrid Systems for Solar Hydrogen Production and Photo-Triggered Mechanistic Studies

By
Bryant Chica

Advisor: Dr. R. Brian Dyer

A dissertation submitted to the Faculty of the
James T. Laney School of Graduate Studies of Emory University
in partial fulfillment of the requirements for the degree of
Doctor of Philosophy
in Chemistry
2017

Acknowledgements

First and foremost, I would like to thank my advisor, Dr. Brian Dyer for sticking with me, encouraging and believing in me through the ups and downs of my graduate career. A combination of insightful advice and guidance and an environment of intellectual freedom and independence; the ability to follow my curiosity, to explore, discover, and pursue new, risky, ideas have shaped me into the scientist I am today. For this I am very grateful and indebted to him.

I would also like thank all the other professors who have provided guidance and inspiration throughout my graduate career; Michael Heaven, Emily Wienert, Chris Scarborough, Tim Lian, Craig Hill, Francesco Evangelista and Cora Macbeth. My academic experience would have been much impoverished without you all there to guide me.

I would also like to thank my parents, Jorge and Elia, for their unwavering support and guidance throughout my life. I would truly be nowhere without you and I am eternally grateful for all you have done and continue to do for me. I would like to thank my wonderful wife Rini for being there with me through this process. To my siblings, Yvette and Daniel, who have been a constant source of inspiration for me, I am proud of you guys and thankful you are in my life. I must also thank Daniel for his synthetic work in creating a novel catalytic material for hydrogen evolution which is an ongoing collaboration and my brother-in-law, Ben, for his help and guidance in my forays into computational chemistry.

I also thank my coworkers and friends at Emory who have been there with me through my graduate career; Gokul Raghunath, Erin Schuler, Rolando Rengifo, Gregory Karahalis, Donny Magana, Brandon Greene, Dongmei Xiang, Brooke Andrews, Micah Eller, Yuhgene Liu, Kevin Yehl and many others have been like a family away from home and the source of much merriment, intellectual stimulation and collaboration.

I would also like to thank our collaborators from the University of Georgia, Dr. Michael W.W. Adams and Chang-Hao "Perry" Wu for providing me with copious amounts of valuable enzyme without which many of the studies detailed in this document would be completely impossible. Also Dr. Ekaterina Pletneva and her student Jie Gu for providing the cytochrome c mutants that made some of this work possible.

I would also like to thank and remember those friends who have touched my life in some way but have left this world behind; Mark Nichols and Christopher France, the world is poorer without you guys laughing in it. You will be missed but not forgotten.

I am eternally grateful you all for the parts you have played in shaping me into the scientist and person I am today and helping me in this journey.

Table of Contents

List of Figures

Chapter 4

Chapter 5

List of Tables

Chapter 3

Chapter 1

Introduction

1.1 - Climate Change, Clean Energy and Solar Fuels

For the past several hundred years, fossil fuels have provided the paradigm to bring human civilization into the modern industrial age that elevated the living standards of billions of human beings.[1] Continual emission of carbon dioxide from the burning of fossil fuels has contributed to increasing the CO_2 content of the atmosphere from below 300 ppm to above 400 ppm currently which has been a primary contributor to global climate change[2]. The growing consensus in the scientific community is that lowering of emissions and significant progress towards sustainability in global energy production, large scale industry, land use and transport is necessary on a sub-decade timescale to avert unacceptable risk of worst case climate scenarios and their consequences for human civilization[3].

The solar flux at earth's surface is approximately 1000 W/m^2, totaling $1.75x10^5$ TW, greatly exceeding global energy demand of 15TW[1]. This incoming UV and visible radiation is subsequently transformed in a few distinct ways. It may impinge upon the ground where it is either scattered or absorbed and converted to electronic excitations which are ultimately thermalized and reemitted to space as infrared photons with a higher entropy content. Alternatively, these high-energy photons may be captured by a photosynthetic apparatus and their energy used to produce charge separated states capable of charge transport to a catalytic center, ultimately supporting biomass synthesis and sustaining of life. Capturing and converting even a small fraction of this incident light to a form suitable for powering human activities provides a clear path to reduce and eliminate the need for burning fossil fuels to power human civilization.

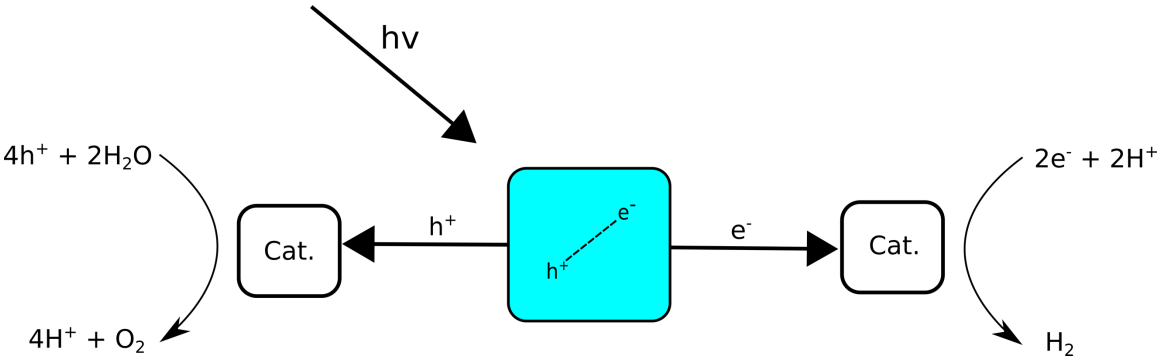

Scheme 1.1 –Architecture required for a solar fuel generating device. A central module for light harvesting and charge separation. Transport of separated electrons (e^-) and holes (h^+) to catalytic centers where substrates (protons (H^+) and water) are transformed to products (hydrogen and oxygen). Note: the overall chemical reaction is not balanced here. The cathodic reaction on the right has a 2:1 stoichiometric ratio to the anodic reaction on the left.

Photovoltaic technology represents a rapidly growing method of harvesting renewable solar energy. Rapidly falling solar panel prices are contributing to increasingly rapid adoption of this technology. Adoption of this method for all energy usage is challenged by the intermittency of the solar flux and it's mismatch with peak load times of the electric grid. While the solar flux peaks at noontime, peak demand of electricity occurs in the evening when the sun is setting. Some progress in mitigating these shortcomings through improvement and implementation of technology for Li-ion battery based grid-scale and end user level electricity storage has been seen recently.[4] Recent years have also seen increasing public interest and penetration of electric car technology although some of the most emissions intensive automobile activities such as long haul

trucking may still require further advancement in battery energy density to become competitive with chemical fuels.[5]

The mismatch between availability and demand with solar energy can be mitigated with the development of viable methods for storage of solar energy. The most obvious option for solar energy storage is charging and discharging of batteries. Battery technologies, however, suffer from comparatively low energy densities with state of the art Li-ion cells achieving energy densities of 250 Wh/kg. An alternative approach is to store energy in the chemical bonds of a fuel. In contrast to batteries, high octane gasoline has an energy density of 12,883 Wh/kg and hydrogen gas boasts an impressive 39,443 Wh/kg. This motivates approaches for using solar photons to directly synthesize chemical fuels which could provide carbon neutral fuels through water splitting to H_2 or CO_2 reduction to produce hydrocarbons.

Viability of solar approaches to generating chemical fuels depends on optimization of several independent modules[1] as depicted in Scheme 1. First, the central module represents a system for efficient light harvesting and charge separation. Those separated charges must then be transported to an appropriate catalyst to be consumed in driving the desired fuel forming half reactions and regenerate the original state of the system. Optimization of each of these modules represents a vast research enterprise spanning many years of effort.

Driving proton reduction with light is one area that has received much attention over the years[6] especially in the use of biomimetic molecular systems. While much progress has been made in identifying viable and abundant catalysts for proton reduction[7] and water oxidation[8] much progress is still required to improve the stability, performance

and scalability of these technologies[9] and related problems such as hydrogen storage and fuel cell technologies. We thus set out to explore the design of a photocatalytic system based on a member of the set of the best catalysts known for hydrogen production and oxidation: Hydrogenases.

1.2 - Hydrogenases

1.2.1 - Hydrogenases in Photocatalytic Hydrogen Production

Synthetic chemistry has very fruitfully relied on biomimetic approaches to hydrogenase in the rational design of molecular and heterogeneous catalysts for proton reduction.[7, 10-11] Hydrogenases themselves have also shown success in being incorporated into systems for light driven proton reduction[12-15] generally outperforming their synthetic counterparts[16]. However, photosensitized systems with hydrogenases as catalysts have ultimately not been able to achieve very high quantum efficiencies (QE) of hydrogen generation[12-15] with the peak QE being ~20% with a CdS nanorod sensitized [FeFe] Hydrogenase system. In contrast, some nanoparticle/noble metal catalyst heterostructures have achieved near unity quantum yield of hydrogen produced.[17] It is an important goal of research in this area to not only design systems that can achieve high quantum efficiencies of hydrogen generation, but to carry out detailed physical characterization of these systems and to discover where are the bottlenecks in efficiency. For the kinds of systems discussed above, particularly the hydrogenase based systems of primary interest here, there have been reports of photocatalytically active sacrificial systems of varying efficiencies, but characterization of the detailed processes involved has often been limited.

Themes have begun to emerge in these the factors governing the efficiency of sacrificial model systems for hydrogen production. Of primary importance is the removal of holes from the sensitizer[18-19] to regenerate the ground state faster than the electron transfer event, especially if the product of electron transfer retains strong coupling for charge recombination as in the case of metal nanoparticles grown on semiconductors.[19] An important design consideration in photochemical fuel production and any system for efficient energy conversion is the shaping of the potential energy landscape experienced by photo excited charge carriers. Charge transfer events from one site to another are driven by changes in Gibbs free energy (1) between the two states and are required to be exergonic ($\Delta G^0 < 0$).

(1) $\Delta G^0 = \Delta H^0 - T\Delta S^0$

This charge transport provides the spatial separation of charges critical to preventing charge recombination and preserving high efficiencies. Even so, a balance must be struck between the use of the available free energy to do the work of charge separation versus preserving enough free energy in the charge carriers to effectively drive catalysis in the desired direction. We still require the invention of novel schemes and a refinement in the understanding of effective ways of shaping the energy landscape in light harvesting systems[20] in order to maximize the funneling of the available free energy towards the desired productive processes. This goal requires thermodynamically efficient and fast catalysts and rational design of the photocatalytic systems to embed them in favorable energetic landscapes.

1.2.2 - Hydrogenase Mechanism

Hydrogenases (H_2ases) are metalloenzymes that catalyze the reversible interconversion of protons and electrons to dihydrogen (2).[21]

(2) $2H^+ + 2e^- \leftrightharpoons H_2$

They perform this reaction at specialized Ni and Fe containing active sites buried deep inside the hydrophobic protein interior. Two main classes of H_2ases exist, which are differentiated by their active site metal content. The so called [FeFe] enzymes don't contain nickel, rather they have a binuclear iron active site ligated by CN^- and CO ligands and a unique bridging azadithiolate ligand critical for proton transfer at the active site.[10, 22] The [NiFe] H_2ases harbor a heterobimetallic active site containing Ni and Fe where the Fe is ligated by one CO and two CN^- ligands and the Ni site is ligated by four cysteine thiolates, two of which are bridging to the Fe, in a distorted square pyramidal motif. Electrons are shuttled to and from the active site via a chain of iron sulfur clusters[23] to the protein surface where they may exchange with physiological redox partners, mediator molecules or an electrode via interfacial electron transfer. Protons are delivered to the active site by a network of ionizable amino acid side chains and structural waters within the protein.[24]

The catalytic mechanism of H_2ases has been the subject of intense interest and study[25-30] to understand how base metals such as Fe and Ni can be harnessed to achieve catalytic performance rivaling that of platinum. The catalytic mechanism of hydrogenase has been extensively characterized and a generally agreed upon outline of the mechanism has emerged in the literature.[21, 26, 29] This mechanism of proton reduction and hydrogen oxidation is sketched out in Scheme 1.2. The naming scheme refers to the original

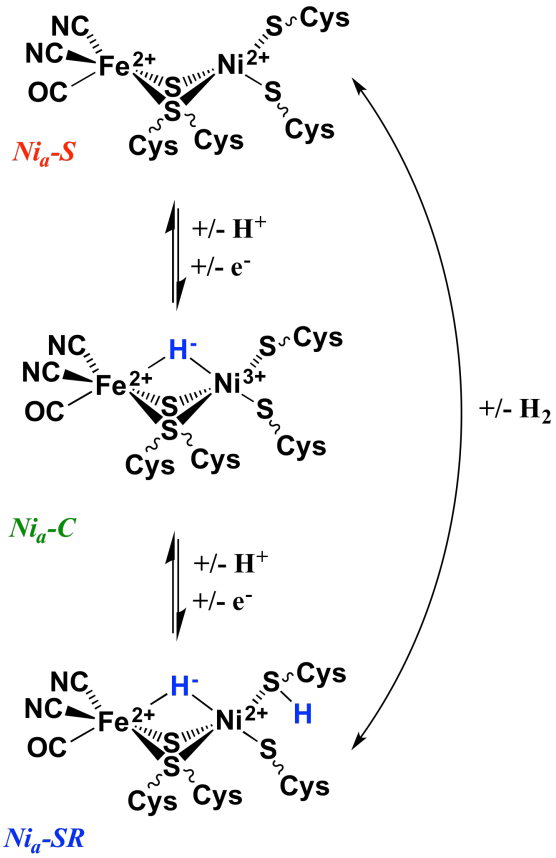

Scheme 1.2 – Elementary catalytic cycle of hydrogen production and oxidation in [NiFe] Hydrogenases.

description of these states as identified by EPR spectroscopy[21] where "S" designates EPR silent divalent nickel states. The most oxidized state in the cycle, Ni-S, is reduced and protonated in a concerted PCET process[29] leading to the formation of Ni-C with a bridging hydride and a formally trivalent nickel center. Subsequent reduction and protonation leads to the formation of Ni-SR, the most reduced catalytic intermediate, which is primed for H_2 formation and release with a very basic hydride and a protonated cysteine ligand. Hydrogen oxidation proceeds in the reverse direction along this pathway beginning with dihydrogen approach to the Ni-S state where it is heterolytically cleaved to a hydride and a proton, yielding the Ni-SR state. More detailed aspects of the mechanism, such as whether the heterolytic cleavage of dihydrogen proceeds via a

frustrated Lewis pair mechanism[26] with a preserved arginine residue near the active site or via formation of a transient Fe-H_2 or Ni-H_2 intermediate[31] are still the subject of much debate and ongoing investigations by various groups.

1.2.3 Catalytic Bias in Hydrogenases

The function of a catalyst in a chemical reaction is to lower the activation barrier(s) for a reaction to accelerate the kinetics of that transformation without altering the thermodynamic characteristics of that process. An ideal catalyst therefore should not have any inherent preference for the direction in which a chemical transformation proceeds. In the hydrogenase systems, however, a directional preference is often observed which is termed a catalytic bias. From the perspective of voltammetry this phenomenon manifests as significant deviations from unity of the proton reduction to hydrogen oxidation current ratio.[32-33] Catalytic bias is thought to emerge from two distinct factors. The first of these is the kinetic influence of rate limiting steps occurring remote from the catalytic active site.[33] These steps can have altered rate limiting character depending on the direction of catalysis. For example, in [NiFe] H_2ases, product release is thought to be rate limiting for proton reduction. This is related to the strong product inhibition by H_2 observed in these enzymes: once the Ni-SR state evolves H_2 the nascent oxidized Ni-S state is primed to rebind H_2 until it diffuses away from the active site. Thus, altering the rate of product release through mutations around the gas channel through which H_2 escapes presumably permitted the tuning of the catalytic bias. This factor can only operate in the case where, under the conditions that drive the reverse reaction, a distinct rate limiting step dominates the rate. For H_2 oxidation this is thought

to become electron transfer rather than product release.[33] This method can be thought of as simply alleviating or enhancing the strong product inhibition observed in NiFe H_2ases. The second factor controlling the bias is considered to be the most important in determining this property. H_2ases are not defined by their catalytic active sites alone. They are electronically coupled to the outside environment through chains of FeS clusters of varying size and complexity with well-defined redox properties of their own.[21] The redox states of these FeS cofactors control the redox potential that the active site "sees" and thus the availability of electrons at the active site for productive catalysis.[28, 34-35] The energetic landscape of the FeS electron transfer chain dictates the directionality along which electron flow is energetically favorable and thus the directional bias of catalysis. Such energetics are evident, for example, in the [FeFe] H_2ase from *Clostridium pasteurianum*, where the distal FeS cluster has a quite negative reduction potential (-450 mV vs NHE) which favors subsequent reduction of the more positive accessory FeS clusters and the catalytic H-cluster, biasing the enzyme towards proton reduction.[36]

These biological machines make clear that shaping the energetic landscape around the catalytic center is critical for effective catalysis. This is even more true in the case of photocatalytic systems for fuels production where high efficiencies are critical for technological viability and hard thermodynamic limits are fundamentally[37] built in. Strategies have emerged for controlling the catalytic bias of these astounding biological catalysts through control of external environments and interactions.[38] This thesis will investigate later (Chapter 3) the question of whether this motif can be mimicked by an external soluble redox couple to greatly increase the efficiency of photocatalytic hydrogen production.

1.2.4 Oxygen Sensitivity in Hydrogenases

Proton reduction inherently occurs in reducing environments. At neutral conditions (pH = 7) the thermodynamic potential required is -59.2*7 = -414 mV vs. NHE. Real world catalysis typically entails application of even more negative potentials to accelerate reaction kinetics. At these potentials, other reactions besides activation of protons are possible, especially the generation of reactive oxygen species.[39-40]

1. $O_2 + e^- \rightarrow O_2^{\bullet -}$ $E^{0'} = -0.33$ V
2. $O_2 + 2H^+ + 2e^- \rightarrow H_2O_2$ $E^{0'} = +0.28$ V

Such species are highly reactive and can potentially degrade the catalytically active species. The ubiquity of elemental oxygen in earth's atmosphere has forced biological systems to develop proton reduction catalysts having structures and mechanisms that avoid inactivation or even destruction by oxygen. Activating first row transition metals towards proton reduction requires coordination by strongly donating, electron rich ligands which can be susceptible to oxidation. This can result in oxidative degradation of these ligands such as formation of phosphine oxides for Dubois type[10] proton reduction catalysts[39, 41] and oxygenation of active site cysteine ligands in [NiFe] H_2ases[42-43]. While synthetic complexes are generally irreversibly destroyed by such transformations some [NiFe] H_2ases show varying degrees of oxygen tolerance. The standard hydrogenases form two sets of Ni(III) containing paramagnetic inactive states upon exposure to oxygen or other oxidizing conditions. These states are termed Ni_r-B and Ni_u-A (where r stands for "ready", meaning readily reactivated and u for "unready", sometimes subscripts may be omitted) which are distinguished by their reactivation kinetics. Under reducing

conditions Ni_r-B can be reactivated in seconds to minutes, while Ni_u-A may require hours under reducing conditions to reactivate. The "oxygen tolerant" H_2ases appear to survive these conditions by selectively forming the rapidly reactivating Ni_r-B state and avoiding formation of Ni_u-A. Further expansion in the growth of oxygen tolerant behavior in [NiFe] hydrogenases has recently been observed in the soluble H_2ase of *Pyrococcus furiosus* where a high degree of oxygen tolerance was observed but the inactive states detected were distinct from Ni_r-B and Ni_u-A.

On top of this diversity of behaviors with respect to oxygen tolerance in the [NiFe] H_2ases, the structure of the inactive states themselves (and indeed of the active states[44]) has been highly controversial.[43, 45-46] It is generally agreed on that Ni_r-B has a structure with a bridging hydroxide ligand between the nickel and iron sites.[47] The structure of the slowly unready Ni-A state, however has been much more contentious. Two dominant ideas in the literature have been either a state involving oxygenation of active site cysteine thiolates to sulfenates[43, 48] as shown in Figure 1.1B or a peroxide species bridging between the Ni and Fe sites as in figure 1.1A although recent evidence[46] has cast doubt on the latter hypothesis. In any case, the picture is far from settled.

Figure 1.1 – Proposed structures of the Ni_u-A state in [NiFe] H_2ases implicating A) a bridging peroxide or B) a bridging cysteine sulfenate.

1.3 - Scope and Hypothesis

The goal of this thesis is twofold. Compelling evidence supports the need to advance the fundamental understanding of photocatalysis related to solar fuel production. We have thus set out to design a highly efficient photocatalytic system using semiconductor nanostructures for light harvesting and SHI as a highly stable and efficient model proton reduction catalyst through control over the energetic landscape experienced by photoexcited electrons. This system is an ideal model to study to increase the understanding of the mechanisms of photocatalytic proton reduction and methods of catalyst integration with photosensitizers.

We recognized that such a system, despite operating at high efficiencies and showing impressive robustness, is only a model for increasing the understanding of how photocatalytic systems operate and as a practical matter has very high barriers of cost, scalability and durability for application on industrial scales. As such the second goal of this thesis was to show that, despite shortcomings in terms of industrial viability, this highly robust and efficient system for optically triggering enzyme activity has a vast potential for mechanistic studies using time-resolved and steady state spectroscopy of H_2ase enzymes. We showed that this system could be exploited to observe sub-TOF dynamics at the H_2ase active site and provide deep insight into the nature of the inactive states of the enzyme and their reactivation under reducing conditions. We aim to encourage the field to exploit the full range of possibilities with model photocatalytic systems. These are not just toy models, but rather can be shaped to be powerful tools of mechanistic insight if the proper design considerations are taken.

1.4 - References

1. Lewis, N. S.; Nocera, D. G., Powering the planet: Chemical challenges in solar energy utilization. *Proc. Natl. Acad. Sci*. **2006,** *103* (43), 15729-15735.

2. Oreskes, N., The Scientific Consensus on Climate Change. *Science* **2004,** *306* (5702), 1686.

3. Figueres, C.; Joachim, H.; Schellnhuber; Whiteman, G.; Rockström, J.; Hobley, A.; Rahmstorf, S., Three years to safeguard our climate. *Nature* **2017,** *546* (7660), 593-595.

4. Cardwell, D., Tesla Ventures Into Solar Power Storage for Home and Business. *The New York Times* 5/1/2015, 2015.

5. Sripad, S.; Viswanathan, V., Performance Metrics Required of Next-Generation Batteries to Make a Practical Electric Semi Truck. *ACS Energy Letters* **2017**, 1669-1673.

6. Esswein, A. J.; Nocera, D. G., Hydrogen Production by Molecular Photocatalysis. *Chem. Rev.* **2007,** *107* (10), 4022-4047.

7. Jaramillo, T. F.; Jørgensen, K. P.; Bonde, J.; Nielsen, J. H.; Horch, S.; Chorkendorff, I., Identification of Active Edge Sites for Electrochemical H_2 Evolution from MoS2 Nanocatalysts. *Science* **2007,** *317* (5834), 100-102.

8. Yin, Q.; Tan, J. M.; Besson, C.; Geletii, Y. V.; Musaev, D. G.; Kuznetsov, A. E.; Luo, Z.; Hardcastle, K. I.; Hill, C. L., A Fast Soluble Carbon-Free Molecular Water Oxidation Catalyst Based on Abundant Metals. *Science* **2010,** *328* (5976), 342-345.

9. Gray, H. B., Powering the planet with solar fuel. *Nat. Chem.* **2009,** *1* (1), 7-7.

10. Helm, M. L.; Stewart, M. P.; Bullock, R. M.; DuBois, M. R.; DuBois, D. L., A Synthetic Nickel Electrocatalyst with a Turnover Frequency Above 100,000 s−1 for H_2 Production. *Science* **2011,** *333* (6044), 863-866.

11. Jain, A.; Lense, S.; Linehan, J. C.; Raugei, S.; Cho, H.; DuBois, D. L.; Shaw, W. J., Incorporating Peptides in the Outer-Coordination Sphere of Bioinspired Electrocatalysts for Hydrogen Production. *Inorg. Chem.* **2011,** *50* (9), 4073-4085.

12. Greene, B. L.; Joseph, C. A.; Maroney, M. J.; Dyer, R. B., Direct Evidence of Active-Site Reduction and Photodriven Catalysis in Sensitized Hydrogenase Assemblies. *J. Am. Chem. Soc.* **2012,** *134* (27), 11108-11111.

13. Brown, K. A.; Wilker, M. B.; Boehm, M.; Dukovic, G.; King, P. W., Characterization of Photochemical Processes for H2 Production by CdS Nanorod–[FeFe] Hydrogenase Complexes. *J. Am. Chem. Soc.* **2012,** *134* (12), 5627-5636.

14. Sakai, T.; Mersch, D.; Reisner, E., Photocatalytic Hydrogen Evolution with a Hydrogenase in a Mediator-Free System under High Levels of Oxygen. *Angew. Chem., Int. Ed.* **2013,** *52* (47), 12313-12316.

15. Hutton, G. A. M.; Reuillard, B.; Martindale, B. C. M.; Caputo, C. A.; Lockwood, C. W. J.; Butt, J. N.; Reisner, E., Carbon Dots as Versatile Photosensitizers for Solar-Driven Catalysis with Redox Enzymes. *J. Am. Chem. Soc.* **2016,** *138* (51), 16722-16730.

16. Rodriguez-Maciá, P.; Dutta, A.; Lubitz, W.; Shaw, W. J.; Rüdiger, O., Direct Comparison of the Performance of a Bio-inspired Synthetic Nickel Catalyst and a [NiFe]-Hydrogenase, Both Covalently Attached to Electrodes. *Angew. Chem., Int. Ed.* **2015,** *54* (42), 12303-12307.

17. Kalisman, P.; Nakibli, Y.; Amirav, L., Perfect Photon-to-Hydrogen Conversion Efficiency. *Nano Lett.* **2016,** *16* (3), 1776-1781.

18. Wu, K.; Chen, Z.; Lv, H.; Zhu, H.; Hill, C. L.; Lian, T., Hole Removal Rate Limits Photodriven H_2 Generation Efficiency in CdS-Pt and CdSe/CdS-Pt Semiconductor Nanorod–Metal Tip Heterostructures. *J. Am. Chem. Soc.* **2014,** *136* (21), 7708-7716.

19. Simon, T.; Carlson, M. T.; Stolarczyk, J. K.; Feldmann, J., Electron Transfer Rate vs Recombination Losses in Photocatalytic H2 Generation on Pt-Decorated CdS Nanorods. *ACS Energy Letters* **2016,** *1* (6), 1137-1142.

20. Lau, B.; Kedem, O.; Schwabacher, J.; Kwasnieski, D.; Weiss, E. A., An introduction to ratchets in chemistry and biology. *Materials Horizons* **2017,** *4* (3), 310-318.

21. Lubitz, W.; Ogata, H.; Rüdiger, O.; Reijerse, E., Hydrogenases. *Chem. Rev.* **2014,** *114* (8), 4081-4148.

22. Siebel, J. F.; Adamska-Venkatesh, A.; Weber, K.; Rumpel, S.; Reijerse, E.; Lubitz, W., Hybrid [FeFe]-Hydrogenases with Modified Active Sites Show Remarkable Residual Enzymatic Activity. *Biochemistry* **2015,** *54* (7), 1474-1483.

23. Pandelia, M.-E.; Nitschke, W.; Infossi, P.; Giudici-Orticoni, M.-T.; Bill, E.; Lubitz, W., Characterization of a unique [FeS] cluster in the electron transfer chain of the oxygen tolerant [NiFe] hydrogenase from Aquifex aeolicus. Proc. Natl. Acad. Sci. **2011,** *108* (15), 6097-6102.

24. Sumner, I.; Voth, G. A., Proton Transport Pathways in [NiFe]-Hydrogenase. *The Journal of Physical Chemistry B* **2012,** *116* (9), 2917-2926.

25. Happe, R. P.; Roseboom, W.; Albracht, S. P. J., Pre-steady-state kinetics of the reactions of [NiFe]-hydrogenase from Chromatium vinosum with H2 and CO. *European Journal of Biochemistry* **1999,** *259* (3), 602-608.

26. Evans, R. M.; Brooke, E. J.; Wehlin, S. A. M.; Nomerotskaia, E.; Sargent, F.; Carr, S. B.; Phillips, S. E. V.; Armstrong, F. A., Mechanism of hydrogen activation by [NiFe] hydrogenases. *Nat Chem Biol* **2016,** *12* (1), 46-50.

27. Ash, P. A.; Hidalgo, R.; Vincent, K. A., Proton Transfer in the Catalytic Cycle of [NiFe] Hydrogenases: Insight from Vibrational Spectroscopy. *ACS Catal.* **2017,** *7* (4), 2471-2485.

28. Hexter, S. V.; Grey, F.; Happe, T.; Climent, V.; Armstrong, F. A., Electrocatalytic mechanism of reversible hydrogen cycling by enzymes and distinctions between the major classes of hydrogenases. *Proc. Natl. Acad. Sci.* **2012,** *109* (29), 11516-11521.

29. Greene, B. L.; Wu, C.-H.; McTernan, P. M.; Adams, M. W. W.; Dyer, R. B., Proton-Coupled Electron Transfer Dynamics in the Catalytic Mechanism of a [NiFe]-Hydrogenase. *J. Am. Chem. Soc.* **2015,** *137* (13), 4558-4566.

30. Hidalgo, R.; Ash, P. A.; Healy, A. J.; Vincent, K. A., Infrared Spectroscopy During Electrocatalytic Turnover Reveals the Ni-L Active Site State During H2 Oxidation by a NiFe Hydrogenase. *Angew. Chem., Int. Ed.* **2015,** *54* (24), 7110-7113.

31. Krämer, T.; Kampa, M.; Lubitz, W.; van Gastel, M.; Neese, F., Theoretical Spectroscopy of the NiII Intermediate States in the Catalytic Cycle and the Activation of [NiFe] Hydrogenases. *ChemBioChem* **2013,** *14* (14), 1898-1905.

32. Armstrong, F. A.; Evans, R. M.; Hexter, S. V.; Murphy, B. J.; Roessler, M. M.; Wulff, P., Guiding Principles of Hydrogenase Catalysis Instigated and Clarified by Protein Film Electrochemistry. *Accounts of Chemical Research* **2016,** *49* (5), 884-892.

33. Abou Hamdan, A.; Dementin, S.; Liebgott, P.-P.; Gutierrez-Sanz, O.; Richaud, P.; De Lacey, A. L.; Rousset, M.; Bertrand, P.; Cournac, L.; Léger, C., Understanding and Tuning the Catalytic Bias of Hydrogenase. *J. Am. Chem. Soc.* **2012,** *134* (20), 8368-8371.

34. Hexter, S. V.; Esterle, T. F.; Armstrong, F. A., A unified model for surface electrocatalysis based on observations with enzymes. *Physical Chemistry Chemical Physics* **2014,** *16* (24), 11822-11833.

35. Adamson, H.; Robinson, M.; Wright, J. J.; Flanagan, L. A.; Walton, J.; Elton, D.; Gavaghan, D. J.; Bond, A. M.; Roessler, M. M.; Parkin, A., Re-tuning the Catalytic Bias and Overpotential of a [NiFe]-hydrogenase via a Single Amino Acid Exchange at the Electron Entry/exit Site. *J. Am. Chem. Soc.* **2017**.

36. Artz, J. H.; Mulder, D. W.; Ratzloff, M. W.; Lubner, C. E.; Zadvornyy, O. A.; LeVan, A. X.; Williams, S. G.; Adams, M. W. W.; Jones, A. K.; King, P. W.; Peters, J. W., The reduction potentials of [FeFe]-hydrogenase accessory iron-sulfur clusters provide insights into the energetics of proton reduction catalysis. *J. Am. Chem. Soc.* **2017**.

37. Shockley, W.; Queisser, H. J., Detailed Balance Limit of Efficiency of p-n Junction Solar Cells. *Journal of Applied Physics* **1961,** *32* (3), 510-519.

38. Bachmeier, A.; Wang, V. C. C.; Woolerton, T. W.; Bell, S.; Fontecilla-Camps, J. C.; Can, M.; Ragsdale, S. W.; Chaudhary, Y. S.; Armstrong, F. A., How Light-Harvesting Semiconductors Can Alter the Bias of Reversible Electrocatalysts in Favor of H2 Production and CO2 Reduction. *J. Am. Chem. Soc.* **2013,** *135* (40), 15026-15032.

39. Wakerley, D. W.; Reisner, E., Oxygen-tolerant proton reduction catalysis: much O2 about nothing? *Energy. Environ. Sci.* **2015,** *8* (8), 2283-2295.

40. Wood, P. M., The potential diagram for oxygen at pH 7. *Biochemical Journal* **1988,** *253* (1), 287-289.

41. Yang, J. Y.; Bullock, R. M.; Dougherty, W. G.; Kassel, W. S.; Twamley, B.; DuBois, D. L.; Rakowski DuBois, M., Reduction of oxygen catalyzed by nickel diphosphine complexes with positioned pendant amines. *Dalton Transactions* **2010,** *39* (12), 3001-3010.

42. Horch, M.; Lauterbach, L.; Mroginski, M. A.; Hildebrandt, P.; Lenz, O.; Zebger, I., Reversible Active Site Sulfoxygenation Can Explain the Oxygen Tolerance of a NAD+-Reducing [NiFe] Hydrogenase and Its Unusual Infrared Spectroscopic Properties. *J. Am. Chem. Soc.* **2015,** *137* (7), 2555-2564.

43. Volbeda, A.; Martin, L.; Barbier, E.; Gutiérrez-Sanz, O.; De Lacey, A. L.; Liebgott, P.-P.; Dementin, S.; Rousset, M.; Fontecilla-Camps, J. C., Crystallographic studies of [NiFe]-hydrogenase mutants: towards consensus structures for the elusive unready oxidized states. *J Biol Inorg Chem* **2015,** *20* (1), 11-22.

44. Ogata, H.; Nishikawa, K.; Lubitz, W., Hydrogens detected by subatomic resolution protein crystallography in a [lsqb]NiFe[rsqb] hydrogenase. *Nature* **2015,** *520* (7548), 571-574.

45. Ogata, H.; Kellers, P.; Lubitz, W., The Crystal Structure of the NiFe Hydrogenase from the Photosynthetic Bacterium Allochromatium vinosum: Characterization of the Oxidized Enzyme (Ni-A State). *J. Mol. Biol.* **2010,** *402* (2), 428 - 444.

46. Abou Hamdan, A.; Burlat, B.; Gutiérrez-Sanz, O.; Liebgott, P.-P.; Baffert, C.; De Lacey, A. L.; Rousset, M.; Guigliarelli, B.; Léger, C.; Dementin, S., O2-independent formation of the inactive states of NiFe hydrogenase. *Nat Chem Biol* **2013,** *9* (1), 15-17.

47. Evans, R. M.; Parkin, A.; Roessler, M. M.; Murphy, B. J.; Adamson, H.; Lukey, M. J.; Sargent, F.; Volbeda, A.; Fontecilla-Camps, J. C.; Armstrong, F. A., Principles of Sustained Enzymatic Hydrogen Oxidation in the Presence of Oxygen – The Crucial Influence of High Potential Fe–S Clusters in the Electron Relay of [NiFe]-Hydrogenases. *J. Am. Chem. Soc.* **2013,** *135* (7), 2694-2707.

48. Breglia, R.; Ruiz-Rodriguez, M. A.; Vitriolo, A.; Gonzàlez-Laredo, R. F.; De Gioia, L.; Greco, C.; Bruschi, M., Theoretical insights into [NiFe]-hydrogenases oxidation resulting in a slowly reactivating inactive state. *J Biol Inorg Chem* **2017,** *22* (1), 137-151.

Chapter 2

Materials and Methods

2.1 – Introduction

In this chapter, the wide variety of synthetic and experimental techniques used and developed in this work are outlined. The reader as also directed to the appropriate literature when previously reported methodologies were used and any modifications are given where applicable. First details of the proteins and catalytic materials used are detailed. The enzyme SHI was prepared by Chang-Hao "Perry" Wu at the University of Georgia in the lab of Dr. Michael W.W. Adams. All chemicals were used as received from standard commercial sources. Additionally, below are included details of non-trivial data analysis methods used.

2.2.1 Soluble Hydrogenase 1 from *Pyrococcus furiosus*

Expression and purification of the *Pf* SHI enzyme followed a literature protocol[1] without modification. The resulting stock solution, typically 1-10 mg/mL, was stored in an anaerobic chamber containing 2-4% H_2 gas (Coy labs) in a Tris buffer at pH = 8 containing 2 mM dithiothreitol and 2 mM dithionite to maintain reducing conditions. Aliquots were purified by concentration and re-dilution with 50 kD centrifugal concentration filters (Amicon) prior to any sample preparation.

2.3.1 Synthesis of PDQ^{2+}

PDQ^{2+} was synthesized according to a previously reported procedure[2] with some modification as outlined in scheme 2.1. Briefly, 6 grams of 2,2' bipyridine was heated to reflux in 20 mL of 1,3-dibromo propane for 2-3 hours. The solid product was filtered off and dissolved in a small volume of water and precipitated with acetone. The resulting

pale-yellow solid was recrystallized twice from methanol. Purity was confirmed by NMR as well as close match with the previously reported spectra of the cation radical as shown later in figure 2.2.

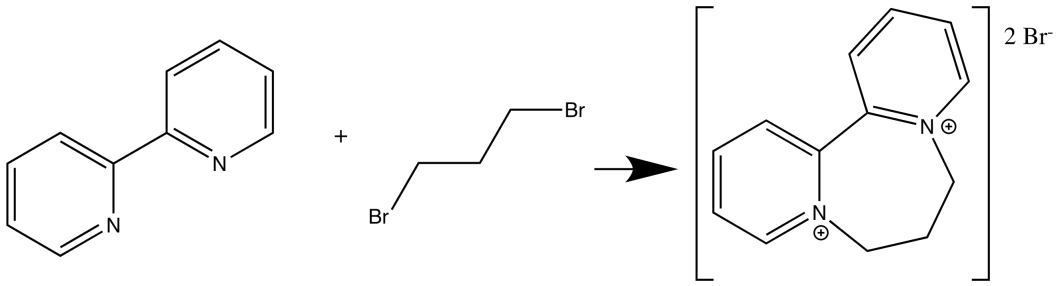

Scheme 2.1 - Synthesis of PDQ^{2+}

2.3.2.1 Synthesis of CdSe/CdS Dot in rod heterostructures and ligand exchange

50 nm CdSe/CdS nanorods were synthesized according to literature procedures[3] with minor modification. Images of the particles taken by electron microscopy are shown in Figure 2.1. The crude reaction solutions were not purified until needed. Instead 5 mL of toluene was added to the crude reaction solutions and this was stored at -20 C° in the dark without purification until needed for ligand exchange. The nanoparticles stored in this way are highly stable and preserve their as-synthesized properties for at least months without degradation.

Ligand exchange of the nanoparticles was carried out by extensive modification of a reported procedure.[4] Briefly, CdSe/CdS Dot-in-rod heterostructures (DIRs) were precipitated from the crude reaction mixture with ethanol and then pelleted in a centrifuge at 5000 x g for 5 minutes. The QD's were then dissolved in chloroform, subsequently precipitated with ethanol, and finally suspended in chloroform at 20-100 μM. The exchange solution was prepared as 100 mM of thiol and 50 mM TCEP in 3:1 MeOH:H_2O, pH adjusted to 9.5. Then 0.5 mL of the DIR chloroform solution and 1 mL

of the exchange solution were mixed in an Eppendorf tube and vortexed for 2 minutes. The aqueous and organic phases were allowed to separate and 10 mL borate buffer (10 mM, pH = 8) and chloroform (2 mL) were added to increase the volume of the respective phases. The mixture was shaken and then allowed to phase separate. The organic phase was removed and the aqueous phase was 2x extracted with chloroform to remove residual hydrophobic ligand. The resulting thiol-capped nanocrystals were purified using 50 kDa molecular weight cutoff Centricon spin filters to remove excess thiol and exchanged into a 10 mM pH = 8 borate buffer, containing 1mM thiol and 1 mM tris-carboxyethylphosphine (TCEP). Ligand exchanged samples were stored in the dark under an inert atmosphere as stock solutions.

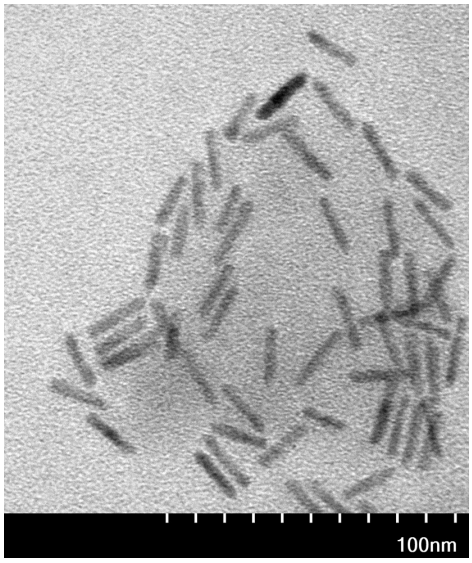

Figure 2.1 – Transmission electron microscopy images of CdSe/CdS DIR structures deposited on a holey carbon copper backed grid.

2.4 - Physical and Analytical Methods

2.4.1 - UV and Visible absorption spectroscopy

UV and visible spectra on large volume samples was typically carried out on a Lambda 35 UV-Vis spectrophotometer (Perkin Elmer) with a 1 nm slit width with a scan speed of 496 nm/min. Spectroscopy of other samples was carried out using a modular home-built fiber coupled spectrometer described here. Light from a 100 W Xeon lamp (Oriel Inc.) was coupled into a solarization resistant optical fiber (Ocean Optics Inc.) and directed into a collimating optic typically mounted in a cuvette holder containing the sample. The collimated beam passes through the sample and into another fiber coupled collimated optic. This fiber is attached to a spectrometer (QE-6500 Ocean Optics). Absorbance measurements were performed in single beam mode and the reference was a solvent blank or empty air as appropriate. Probe beam levels were selected to maximize sensitivity while avoiding the possibility of probe beam driven photochemistry which was typically verified by means of control experiments that verified that spectra did not change over time in the presence of the probe beam absent external photoexcitation.

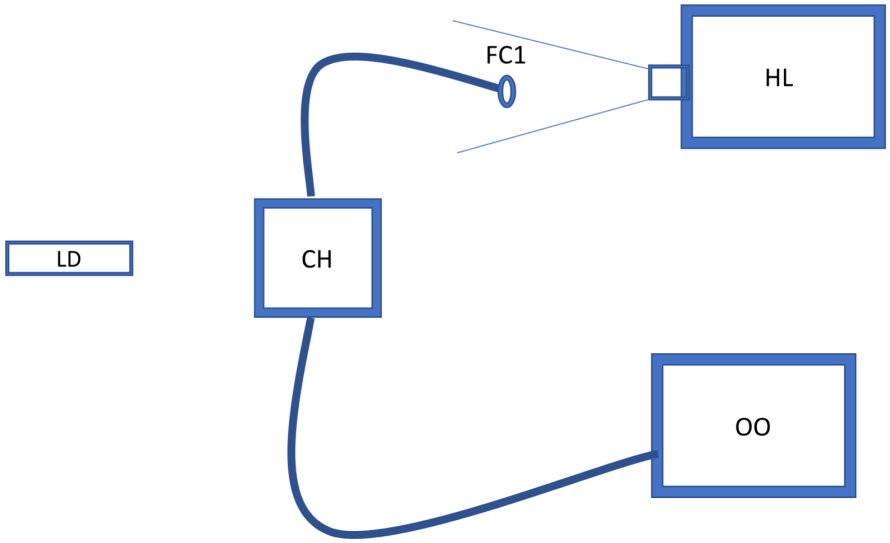

Scheme 2.2 – Apparatus for fiber coupled UV-Vis spectroscopy during photocatalysis. HL is a xeon lamp, FC1 is a fiber coupler and the curved lines are solarization resistant fiber optic cables. CH is a cuvette holder and OO is the fiber coupled spectrometer. LD is the laser diode excitation source.

2.4.2 – FTIR spectroscopy and light titrations

FTIR measurements were conducted on a Varian 660 FTIR spectrometer with the beam directed to an external detector contained in an external purged box. The beam is focused on the sample with a gold parabolic mirror, recollimated and then focused onto a 1 mm LN_2 cooled Mercury Cadmium Telluride detector by two more parabolic gold mirrors. Sample temperature was controlled by a water bath and lateral sample position was adjusted by a computer controlled single axis stage. Measurements were performed with 2 cm^{-1} resolution and 37.5 kHz modulation frequency and a 20 kHz frequency filter. The data were Fourier transformed and ratioed against an appropriate reference in the same sample cell to obtain the absorbance signal.

Light titration experiments were performed using the same spectrometer and external plexiglass box setup. A diode laser (5 mW 455 nm Thor Labs) outside the box was defocused by a lens and transmitted through the plexiglass enclosure to uniformly illuminate the sample. The light intensity at the sample was 50-100 $\mu W/cm^2$. Light exposure was gated by a LabVIEW controlled shutter and LabVIEW also controlled the spectra acquisition. In some cases, optical spectra were collected during the light titrations by overlapping the collimated visible beam from an optical fiber (Ocean Optics) with the infrared beam in the sample plane using the spectrometer described in 2.4.1.

2.4.3 – Hydrogen production and detection

Hydrogen production was measured using two complementary techniques. Gas chromatography (GC) measurements were done on an Agilent 7890A gas chromatograph with a pulsed discharge detector (PDD) by Valco Inc. and a 25m molecule sieve column. The oven was kept at 100 ^{0}C while the inlet was kept at 150 ^{0}C. A calibration curve for response to hydrogen was constructed by injecting a controlled amount of humid hydrogen gas into the sample cell headspace by gastight syringe (Hamilton) and then withdrawing a small aliquot of the headspace volume via syringe after sample equilibration. Retention times at 8 psi and a 100:1 split of the injection were 1.4 minutes, 1.8 minutes and 2.04 minutes for hydrogen, oxygen and nitrogen respectively. The volume of hydrogen was converted to moles of hydrogen by application of the gas law $PV = nRT$.

In additional experiments, hydrogen production was monitored using pressure transducers in a method inspired by the work[5] of Krauss and coworkers. Pressure

transducers from Phidgets (1137_0 and 1140_0) and I/O board (1018_2) were used to monitor pressure with a home written LabVIEW program. The sensors were cemented with epoxy into screw-on cuvette caps for quartz fluorescence cuvettes (Firefly Scientific) which were sealed with O-rings. Inlets and outlets to the cells were provided by IDEX microfluidic valves to allow purging of the cuvette headspace. Headspace volume was determined by measurement of the mass of water required to completely occupy the internal cuvette volume when the sample volume was present. The ideal gas law was then used to determine the gas evolved with a correction for Henry's law under assumption of equilibrium. We ensure this condition is met with vigorous stirring near the surface of the cuvette volume which we found to be necessary for lag free response of the pressure transducer. The error in the pressure values are reported as ± 5% in the pressure by the manufacturer, which is directly proportional to the error in the moles of hydrogen produced.

2.2.4 Photoluminescence titration of mediator nanorod interaction

Fluorescence measurements were taken on a Flouromax spectrophotometer (Horiba Scientific, Edison, New Jersey). Optical densities of the CdSe/CdS DIR at the excitation wavelengths were kept below 0.1 to minimize inner filter effects. Samples of the DIR were prepared in 50mM phosphate buffer in an anaerobic chamber and loaded into a quartz fluorescence cuvette sealed with a septum. Concentrated solutions of the redox mediators were titrated in via gas tight syringe (Hamilton) to generate the appropriate mediator concentrations with minimal dilution (>1% throughout). Excitation

of the sample was at 450 nm with 10 ms integration time, detector set to low gain and each spectrum was the result of 3 averages.

2.4.5 Mediator photoreduction

Samples for measuring the photoreduction of mediators were prepared under inert atmosphere (4% H_2 96% N_2, O_2 < 5 ppm) in the dark or under dim red light only, as follows: Aliquots of DIR were withdrawn from the stock solutions. These were purified and concentrated using 50 kD centrifugal filters (Centricon). DIR concentrate was recovered from the filters using the desired buffer/sacrificial donor solution and transferred to a quartz cuvette with a magnetic stir bar. An aliquot of mediator (PDQ^{2+} or MV^{2+}) from a concentrated stock solution (0.5 M) in deionized water was added to achieve the final desired mediator concentration. Buffer/sacrificial donor solution was added to achieve the final total volume of 1.4 mL. The cuvette was sealed with a rubber septum (Suba Seal). Prior to photo-excitation, the cuvette head space was purged with purified nitrogen gas. The sample was excited with a 4.04 mW 405 nm diode laser (Thor Labs) with the power measured by a thermal power meter (Thor Labs PM160T). A Lab-View controlled mechanical shutter gated excitation light. The optical spectrum was monitored in tandem by a fiber-coupled UV-Vis spectrometer as detailed in section 2.4.1

2.4.6 Photo driven hydrogen production

Light driven hydrogen production was performed similarly to the mediator photoreduction experiments in section 2.4.5. SHI samples were prepared from a stock solution stored in the anaerobic chamber by purification and concentration in 50 kD

Centricon filters. This was then added to the DIR-SED-mediator samples as prepared above and allowed to equilibrate for 20 minutes. Samples were purged with nitrogen until any reduced mediator was reoxidized by SHI. The photoexcitation was carried out as above. The headspace was sampled by GC to measure hydrogen production or the headspace pressure was monitored as described in 2.4.3. Optical spectra were also recorded during photocatalysis via the fiber coupled spectrometer described in 2.4.1.

2.4.7 Time-resolved Photoluminescence

Fluorescence decays were collected on a Nikon confocal scanning laser microscope interfaced with Picoquant TCSPC electronics (LSM upgrade kit). Samples were prepared in an anaerobic chamber in melting point capillary tubes and sealed with vacuum grease. Samples in the capillaries were imaged via the confocal microscope and excited with a 405 nm diode laser at 1 MHz repetition rate. The emission was passed through a 520nm long pass filter (Semrock, RazorEdge) to remove scattered excitation light. The instrument response function was measured by using a narrow band-pass filter to isolate scattered excitation light and measured to be ~ 150 ps FWHM. Data were collected until 10,000 counts was reached at the beginning of the decay trace to ensure good signal to noise ratio.

2.4.8 Ultrafast Transient Absorbance

Ultrafast TA measurements were made using an Ultrafast Systems TA instrument and preparing the mediator complexes in chloroform as previously described.[6] Briefly, solutions of DIR in chloroform were sonicated with ~ 1 mg of the solid redox mediator

for 15 minutes. These solutions were then passes through 0.2 micron filters to remove undissolved solids and loaded into 1mm quartz cuvettes. The measuremnts were performed on an identical setup to that reported.[6]

2.4.9 – Nanosecond to Millisecond Visible and Infrared Transient Absorbance

Samples for time resolved IR and visible spectroscopy as well as light titrations on SHI were prepared as follows. Ligand exchanged solutions of MPA-NR and SHI stock solutions (750 μL of the nanocrystals prepared as previously described and ~1 mg SHI) stored in a Coy labs anaerobic chamber (2-4% H_2) were concentrated and purified using independent 10 kD Centricon spin concentrators with thiol containing buffers (10 mM MPA 50 mM phosphate typically) and concentrated to ~ 20 μL. The sample side of the IR cell (home built copper cell with a 50-75 μm PTFE spacer split between sample and reference sides) was prepared by mixing 10 μL each of the concentrated SHI and MPA-NR solutions. To this solution was added a 1-2 μL aliquot of PDQ stock solution in DI H_2O of the appropriate concentration to yield a final PDQ concentration of 10 mM. The sample was then carefully mixed by aspiration into a gastight syringe and then transferred to the sample side of the IR cell. The reference side was prepared similarly, replacing SHI with 1mg of horse heart met-myoglobin. Time resolved infrared and visible spectroscopy was performed as previously described[7] with the exception of using an 808

nm probe laser diode rather than 635 nm as described previously in order to be more sensitive to the $PDQ^{+\bullet}$ absorbance as shown in figure 2.2.

2.5 – Data Analysis

2.5.1 Fitting and SVD Analysis of broadband ns transient absorption data

Analysis of the nanosecond broadband transient absorption spectra were carried

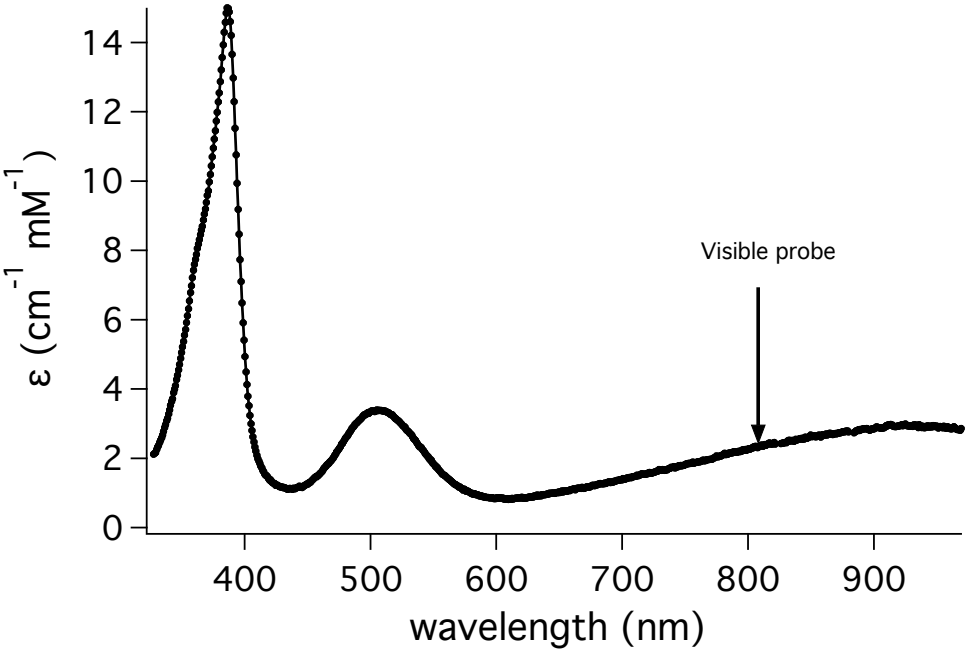

Figure 2.2 – Extinction spectrum of $PDQ^{+\bullet}$ radical and probe wavelength of the time resolved visible experiment as described in 2.4.9.

out in Igor Pro 6.37 using the TADataAnalysis_v4.2 code. Errors are reported as +/- 1 standard deviation of the time constants in the multi exponential fits as output in the fitting procedure after fixing the fitted time zero, instrument response time constant and pre-excitation baseline to their fitted values.

Spectral regions of the nanosecond data known to contain spectral signatures of the charge separated state and excitons were selected from the nanosecond transient absorption data sets as regions of interest (ROI). SVD was performed on these ROIs and the kinetics of the singular vectors corresponding to the state of interest were extracted. The extracted singular vectors are shown in Figure 2.3 and correspond to the known spectral features of the excitonic and charge separated states in these materials. The resulting kinetics are shown in figure 3.5C and more details can be found in section 3.2.2.

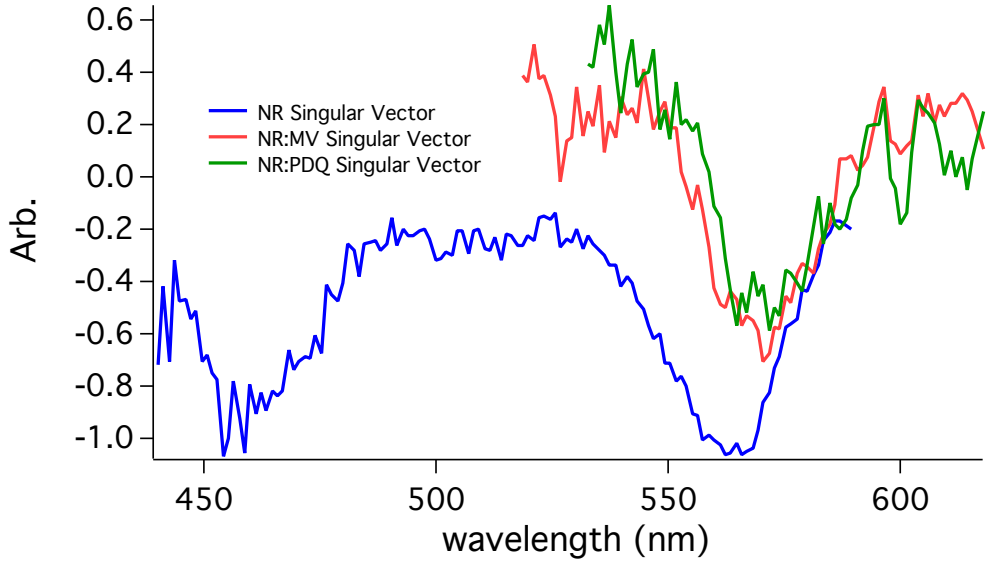

Figure 2.3 - Singular Vectors Extracted from SVD Analysis of Ultrafast TA Spectra. These signals reproduce the important spectral features of the exciton and charge separated states present at the end of the fs-TA experiment (Figure 3.5 A) including the redshift of the bleaches of the charge-separated states supporting the assignment.

2.5.2 Global fitting of photochemical reactivation data

Analysis of the light titration spectra was carried out in Igor Pro 7 using the included global fitting routine. A model for the data consisting of 8 independent Gaussian peaks (1) was used to fit the data and capture the behavior of all the observed states in the CO region (~1910 cm^{-1} - ~1990 cm^{-1}).

(1) $$y = y_0 + \sum_{n=1}^{8} a_n e^{-\left(\frac{x-x_n}{w}\right)^2}$$

The energy of each Gaussian component (x_n) was fit to a single global variable and the model was further constrained to share a single global peak width (w) for every Gaussian components. Thus, only the amplitudes (population) of each state can vary from spectrum to spectrum

2.6 – References

1. Chandrayan, S. K.; Wu, C.-H.; McTernan, P. M.; Adams, M. W. W., High yield purification of a tagged cytoplasmic [NiFe]-hydrogenase and a catalytically-active nickel-free intermediate form. *Protein Expression Purif.* **2015,** *107*, 90-94.

2. Homer, R. F.; Tomlinson, T. E., The stereochemistry of the bridged quaternary salts of 2,2'-bipyridyl. *J. Chem. Soc.* **1960,** (0), 2498-2503.

3. Carbone, L.; Nobile, C.; De Giorgi, M.; Sala, F. D.; Morello, G.; Pompa, P.; Hytch, M.; Snoeck, E.; Fiore, A.; Franchini, I. R.; Nadasan, M.; Silvestre, A. F.; Chiodo, L.; Kudera, S.; Cingolani, R.; Krahne, R.; Manna, L., Synthesis and Micrometer-Scale Assembly of Colloidal CdSe/CdS Nanorods Prepared by a Seeded Growth Approach. *Nano Lett.* **2007,** *7* (10), 2942-2950.

4. Zylstra, J.; Amey, J.; Miska, N. J.; Pang, L.; Hine, C. R.; Langer, J.; Doyle, R. P.; Maye, M. M., A Modular Phase Transfer and Ligand Exchange Protocol for Quantum Dots. *Langmuir* **2011,** *27* (8), 4371-4379.

5. Han, Z.; Qiu, F.; Eisenberg, R.; Holland, P. L.; Krauss, T. D., Robust Photogeneration of H2 in Water Using Semiconductor Nanocrystals and a Nickel Catalyst. *Science* **2012,** *338* (6112), 1321-1324.

6. Wu, K.; Rodríguez-Córdoba, W. E.; Liu, Z.; Zhu, H.; Lian, T., Beyond Band Alignment: Hole Localization Driven Formation of Three Spatially Separated Long-Lived Exciton States in CdSe/CdS Nanorods. *ACS Nano* **2013,** *7* (8), 7173-7185.

7. Greene, B. L.; Wu, C.-H.; McTernan, P. M.; Adams, M. W. W.; Dyer, R. B., Proton-Coupled Electron Transfer Dynamics in the Catalytic Mechanism of a [NiFe]-Hydrogenase. *J. Am. Chem. Soc.* **2015,** *137* (13), 4558-4566.

Chapter 3

Efficient Photocatalytic Hydrogen Production in CdSe/CdS Nanorod-[NiFe] H_2ase Assemblies: Balancing Electron Transfer Rate and Driving Force

Abstract: We describe a hybrid photocatalytic system for hydrogen production consisting of nanocrystalline CdSe/CdS dot-in-rod (DIR) structures coupled to [NiFe] soluble hydrogenase I (SHI) from *Pyrococcus furiosus*. Electrons are shuttled to the catalyst by a redox mediator, either methyl viologen (MV^{2+}, E_0 = -446 mV vs. NHE) or propyl-bridged 2-2'-biyridinium (PDQ^{2+}, E_0 = -550 mV vs. NHE). We demonstrate nearly equal photoreduction efficiencies for the two mediators, despite extracting ~100 mV of additional driving force for proton reduction by PDQ^{2+}. Femtosecond to microsecond transient absorption reveals that while electron transfer (ET) from the DIR to PDQ^{2+} is slower than for MV^{2+}, in both cases the ET process is complete by 1 ns and thus it efficiently outcompetes radiative decay. Long-lived charge separation is observed for both mediators, resulting in similar net efficiencies of photoreduction. Whereas both mediators are readily photoreduced, only PDQ^{2+} yields measurable H_2 production, demonstrating the importance of optimizing the electron shuttling pathway to take advantage of the available reducing power of the DIR excited state. H_2 production in the PDQ^{2+} system is highly efficient, with an internal quantum efficiency (IQE) as high as 77% and a TON_{SHI} of 1.1 x 10^6 under mild (RT, pH = 7.35) conditions

3.1 - Introduction

With the crises of greenhouse gas emission driven climate change[1] and environmental degradation looming ever larger, the prospect of using the solar flux to reduce aqueous protons to H_2 for large-scale fuel production holds great promise for a sustainable, carbon free fuel cycle.[2] Photochemical production of H_2 requires efficient coupling of a photosensitizer with a catalyst. Quantum dots (QDs) and related semiconductor

nanostructures are ideal photosensitizers because of their large optical cross sections, tunable bandgaps and absolute redox potentials that can be matched to the catalytic process of interest, including solar H_2 generation.[3-4] While near unity internal quantum efficiency IQE of H_2 generation has been demonstrated using Pt tipped CdSe/CdS heterostructures, albeit under harsh alkaline conditions, using an unconventional hole shuttling mechanism,[5] achieving higher efficiencies without noble metal catalysts remains challenging.

Hydrogenases (H_2ases) are enzymes highly optimized for H_2 oxidation and proton reduction that operate close to the thermodynamic limit with high turnover frequencies using active sites containing the earth abundant metals nickel and iron.[6] H_2ases, therefore, are important model systems to inform the rational design of synthetic catalysts for highly efficient photochemical H_2 production. Coupling of H_2ases to QDs and other nanostructured light absorbers to form hybrid photocatalytic systems has been an active area of research and this strategy has recently been extended to drive other important reactions such as nitrogen reduction[7] and enzyme cofactor regeneneration.[8] Such biotic-abiotic systems have achieved IQE for H_2 production of up to 20% in the case of CdS nanorod-[FeFe] H_2ase hybrids.[9] Progress has also been made in sensitizing H_2ases with more environmentally benign and scalable materials such as dyes and carbon quantum dots.[10-11]

Despite the high efficiency of the individual photosensitizer and catalytic components of these hybrid systems, the net IQE of H_2 production remains modest.[3-4, 10, 12] We postulate that slow interfacial electron transfer from the nanoparticle surface to the electrostatically bound enzyme limits the overall efficiency. In this study, we have

circumvented this problem by introducing a redox mediator. We show that by optimizing the mediator it is possible to achieve much higher efficiencies of H_2 production. We selected a propyl-bridged 2-2'-bipyridinium (PDQ^{2+}, Scheme 1) to mediate proton reduction using a CdSe/CdS dot-in-rod (DIR) photosensitizer coupled to the soluble [NiFe] hydrogenase I (SHI) from the hyperthermophilic archeon *Pyrococcus furiosus* (*Pf*).[13] *Pf* SHI was chosen for its very high thermal stability and its oxygen tolerance.

The best choice of mediator depends on a careful balance of several factors, including reduction potential, electron transfer (ET) rates and stability and optical absorption of the radical. We have shown that nanoparticle sensitizers photoreduce electrostatically bound methyl viologen (MV^{2+}) with high efficiency.[14] MV^{2+} has been used extensively as an electron relay for photocatalytic H_2 generation,[15] although these systems suffer from some drawback such as irreversible hydrogenation of $MV^{+\bullet}$ at catalytic Pt surfaces[16] and strong product inhibition. The midpoint reduction potential of MV^{2+} (-446 mV vs. NHE) does not provide a large free energy change at neutral aqueous conditions to drive electron transfer (ET) to a proton reduction catalyst (~32 mV). Although MV^{2+} can be effective in mediating proton reduction at lower pH due to the higher driving force (~150 mV at pH 5), colloidal semiconductor nanostructures tend to lose their solution stability under these conditions.[14, 17-18] Aggregation at low pH degrades their photocatalytic performance and introduces undesirable light scattering effects, thus removing the advantages of a homogenous system.

One strategy to overcome these limitations is to modify the redox mediator structure to capture more free energy from the photosensitizer excited state to drive subsequent ET to the catalyst.[15] This is possible since the photosensitizer excited state typically has a large

overpotential with respect to the thermodynamic potential of the catalytic process of interest. If it is feasible to capture some of this excess free energy in the form of a more cathodic mediator potential to drive catalysis[20]

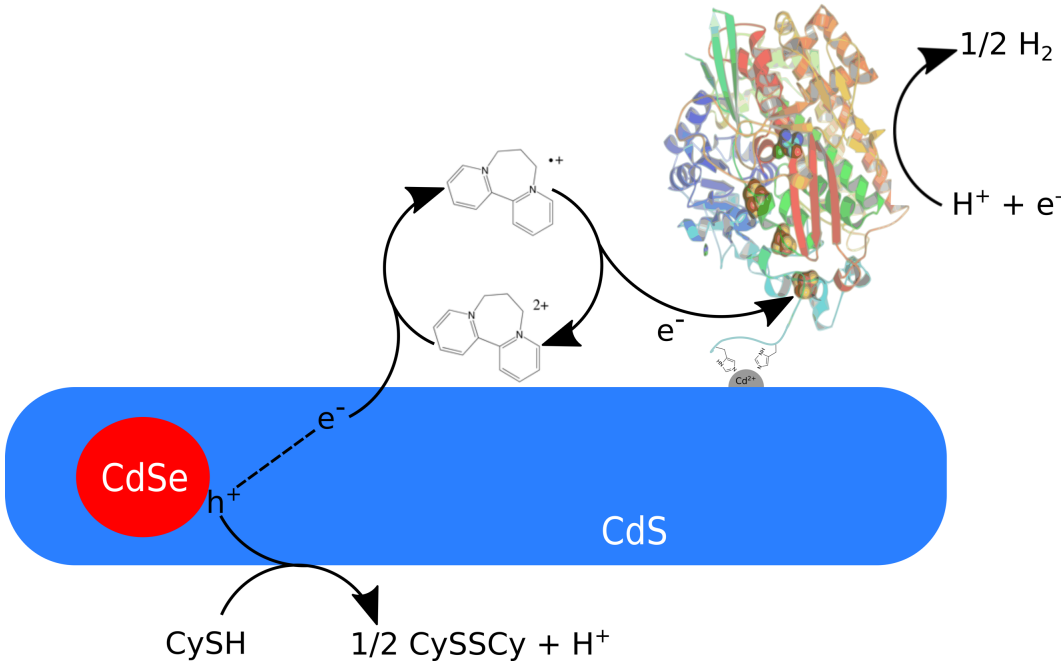

Scheme 3.1 - Representation of the photocatalytic system described in this work. CySH is the thiol sacrificial electron donor (cysteine). e----h+ represents the photo-generated excitonic state in the CdS domain. The catalytic subunit of SHI is depicted using the crystal structure of *Allochromatium vinosum* [NiFe] hydrogenase (PDB 3MYR).[19]

without unduly sacrificing ET efficiency between the sensitizer and the mediator,[21] the net result should be enhanced H_2 generation. This concept has been explored with $Ru(bpy)_3^{2+}$ sensitization,[20-23,24] although the steady state concentration of radicals produced *in situ* and the effect of their optical properties on productive light absorption and ultimately efficiency have not been explicitly considered. The results have generally shown that efficiency can be enhanced using lower potential mediators,[20, 23] although the

yield of electron transfer drops significantly as the potential is reduced.[21] Therefore, even under optimal conditions these systems have been limited to QYs of H_2 production below 20%.[24] Clearly, optimizing the efficiency of photocatalysis is not a simple matter of maximizing the reduction potential extracted from the photosensitizer because of the tradeoff with the efficiency of ET to the catalyst. Furthermore, variation of mediator structure might alter the details of mediator interaction with the nanoparticle surface and hence the ET efficiency.[25]

We have thoroughly characterized the excited state processes responsible for H_2 production for the photocatalytic system represented in Scheme 1, and we present a comprehensive analysis of the operation of the system during photocatalysis. Our results show that CdSe/CdS DIR structures can photoreduce PDQ^{2+} and MV^{2+} with equal efficiency and the PDQ^{2+} mediated photocatalytic system generates H_2 with high efficiency under neutral conditions, whereas no H_2 production is detected with MV^{2+} under the same conditions. We exploit redox mediator overpotential to improve the performance of the photochemically driven hydrogenase enzyme without incurring an efficiency penalty in the initial electron transfer process that typically affects molecular photosensiFtizers.[20-21] These results demonstrate the importance of balancing fast charge separation rates with maximization of the free energy extracted by the charge separation process itself. They also motivate more detailed exploration of the structural aspects controlling ultrafast electron transfer such as the effect of the mediator structure on its interaction with the semiconductor surface.

3.2 – Results and Discussion

3.2.1 – Photocatalytic Hydrogen Production

We first established the binding of the MV^{2+} and PDQ^{2+} redox mediators (Fig. 1A) to the DIR surface and excited state electron transfer (ET) by measuring the DIR photoluminescence (PL) spectrum as a function of mediator concentration. Quenching of the PL intensity provides a sensitive indication of acceptor binding and excited state ET since the latter prevents radiative recombination of the exciton[3]. Figure 3.1B shows representative PL spectra for titration of a DIR solution with the PDQ^{2+} mediator, demonstrating quenching of the DIR emission with increasing PDQ^{2+} concentration. PL titrations for both mediators are shown in Figure 3.1C as well as the behavior in the presence of a sacrificial electron donor (SED), cysteine. These are fit to a single Langmuir isotherm to extract binding constants shown in Table 3.1. The titrations reveal reciprocal binding constants for both MV^{2+} and PDQ^{2+} (34.9 μM and 76.4 μM respectively) that shift to the hundreds of micromolar range (179 μM and 340 μM) in the presence of 16 mM cysteine. The origin of the stronger binding constants for MV^{2+} compared to PDQ^{2+} is not known, although this may be correlated with differences in the charge transfer dynamics as discussed in the next section. Importantly, these results reveal that maximum electron transfer efficiency requires millimolar concentrations of redox mediator in solution. Therefore, subsequent photo-reduction and hydrogen evolution experiments were performed within this concentration range.

Table 3.1: Parameters for Langmuir isotherms in Figure 3.1.C

Condition	K_{Lang} (M^{-1})	$1/K_{Lang}$ (μM)
MV titration	28661	34.9
PDQ titration	13044	76.7
MV titration, 16mM Cys	5593	179
PDQ titration, 16mM Cys	2941	340

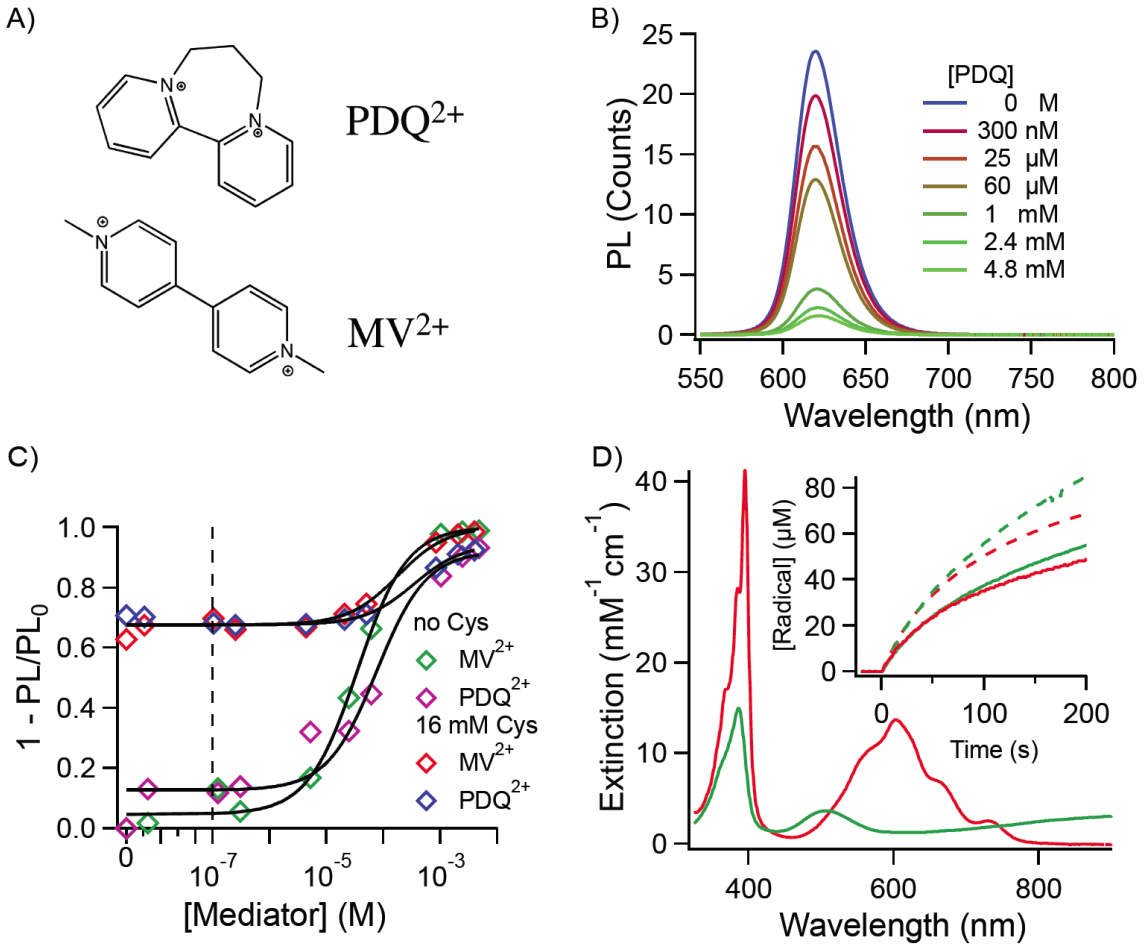

Figure 3.1 - Mediator binding to DIR and photo-induced ET. A) Structures of the two redox mediators used in this study. B) Photoluminescence (PL) spectra of glutathione (GSH) stabilized CdSe/CdS DIR in 50 mM phosphate buffer pH = 7.4 in the presence of increasing concentrations of PDQ^{2+}. C) Quenching of integrated PL intensity with increasing concentrations of redox mediators with and without 16 mM cysteine; solid lines are single Langmuir isotherm fits. D) Extinction spectra of $MV^{+\bullet}$ (red) and $PDQ^{+\bullet}$ (green) cation radicals. Inset: pH dependent steady state photo-reduction of MV^{2+} (red) and PDQ2+ (green) at pH = 7.3 (solid lines) and pH = 8.5 (dashed lines) with 12 nM DIR and 20 mM GSH.

We measured the steady-state photoreduction of MV^{2+} and PDQ^{2+} with DIR

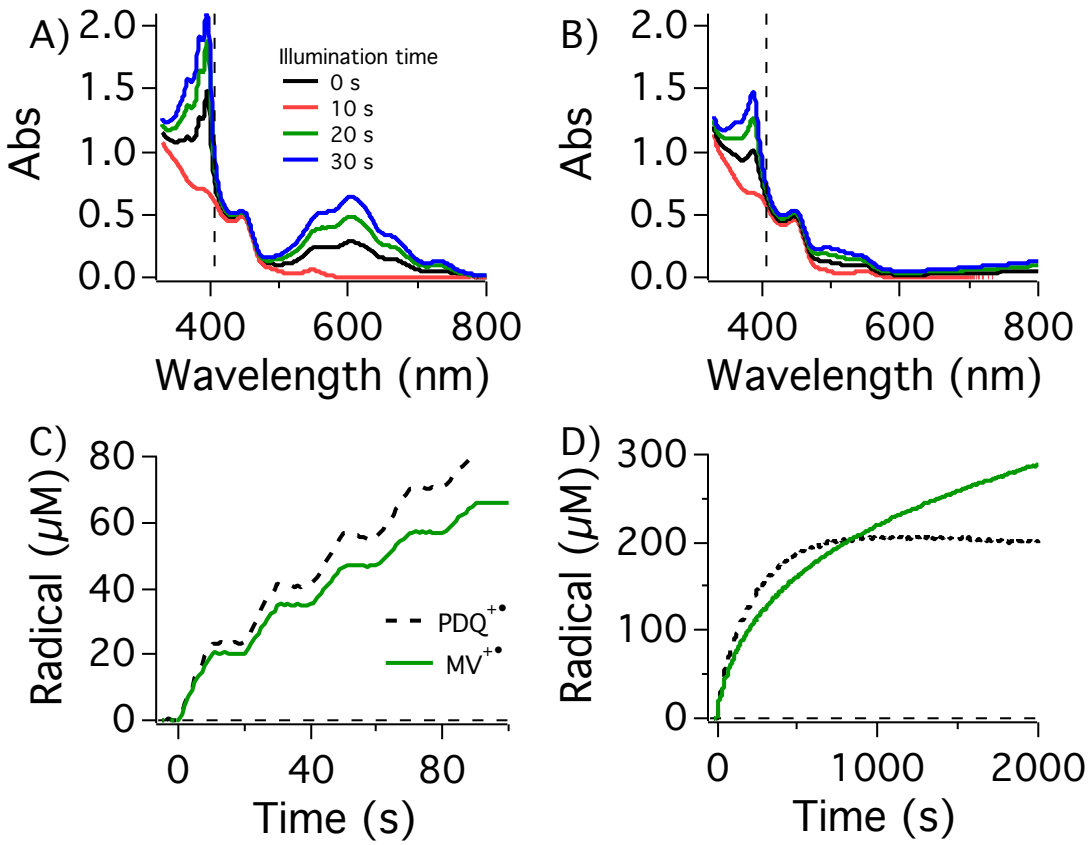

Figure 3.2 – Quantum yield of mediator photoreduction Absorbance spectrum as a function of illumination time for DIR photoreduction samples with 8 mM MV^{2+} A) and 8 mM PDQ^{2+} B). Vertical dashed lines denote the energy of the excitation light. Changes in the mediator radical concentration as a function of time in the photoreduction experiment at early C) and later D) time.

photo-sensitizers using the unique visible absorbance of the reduced mediator cation radical (Fig. 3.1D). Samples with 12 nM DIR and varying concentrations of mediator and SED were illuminated with a 405 nm diode laser under vigorous stirring. Radical concentrations were monitored spectrophotometrically. Initial experiments with glutathione (GSH) functioning as both surface capping DIR ligand and SED revealed that MV^{2+} and PDQ^{2+} were reduced with comparable initial rates as shown in the Figure 3.1D

inset. Increasing the pH from 7.3 to 8.5 led to a 40% increase in photoreduction rate, consistent with a hole quenching limited process since the surface bound thiolate ligand is the active hole scavenger.[26] The ligand affinity for the CdS surface depends on thiol

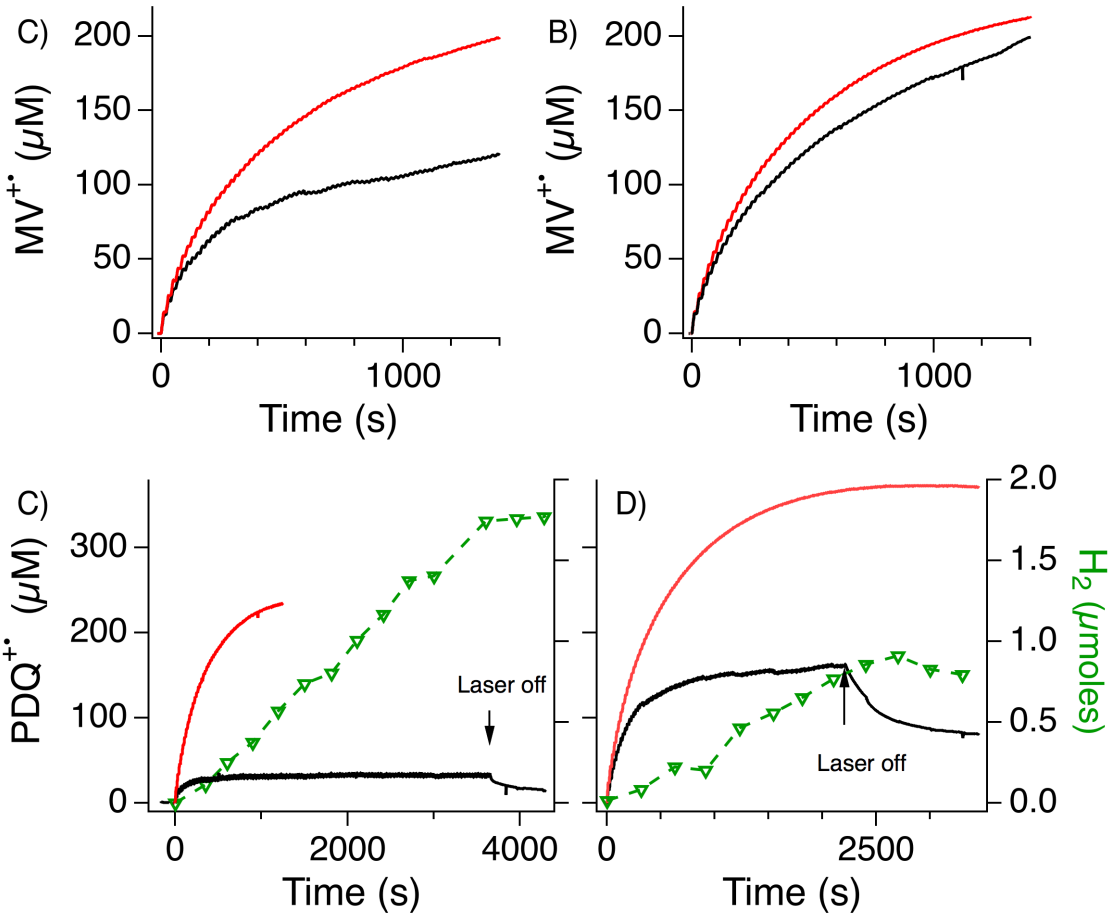

Figure 3.3 – Comparison of MV^{2+} and PDQ^{2+} Photocatalysis. Concentration of photo-generated $MV^{+\bullet}$ (A,B) and $PDQ^{+\bullet}$ (C,D) radical in solution as a function of irradiation time at pH = 7.35 (A,C) and pH = 8.39 (B,D) with (black traces) and without (red traces) 72 nM SHI. Conditions: 5.7 mM MV^{2+} (A,B) PDQ^{2+} (C,D), 100 mM Cysteine, 12 nM MPA-DIR, 50 mM phosphate buffer, excitation source chopped 10 s on / 10 s off with a shutter. Axes on the left correspond to photo-generated radical concentration. Those on the right of the bottom panel correspond to hydrogen produced.

deprotonation[17] and going from pH = 7.3 to 8.5 corresponds to a 13 to 14-fold increase in the concentration of the thiolate anion of glutathione in accordance with the known pKa(SH) = 9.2 - 9.4 of glutathione[27-28] which likely accelerates replenishing of oxidized ligands at the DIR surface.

After about a minute of photolysis, the MV^{2+} photoreduction rate begins to decline relative to that for PDQ^{2+} containing samples. We attribute this to internal screening of the 405-nm excitation light by the $MV^{+\bullet}$ radical which is more strongly absorbing than the $PDQ^{+\bullet}$ radical, as evident from the extinction spectra of these species reported in Figure 1D. These observations motivated us to screen a variety of different sacrificial donors; we reasoned that a higher yield of mediator photoreduction would lead to the higher H_2 production efficiency. We selected cysteine as the SED based on its excellent hole scavenging properties, together with mercaptopropionic acid (MPA) stabilized DIR to explore photocatalytic H_2 generation. Photoreduction under these conditions is shown in Figure 3.2 and yielded 78% Quantum efficiency of MV^{2+} photoreduction and 89% quantum efficiency of PDQ^{2+} photoreduction.

We performed photocatalytic H_2 evolution experiments at pH 7.35 and under more alkaline conditions, pH = 8.39. Using MV^{2+} as the mediator we failed to detect significant H_2 production at either pH by gas chromatography (GC). Radical concentrations as a function of irradiation time in the presence and absence of 72 nM SHI are shown in the 3.3A-B. We also performed the corresponding experiments with PDQ^{2+} as the electron carrier. In this case, significant H_2 was evolved and GC data following H_2 production is included in the Figure 3.3C-D. We report two different values for efficiency of H_2 production: the quantum yield (QY) refers to the efficiency corrected for reflection

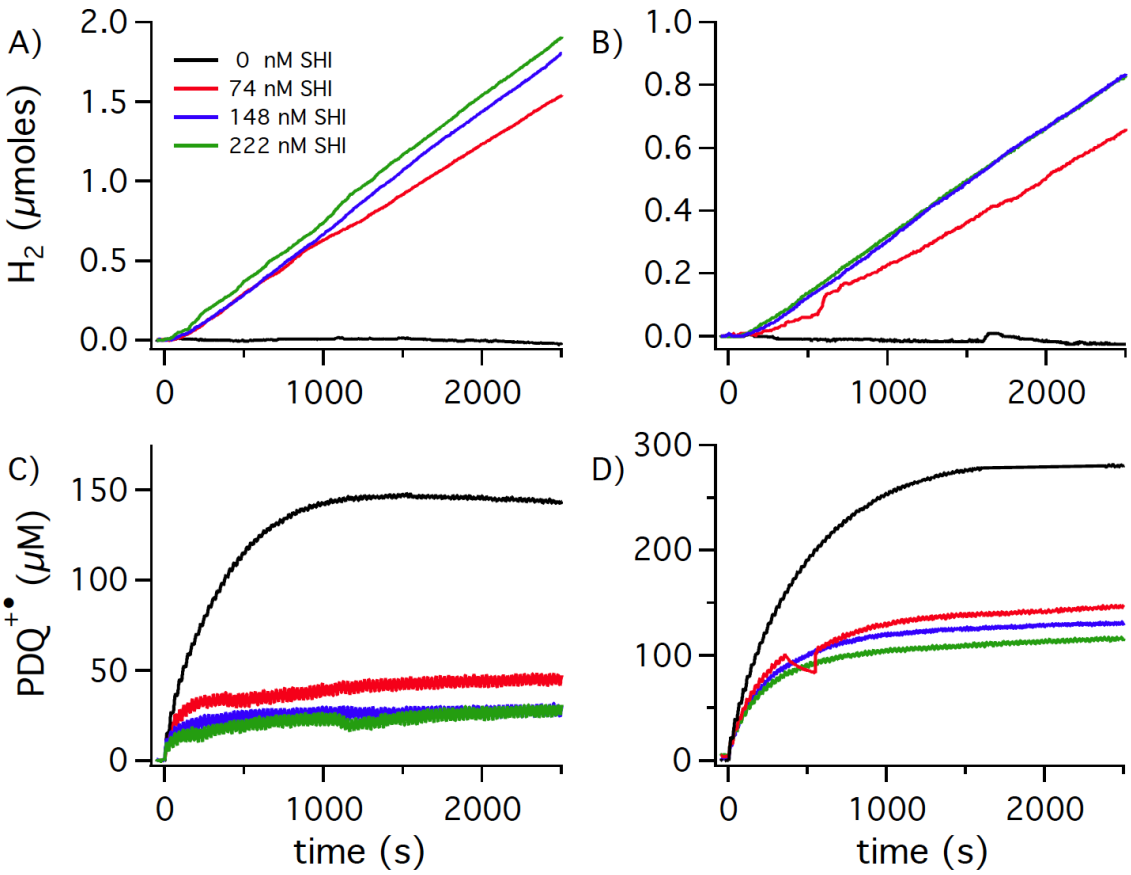

Figure 3.4 – SHI Concentration Dependence of Photocatalytic Hydrogen Production. Quantity of photo-generated H_2 gas (A,B) and concentration of photo-generated $PDQ^{+\bullet}$ (C,D) radical in solution as a function of irradiation time at pH = 7 (A,C) and pH = 8.2 (B,D) with various SHI concentrations. Conditions: 8 mM PDQ^{2+}, 100 mM cysteine, 12 nM MPA-DIR, 50 mM phosphate buffer, excitation source chopped 10 s on / 10 s off with a shutter. The anomaly at 500 s in the 74 nM SHI pH = 8.2 data resulted from a temporary loss of stability of the magnetic stir bar which quickly recovered on resumption of stirring.

off the front face of the cuvette only; the internal quantum efficiency (IQE) refers to the efficiency corrected for both reflection off the front face of the cuvette and for the fraction of light lost to parasitic absorption by the mediator radicals. The initial rate of H_2

production under these conditions corresponds to a QY of 41 ±2 % at pH = 7.35 and 29 ± 2% at pH = 8.39. The higher QY at pH = 7.35 is consistent with the lower steady state $PDQ^{+\bullet}$ concentration at this pH that results from more efficient utilization of the available $PDQ^{+\bullet}$ for proton reduction. Accounting for the internal screening by the $PDQ^{+\bullet}$ absorption yields IQE of 52 ± 2 % at pH = 7.35 and 77 ± 5% at pH = 8.39. Clear advantages emerge in using PDQ^{2+} as a redox mediator to reduce SHI. The ~100 mV of additional driving force[29] beyond MV^{2+} biases the directionality of electron transfer to ensure reduction of the hydrogenase. Despite extraction of this additional energy from the exciton, we observed comparable mediator photoreduction efficiencies for the two mediators.

We also performed hydrogen evolution experiments at various SHI concentrations under similar conditions. Having confirmed by GC that H_2 is the only gas evolved by this system we used a pressure sensing[30] apparatus to detect hydrogen gas evolution. These results and tandem measurements of photo-generated $PDQ^{+\bullet}$ concentration are presented in Figure 3.4. Corresponding corrected efficiencies of H_2 generation are presented in Table 3.2. A general trend of decreasing steady-state $PDQ^{+\bullet}$ concentration with increasing SHI concentration is observed, which correlates with an increased H_2 yield. We attribute the decrease in steady-state $PDQ^{+\bullet}$ concentration to its more rapid consumption by SHI catalyzed proton reduction. At a fixed light flux the lower $PDQ^{+\bullet}$ steady state concentration reduces parasitic screening of the excitation light, resulting in a higher QY for H_2 generation. In particular, the QY between 1000 and 2000 seconds at pH = 7 reflected this trend, rising from 36% to 46% on increasing SHI from 74 nM to 222 nM. Correcting for internal screening by the $PDQ^{+\bullet}$ absorbance results in a shallower

rising trend with the IQE in the same range of conditions rising from 51% to 57%. These trends carry over into alkaline conditions where the IQE of H_2 generation peaks at 63% at 222 nM SHI owing to the higher yield of reduced mediator at alkaline pH.

Table 3.2 – Hydrogen Production Parameters: Quantum yields, internal quantum yields and number of moles of hydrogen produced during the concentration dependent experiments reported in Figure 3.4. Values are reported measuring from the start of illumination to 1000 seconds and 2000 seconds and for the period between 1000-2000 seconds.

		Hydrogen nanomoles	Hydrogen nanomoles	PDQ radical (μM)	PDQ radical (μM)	1000s		2000s		Hydrogen nanomoles	2000s - 1000s	
[SHI] (nM)	pH	1000 s	2000 s	1000 s	2000 s	QY	IQE	QY	IQE	1000s - 2000s	QY	IQE
74	7	666	1310	37	44	0.367	0.496	0.36	0.52	644	0.36	0.51
148	7	710	1523.5	26	26	0.391	0.483	0.42	0.52	813.5	0.45	0.55
222	7	783	1626.7	23	26	0.431	0.520	0.45	0.55	843.7	0.47	0.57
74	8.2	242.8	537	105	113	0.134	0.314	0.15	0.37	294.2	0.16	0.41
148	8.2	324.2	700.8	120	129	0.179	0.474	0.19	0.55	376.6	0.21	0.59
222	8.2	343	705.5	129	142	0.189	0.539	0.19	0.62	362.5	0.20	0.63

3.2.2 – Electron Transfer Dynamics

To gain insight into the carrier dynamics responsible for the comparable photo-reduction efficiencies of PDQ^{2+} and MV^{2+}, we performed femtosecond to microsecond transient absorption (TA) spectroscopy on mediator-DIR complexes assembled in chloroform with excitation at 400 nm. This technique has been shown to be useful for probing intimate details of electron relaxation and transfer dynamics in semiconductor nanostructures and their assemblies.[31-33] Studying a subset of the system assembled in chloroform allows the retention of native phosphonate ligands that do not trap holes and isolation of the charge separation and recombination dynamics between the mediator and DIR in the absence of hole removal or ET to SHI. Incident 400 nm pump photons generate excitons localized primarily in the CdS rod domain of the DIR due to its large volume and dominant absorption at 400 nm, although direct absorption by the CdSe seed can still occur. The initially formed CdS excitons diffuse in the CdS domain[33] and undergo branching to several distinct localized excitonic states driven by hole localization.[32] These states are all capable of participating in electron transfer to surface bound acceptors with distinct rates.

Photo excited electrons in CdSe/CdS nanostructures induce bleaching at the band edge transitions of CdSe and CdS due to state filling of the doubly degenerate 1S and 1s transitions in the rod and seed respectively. The magnitude of these bleaches corresponds to the population of photoexcited electrons.[14] Recovery of this bleach corresponds to depopulation of the excited electron state, either through radiative and non-radiative decay pathways, or through electron/energy transfer to an acceptor. Electron transfer to an acceptor leads to formation of characteristic derivative-like features in the transient

optical spectrum due to Stark effect induced shifting of the exciton transitions.[31] Thus, the dynamics of excited electrons in these materials have well established spectral signatures that can be used to probe their dynamics.

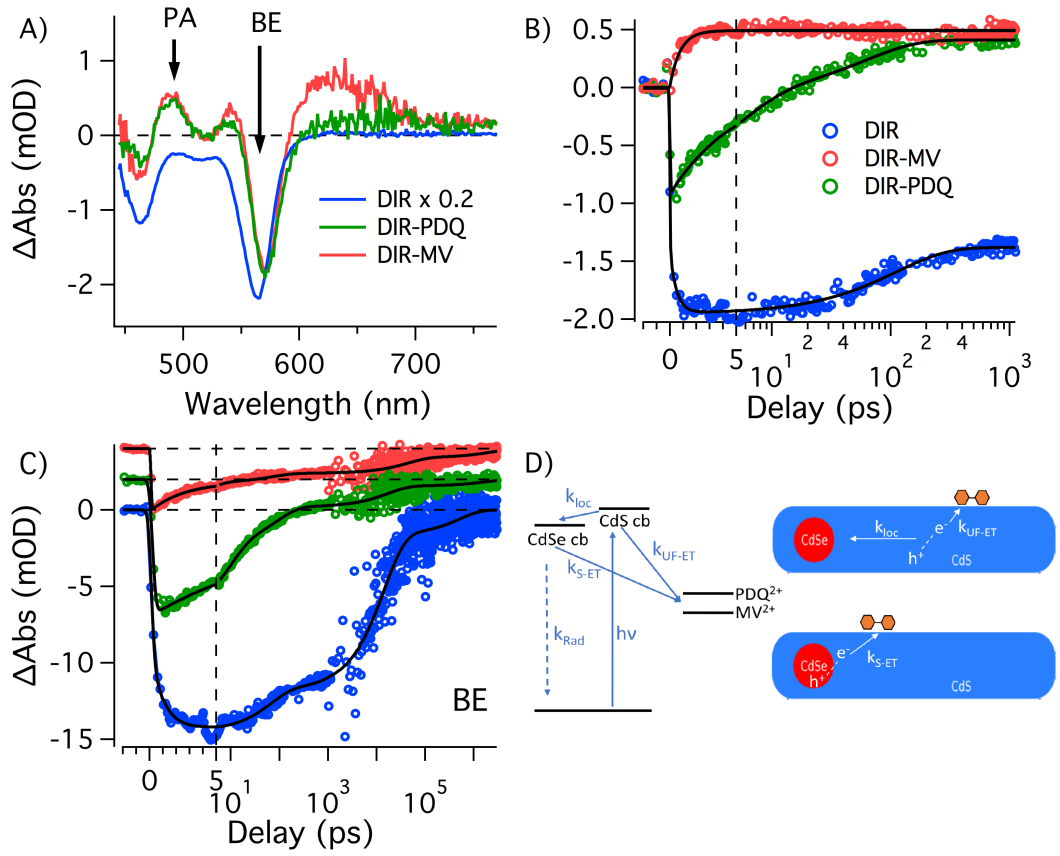

Figure 3.5 - Ultrafast transient absorption of mediator-DIR complexes. (A) Transient absorption spectra for DIR, DIR-PDQ^{2+} and DIR-MV^{2+} complexes averaged from 800 ps to 1 ns. (B) Transient absorption of the PA (photoinduced absorption) feature for DIR, DIR-PDQ^{2+} and DIR-MV^{2+} complexes probed at 490 nm. (C) Transient absorption of the band edge (BE) feature probed at 565 nm. (D) Qualitative energy level diagram and schematic representation of the electron transfer processes that occur between photo-excited DIR and mediator. Vertical dashed lines denote a break between linear and logarithmic scaling of the time axes.

TA spectra of the DIR and DIR-mediator complexes averaged from 0.8-1 ns are shown in Figure 3.5A. The DIR spectrum in the absence of mediators shows features associated with long-lived excitonic states where the electron has localized in the CdSe core and at the CdSe/CdS interface.[32] Both the DIR-PDQ^{2+} and DIR-MV^{2+} complexes show similar spectral features to each other but they are highly distinct from the DIR alone. The red-shifted bleach feature and derivative-like features are consistent with the charge separated state subsequent to ET to an electron acceptor.[31] Additionally, a spectral contribution of the $MV^{+\bullet}$ radical is evident as a photoinduced absorption at >600 nm in the DIR-MV^{2+} complex. This radical absorption feature is not as well resolved in the DIR-PDQ^{2+} complex, which is reasonable given the 3-fold smaller extinction of $PDQ^{+\bullet}$ and its broad and shifted absorption features (Fig. 3.1D). The similarity of the DIR-MV^{2+} and DIR-PDQ^{2+} transient spectra provides unambiguous evidence that the spectral features in the DIR-PDQ^{2+} also correspond to the charge separated state. After establishing the spectral features associated with ET in these systems the charge separation process was followed by probing the formation of the photoinduced absorption feature (PA) at 490 ± 5 nm that is characteristic of the charge separated state in DIR complexes of either mediator. The PA transients were fit to sums of exponentials convolved with an instrument response function as shown in Figure 3.5AB.

For DIR in absence of mediators, a strong bleaching signal grows in at early time and persists for the duration of the measurement time window. A rising component of 595 ± 390 fs is attributed to exciton localization dynamics that occurs within the first picosecond leading to localization of electrons around the CdSe seed.[32] A small amplitude decay with a lifetime of 110 ± 21 ps is also observed, attributed to a minor

component of biexciton decay due to Auger recombination, similar to related CdSe/CdS nanomaterials.[34] The persistence of the bleaching signal corresponds to long lived excitons localized to the CdSe seed or the CdSe- CdS interface that recombine on a longer timescale.

In the presence of electron acceptors the PA dynamics are significantly modified. The crossing of the PA signal from bleach to induced absorption provides a clear signature of the ET process. Both mediator-DIR complexes show significant bleaching amplitude missing at early delay time. This can be attributed to ultrafast (within the 100 fs instrument response) ET from excitons initially formed in the CdS domain, preceding exciton localization. For the MV^{2+}-DIR complex the bleaching signal is completely suppressed and an induced absorption signal is observed that can be fit to a single exponential with $\tau = 794 \pm 210$ fs. These PA dynamics also coincide with formation of the spectrum of the charge-separated state (Fig. 3.5A,B). Therefore, we assign these PA dynamics to ultrafast ET from the photo-excited CdS domain to adsorbed MV^{2+} resulting in a long-lived charge-separated state that persists beyond the experimental time window. Substantially different PA dynamics are observed for the photoexcited PDQ^{2+}-DIR complex. Coincident with the instrument response a bleaching signal forms with an amplitude of roughly 50% that of the free DIR. This implies a substantial fraction of PDQ^{2+}-DIR undergoes a sub-picosecond ET process analogous to the ultrafast ET process in the MV^{2+}-DIR complex. The PA signal then undergoes a biphasic recovery with an amplitude weighted lifetime (AWL) of 25.0 ± 2.8 ps, after which the spectrum of the charge separated state is fully formed and persists for the duration of the time window.

To probe recombination of the long-lived charge separated states in this system, nanosecond to microsecond transient absorbance (ns-TA) was also performed. Figure 3.5C shows the fs-TA dynamics probed at the band edge (BE) bleaching feature (565 ± 5 nm) concatenated with the ns-TA dynamics of the charge-separated state as described in the SI. The dynamics up to 1 ns are nearly identical to the PA dynamics and support the above interpretation. Interestingly, the MV^{2+}-DIR band edge transient shows an additional small decay component with an AWL of 7 ± 2.1 ps. We assign this small phase to ET from excited electrons generated in the CdSe seed by direct photoexcitation of CdSe. These electrons transfer on a slower timescale due to the tunneling barrier imposed by the CdS shell that encases the CdSe domain. This process is a sufficiently small part of the total ET, which primarily occurs in the initial ultrafast phase, such that an appreciable contribution of this process to the PA signal is not resolved. In summary, within one hundred picoseconds of photo-excitation, only the charge-separated state is observed in DIR complexes of either mediator. Subsequent spectral evolution consists only of decay of the charge-separated state by recombination of the mediator-localized cation radical and the hole. These recombination dynamics were modeled as biexponential functions in the coupled model and gave rise to amplitude-weighted lifetimes of 898 ± 144 ns and 451 ± 149 ns for MV^{2+} and PDQ^{2+} respectively.

The TA results indicate why we observe nearly equal net efficiencies for the reduction of the PDQ^{2+} and MV^{2+} acceptors by photo-excited DIR. The fraction of ultrafast ET from excitons generated in the CdS rod to the mediator is significantly greater for MV^{2+} than for PDQ^{2+}. In the DIR-PDQ^{2+} complex, some fraction of excitons still localize to the seed before ET to PDQ^{2+}, reminiscent of the competition between

branching to core exciton localization and ET in CdSe tetrapods and the disparity observed in ET between methylene blue and MV^{2+}.[35] Nevertheless, the remaining seed and interface-localized electrons transfer to the acceptors within tens of picoseconds in both cases, effectively outcompeting other relaxation processes. A qualitative energy level diagram and schematic in Figure 3.5D depicts these charge separation processes. Here $k_{UF\text{-}ET}$ represents the ultrafast ET process from excitons in the CdS to directly reduce the mediator. The exciton localization process from CdS to CdSe is represented by $k_{loc,}$ and $k_{S\text{-}ET}$ is the slower electron transfer process from these CdSe localized states. Decay of the charge-separated state occurs on the hundreds of nanoseconds timescale for DIR complexes of both mediators. In DIR-MV^{2+} the charge separation lifetime is twice as long as for DIR-PDQ^{2+}. We suspect this is because a larger fraction of ET originates from the ultrafast ET processes in DIR-MV^{2+}, resulting in greater average spatial separation between the mediator localized electron and the CdSe seed localized hole. Similar phenomena have resulted when these states are selectively generated through control over excitation energy.[36]

3.2.3 – Hole Transfer Dynamics

Despite the disparity in recombination rates detailed in sections 3.2.2, equal efficiencies of photoreduction are still observed because hole filling by thiolate ligands is expected to be three orders of magnitude faster (~300 ps) than recombination of the charge separated state in these nanostructures.[14] This conclusion is supported by ps time-resolved fluorescence measurements that probe the hole transfer kinetics as a function of

the surface chemistry and environment of the DIR structures which are detailed in the figure 3.6

The photoluminescence decays in figure 3.6 were fit to function of the form (1) where *n* was selected to obtain randomly distributed residuals over the whole decay trace.

(1) $$f(t) = y_0 + \sum_{n=4} a_n \exp\left(\frac{(t - t_0)}{\tau_n}\right)$$

Amplitude weighted lifetimes were the calculated for each trace by (2) where a_n is the amplitude of the exponential component and τ_n is the lifetime of the exponential component.

(2) $$\tau_{awl} = \frac{\sum_n a_n \tau_n}{\sum_n a_n}$$

The different surface chemistry conditions of the DIR structures are assumed to modify pathways for hole transfer from the nanostructure[37]. Exchange of native hydrophobic ligands with the hydrophilic thiol glutathione is observed to shorten the PL decay, presumably due to transfer of holes that would normally radiatively recombine with the excited electron. Addition of 50mM cysteine to the solution shortens the lifetime consistent with its performance as a more effective sacrificial electron donor. The mechanism responsible for this dramatic difference in hole transfer rates between glutathione and cysteine is beyond the scope of these studies but may be due to the smaller size of cysteine allowing for greater surface density of ligands to be achieved or differences in electronic structure between the two thiol ligands.

Hole transfer time can be calculated by assuming thiol binding creates an additional channel for non-radiative decay of the fluorescence by hole transfer using the relation (3).

(3) $$\tau_{HT} = \left(\frac{1}{\tau_{DIR+thiol}} - \frac{1}{\tau_{DIR}} \right)^{-1}$$

Table 3.3 Hole Transfer Parameters for Thiol Capped CdSe/CdS DIR

Sample	τ_{HT}
GSH capped DIR	7.79 ns
GSH capped DIR in 50mM Cys	0.383 ns

3.2.4 – pH Dependence and Energetics

The rate of proton reduction by DIR-PDQ^{2+}-SHI at a given excitation light flux is strongly pH dependent. The pH dependence of the initial rates of proton reduction in the

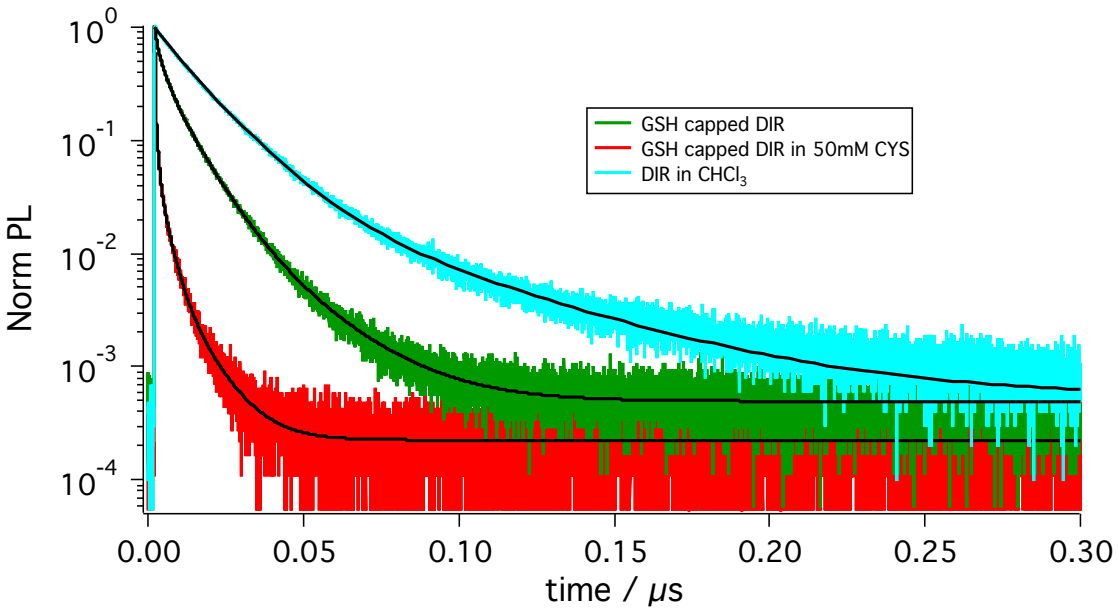

Figure 3.6 - Normalized photoluminescence dynamics of DIR structures excited at 405 nm monitored by TCSPC.

SHI-DIR system using both cysteine and glutathione as SED are presented in Figure 3.7. The initial proton reduction rate peaks between pH = 6 - 7. This is likely a manifestation of two factors. First, the efficiency of steady-state photo-reduction of the mediator decreases as the pH is decreased (Fig. 3.1D, inset), limiting the efficiency at lower pH. This is likely a consequence of reduced ligand coverage of the DIR at lower pH as the capping group thiolates get protonated,[17] inhibiting their ability to scavenging activity far from pH = 4.5.[38] Hole scavenging is more efficient at higher pH since surface bound anionic thiolates are the active hole scavenging species[26] and in solution there is a higher population of deprotonated thiol which can readily replace ligands lost to disulfide

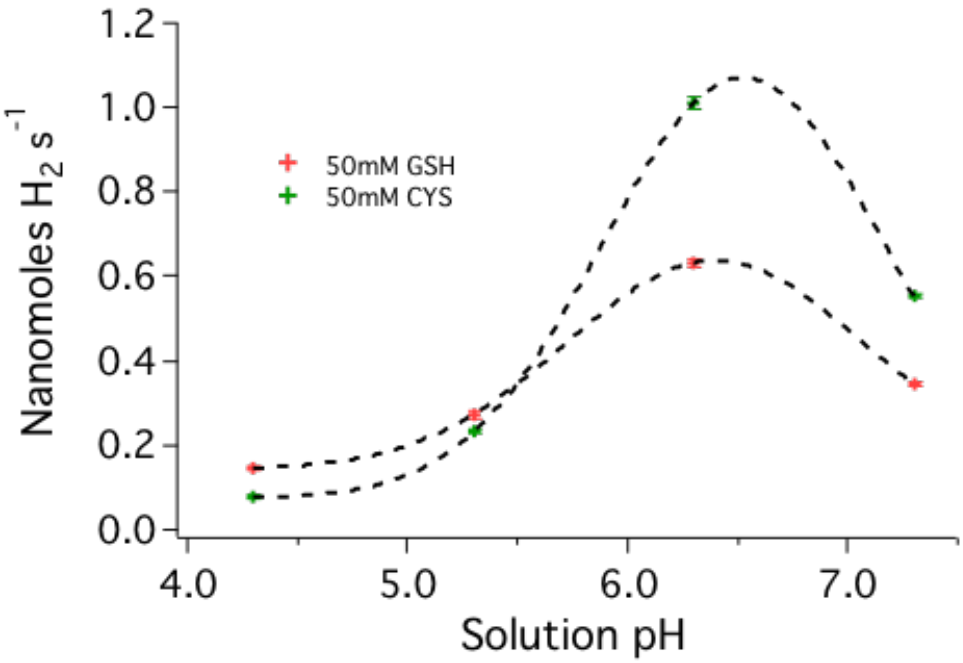

Figure 3.7 - pH Dependence of the H_2 Production rate as a function of pH of the sacrificial donor solution. Conditions SHI = 230 nM, DIR = 12 nM, PDQ^{2+} = 50 mM, Donor = 50mM, Buffer = 50 mM Phosphate/Citrate, 4.3 mW 405 nm excitation. Fits to Gaussian functions are meant to guide the eye and do not have physical significance.

formation. At low pH, thiolate protonation to form thiol and ligand desorption from the nanocrystal surface[17] decrease the available hole transfer pathways, promoting nanocrystal photo-corrosion and aggregation. Second, the proton reduction reaction itself is energetically more favorable at lower pH, reflecting the 59 mV/pH dependence of the ($H_2/2H^+$) redox couple. The positive shift in the ($H_2/2H^+$) reduction potential at lower pH raises the solution reduction potential required to drive hydrogen evolution and thus lowers the radical concentration required to drive it. The turnover frequency of SHI also increases with decreasing pH although this is not a strong dependence in *Pf* SHI.[39] The competition between these two anti-correlated trends leads to the observed pH dependence of the H_2 production rate with a maximum where the two effects minimally interfere and is clearly observed in Fig. 3.7 for both cysteine and glutathione SEDs. Diminishing rates are observed upon deviation from this pH value.

The significant disparity between H_2 production efficiencies for the two mediators is explained by the solution electrochemical potential imposed by the ($PDQ^{2+}/PDQ^{+\bullet}$) and ($MV^{2+}/MV^{+\bullet}$) redox couples under photocatalytic conditions. According to the Nernst relation (1) the solution electrochemical potential is governed by the relative concentrations of electro-active species and their midpoint potential at equilibrium.

(1) $$E = E_0 + \frac{RT}{nF}\ln\left(\frac{[\text{Oxidized}]}{[\text{Reduced}]}\right)$$

The mediator redox couples are in rapid equilibrium with the SHI electron transfer chain and active site[39] and thus effectively impose the solution electrochemical potential on the catalyst, SHI, despite the presence of other molecules that are, in principle, redox active[40] (e.g. thiols) but are kinetically irrelevant. Equation (1) was used to transform the time dependent radical concentrations reported in Fig 3.3 to the time dependent solution electrochemical potential shown in Figure 3.8.

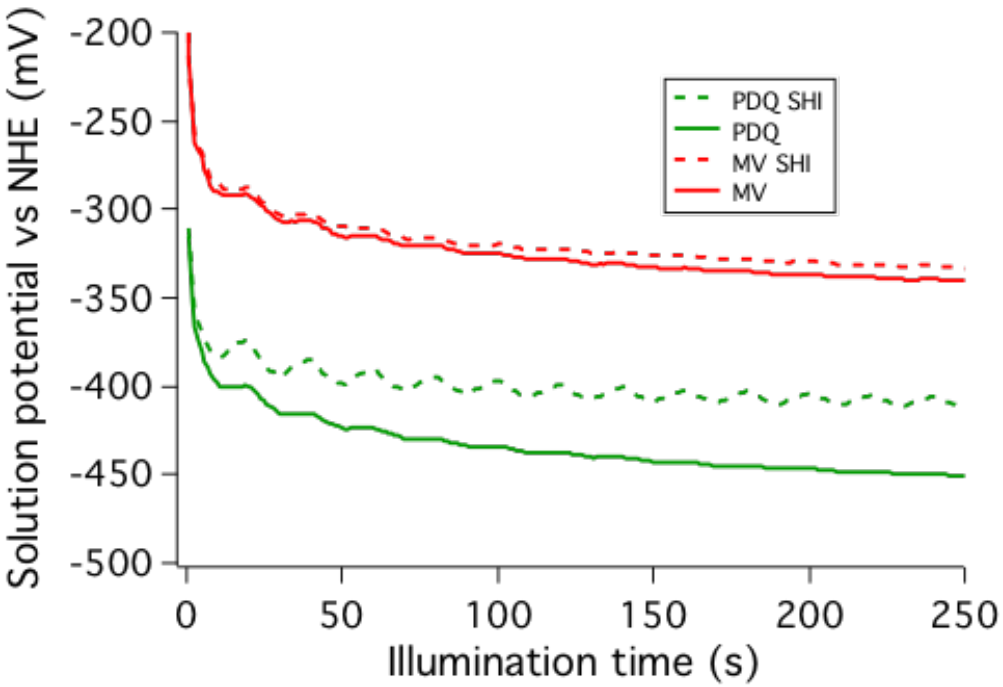

Figure 3.8 - Nernstian potential imposed by the mediator redox couples under the conditions in Fig. 3.7 at pH = 7.35 under identical photoexcitation conditions.

The results clearly demonstrate the advantage of the PDQ^{2+} mediated photocatalytic system. For all illumination times, the PDQ^{2+}-DIR system achieves a more cathodic potential than the MV^{2+}-DIR system, which imposes an overpotential on SHI and biases the catalyst towards proton reduction. In principle, the MV^{2+}-DIR system can also attain such cathodic potentials, however this would require more than half of the MV^{2+} in solution to be reduced to the radical form. Internal screening of the excitation

light by the radical visible absorbance becomes overwhelming at these higher radical concentrations (>99% @ 405 nm), due to its extinction coefficient of >10 $mM^{-1}cm^{-1}$ across much of the visible spectrum. This inner filter effect highlights a further advantage of the PDQ^{2+} mediator since 1) the consumption of $PDQ^{+\bullet}$ by SHI turnover prevents buildup of high concentrations of the radical that could screen excitation light and 2) the $PDQ^{+\bullet}$ radical has 3-fold smaller extinction than the $MV^{+\bullet}$ radical across the visible spectrum which further reduces screening. The smaller $PDQ^{+\bullet}$ radical extinction is likely due to the twisted geometry of the bipyridyl rings imposed by the propyl bridge between the N atoms that reduces the overlap of the ring π^* orbitals containing the radical spin density.

3.2.5 – Stability of the Photochemical System

The DIR-PDQ^{2+}-SHI system is highly robust. Long term H_2 production was monitored by headspace pressure[30] change since H_2 was the only gaseous product observed by GC sampling. We observed continuous H_2 production over the course of 385

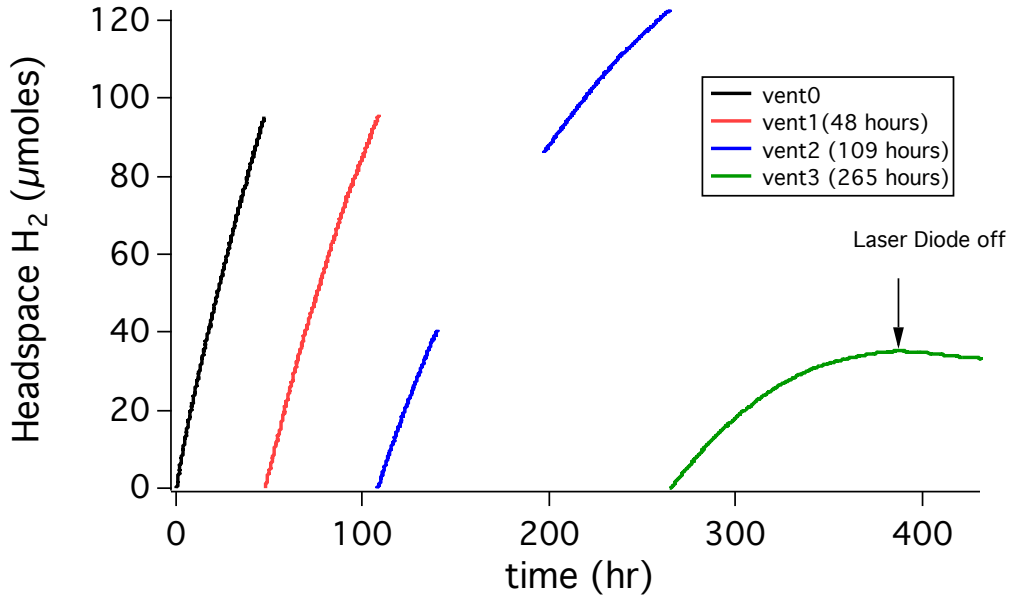

Figure 3.9 - Time dependent photo-production of hydrogen from hybrid assemblies. Moles of hydrogen produced, measured by headspace pressure. The data trace from 141-197 hours was lost due to crashing of the data collection programs, however this does not affect the measurement for hydrogen produced at other times or the yield calculated.

hours (~16 days) under 450 nm illumination, corresponding to a TON of 1.1 x 10^6 on a per SHI basis or 28 on a per PDQ basis as shown in Figure 3.9. This TON represents a lower limit imposed by PDQ^{2+} stability since addition of PDQ^{2+} to the system regenerated substantial activity. These results highlight the high stability of the DIR-PDQ^{2+}-SHI system and improvement over previous [NiFe] H_2ase/nanoparticle based systems.[3, 18] Importantly, unlike previous reports where enzyme inactivation was attributed to thiol or oxidized thiol,[3-4] the present system competently operates at high thiol concentrations and under continuous generation of thyil-radical species,[26] suggesting SHI is not susceptible to this inactivation mechanism.

Activity diminishes slightly over the course of several hours following the start of photocatalysis. We attribute this decline in rate of H_2 production to two factors. First, we observe product inhibition as the H_2 pressure builds up in the cell. For a multi-day run, the headspace of the cell was vented periodically in an anaerobic chamber to prevent cell breakage from excess pressure. The venting procedure resulted in an increase in the H_2 production rate, consistent with product inhibition at high H_2 partial pressure (>1.5 atm H_2). The second, more significant contribution to the decline in activity is a decrease in light absorption by the DIR caused by buildup of a degradation product of PDQ^{2+} that absorbs strongly at the excitation wavelength of 405 nm and eventual depletion of the available pool of PDQ^{2+}. A similar decline was observed in steady-state photoreduction experiments with DIR-PDQ^{2+} without SHI, manifest as saturation in $PDQ^{+\bullet}$ concentration at long illumination times and concomitant formation of a new absorption band at 404 nm assigned to the degradation product shown in Figure 3.10. Degradation of the cation radical in solution has been observed previously in a structurally related redox mediator.[41] Formation of this degradation product absorption is coupled to a decline in the steady state $PDQ^{+\bullet}$ concentration observed over the same period due to a reduced rate of productive photon absorption.

These results suggest that the current system is limited by the stability of the $PQD^{+\bullet}$ radical itself. The impact of $PDQ^{+\bullet}$ degradation is diminished in the presence of SHI since the catalyst rapidly scavenges the radical and enforces a lower steady-state radical concentration, thereby minimizing the deleterious effects of this pathway (Fig. 3.3C). Mediator stability may represent a fundamental limitation of this type of photocatalytic system, as more reactive radical carriers may be inherently less stable.

Future work will examine the effects of further variation of mediator structure in this system to promote mediator stability while retaining high photoreduction efficiency and favorable driving force for catalysis.

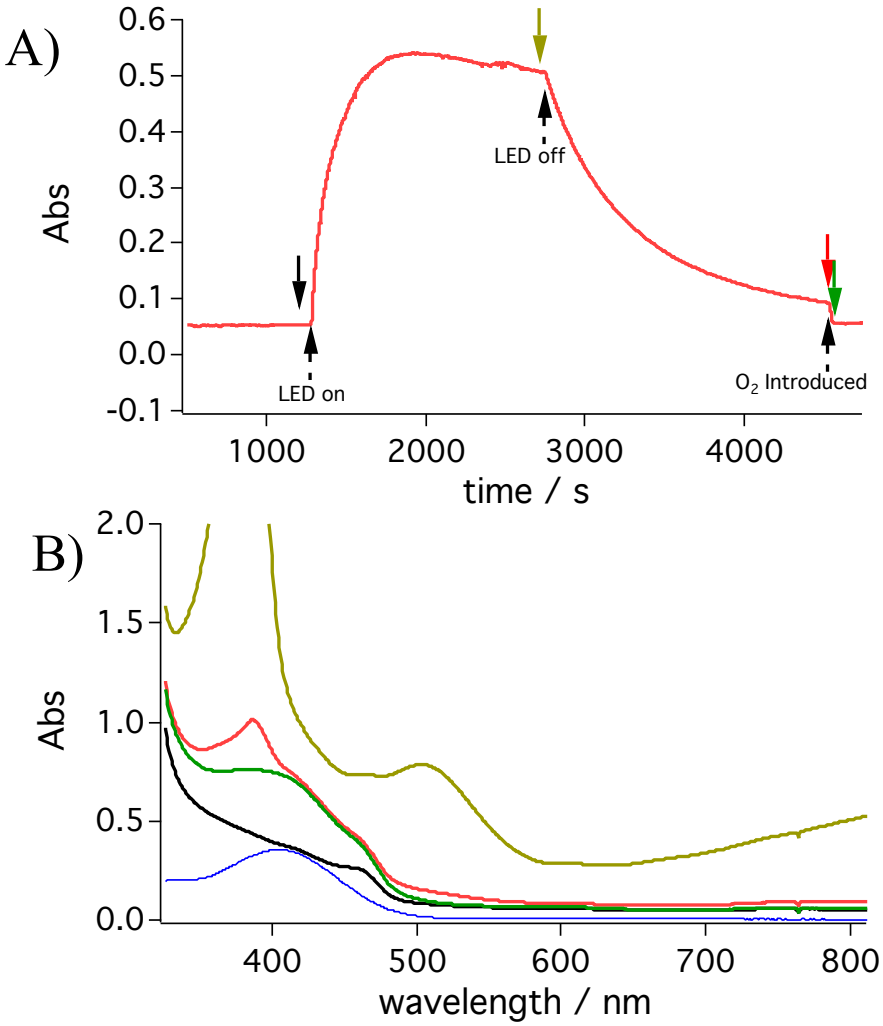

Figure 3.10. Degradation Product of PDQ^{2+} (A) Absorbance at 800 nm of glutathione capped CdS in 0.5M Glutathione pH = 6.8 with 7.14mM PDQ^{2+} under 4.04 mW 405 nm laser diode illumination. (B) Absorbance spectra at selected points from trace in panel (A) designated by downward pointing color coded arrows. The blue trace represents the difference spectrum between the sample before illumination and after quenching with oxygen, showing the buildup of the PDQ^{2+} degradation product.

An important factor in maximizing the efficiency of photocatalytic systems, for both sacrificial and full water splitting systems is the management of unproductive side reactions and reactive intermediates.[42] A likely contributor to the stability of the reported system is an efficient pathway for managing the oxidizing equivalents generated during catalysis. Single hole transfer reactions generate a thyil radical which, were it allowed to diffuse freely, could degrade components of the photocatalytic system. Thyil radicals can react with C-H bonds in H_2ase, generating carbon-centered radicals and possibly irreversible damage to the enzyme. We do not observe degradation of the H_2ase in our experiments, even for very large TON of the enzyme. Previous studies indicate that the cadmium chalcogenide surface of the DIR prevents release of the thyil radicals by confining them to the nanoparticle surface and facilitating their quantitative conversion to stable disulfide product.[26] Clean conversion of the sacrificial donor to a stable oxidation product[42-43] and sequestration of the reactive intermediates in the process both provide important contributions to the stability of the photocatalytic system.

3.3 – Conclusions

We provide a thorough characterization of the factors that lead to the high efficiency of hydrogen production in the PDQ-DIR-SHI system, probing the charge transfer processes across many decades in time and using *in situ* spectroscopic observation to probe time-dependent radical concentrations and how the optical properties of the mediator impact the efficiency. These results provide guiding principles that can be widely applied in photocatalytic systems. First, we find it is critical to control the cation radical concentration required to drive catalysis so that it does not significantly

suppress the productive absorption of light by the semiconductor. We demonstrate that this can be accomplished through modulation of both the energetics and optical properties of the mediator. Second, we demonstrate that it is possible to extract more free energy from the photosensitizer excited state to drive subsequent ET to the catalyst due to the unique photophysical properties of the DIR structure. Finally, we use the more negative redox mediator midpoint potential to effectively rectify the direction of catalysis towards H_2 production[44] in a [NiFe] H_2ase that is normally biased towards H_2 oxidation through controlling the potential of electrons entering the catalyst.[45] This approach achieves unprecedented efficiency of H_2 production.

The photochemical system is distinct from electrochemical examples using a low potential mediator to drive catalysis, as recently for nitrogenase,[46] or from the use of the mediators to facilitate electron transfer from a kinetically slow, low potential, chemical reductant.[47-48] In the electrochemical case, an excess potential is applied to the electrode to reduce a low potential mediator, which is an extra energy input even beyond any excess potential applied to overcome kinetic barriers associated with charge transfer. This constitutes a loss in efficiency if the goal is energy conversion and fuel production. In the present case, the excess free energy exploited to reduce the low potential mediator is intrinsic to the conduction band of the chosen semiconductor.

It seems unlikely that driving force dependence alone can account for the differing electron transfer mechanisms of PDQ^{2+} and MV^{2+} given the highly reducing nature of the CdSe/CdS conduction band electron (~ -1 V). We are currently investigating whether there are additional contributions from electronic coupling of the mediator to the nanorod frontier orbitals that depend on the conformation of the mediator on the surface

of the CdS lattice.[25] Hole removal is key for efficiency[49] since ET easily outcompetes recombination due to greater than microsecond charge separation lifetimes in PDQ^{2+}-DIR complexes.

These results demonstrate the advantage of DIR structures for redox-mediated photocatalysis. We demonstrate that additional driving force for catalysis can be extracted from these systems with minimal penalty of efficiency due to the preservation of ultrafast ET and long-lived charge separation. Our results demonstrate that simple modifications of the redox mediator linking the photosensitizer with the catalyst can lead to substantial improvements in photocatalytic activity. Future work will explore additional mediator/ semiconductor combinations that can preserve these features and further increase the efficiency and stability of these systems. Future work will also address using this system for photo-triggered mechanistic studies of the hydrogenase catalytic mechanism.

3.4 – References

1. Oreskes, N., The Scientific Consensus on Climate Change. *Science* **2004,** *306* (5702), 1686.

2. Lubitz, W.; Tumas, W., Hydrogen: An Overview. *Chem. Rev.* **2007,** *107* (10), 3900-3903.

3. Greene, B. L.; Joseph, C. A.; Maroney, M. J.; Dyer, R. B., Direct Evidence of Active-Site Reduction and Photodriven Catalysis in Sensitized Hydrogenase Assemblies. *J. Am. Chem. Soc.* **2012,** *134* (27), 11108-11111.

4. Brown, K. A.; Wilker, M. B.; Boehm, M.; Dukovic, G.; King, P. W., Characterization of Photochemical Processes for H2 Production by CdS Nanorod–[FeFe] Hydrogenase Complexes. *J. Am. Chem. Soc.* **2012,** *134* (12), 5627-5636.

5. Kalisman, P.; Nakibli, Y.; Amirav, L., Perfect Photon-to-Hydrogen Conversion Efficiency. *Nano Lett.* **2016,** *16* (3), 1776-1781.

6. Lubitz, W.; Ogata, H.; Rüdiger, O.; Reijerse, E., Hydrogenases. *Chem. Rev.* **2014,** *114* (8), 4081-4148.

7. Brown, K. A.; Harris, D. F.; Wilker, M. B.; Rasmussen, A.; Khadka, N.; Hamby, H.; Keable, S.; Dukovic, G.; Peters, J. W.; Seefeldt, L. C.; King, P. W., Light-driven dinitrogen reduction catalyzed by a CdS:nitrogenase MoFe protein biohybrid. *Science* **2016,** *352* (6284), 448-450.

8. Brown, K. A.; Wilker, M. B.; Boehm, M.; Hamby, H.; Dukovic, G.; King, P. W., Photocatalytic Regeneration of Nicotinamide Cofactors by Quantum Dot–Enzyme Biohybrid Complexes. *ACS Catal.* **2016,** *6* (4), 2201-2204.

9. Wilker, M. B.; Shinopoulos, K. E.; Brown, K. A.; Mulder, D. W.; King, P. W.; Dukovic, G., Electron transfer kinetics in CdS nanorod-[FeFe] hydrogenase complexes and implications for photochemical H2 generation. *J. Am. Chem. Soc.* **2014**.

10. Hutton, G. A. M.; Reuillard, B.; Martindale, B. C. M.; Caputo, C. A.; Lockwood, C. W. J.; Butt, J. N.; Reisner, E., Carbon Dots as Versatile Photosensitizers for Solar-Driven Catalysis with Redox Enzymes. *J. Am. Chem. Soc.* **2016,** *138* (51), 16722-16730.

11. Sakai, T.; Mersch, D.; Reisner, E., Photocatalytic Hydrogen Evolution with a Hydrogenase in a Mediator-Free System under High Levels of Oxygen. *Angew. Chem., Int. Ed.* **2013,** *52* (47), 12313-12316.

12. Selvaggi, A.; Tosi, C.; Barberini, U.; Franchi, E.; Rodriguez, F.; Pedroni, P., In vitro hydrogen photoproduction using Pyrococcus furiosus sulfhydrogenase and TiO2. *J. Photochem. Photobiol., A* **1999,** *125* (1–3), 107-112.

13. Chandrayan, S. K.; McTernan, P. M.; Hopkins, R. C.; Sun, J.; Jenney, F. E.; Adams, M. W. W., Engineering Hyperthermophilic Archaeon Pyrococcus furiosus to Overproduce Its Cytoplasmic [NiFe]-Hydrogenase. *J. Biol. Chem.* **2012,** *287* (5), 3257-3264.

14. Zhu, H.; Song, N.; Lv, H.; Hill, C. L.; Lian, T., Near Unity Quantum Yield of Light-Driven Redox Mediator Reduction and Efficient H2 Generation Using Colloidal Nanorod Heterostructures. *J. Am. Chem. Soc.* **2012,** *134* (28), 11701-11708.

15. Esswein, A. J.; Nocera, D. G., Hydrogen Production by Molecular Photocatalysis. *Chem. Rev.* **2007,** *107* (10), 4022-4047.

16. Ebbesen, T. W., Interference of hydrogen with the electron transfer to colloidal platinum catalyst and consequences for photochemical water reduction. *J. Phys. Chem.* **1984,** *88* (18), 4131-4135.

17. Aldana, J.; Lavelle, N.; Wang, Y.; Peng, X., Size-Dependent Dissociation pH of Thiolate Ligands from Cadmium Chalcogenide Nanocrystals. *J. Am. Chem. Soc.* **2005,** *127* (8), 2496-2504.

18. Brown, K. A.; Dayal, S.; Ai, X.; Rumbles, G.; King, P. W., Controlled Assembly of Hydrogenase-CdTe Nanocrystal Hybrids for Solar Hydrogen Production. *J. Am. Chem. Soc.* **2010,** *132* (28), 9672-9680.

19. Ogata, H.; Kellers, P.; Lubitz, W., The Crystal Structure of the NiFe Hydrogenase from the Photosynthetic Bacterium Allochromatium vinosum: Characterization of the Oxidized Enzyme (Ni-A State). *J. Mol. Biol.* **2010,** *402* (2), 428 - 444.

20. Launikonis, A.; Loder, J. W.; Mau, A. W. H.; Sasse, W. H. F.; Wells, D., Improved Hydrogen Production with Tetramethyl-and Hexamethylviologen as Electron-Transfer Agents in the System H2O-Ru(bpy)2+3-edta-Pt. *Isr. J. Chem.* **1982,** *22* (2), 158-162.

21. Amouyal, E.; Zidler, B.; Keller, P.; Moradpour, A., Excited-state electron-transfer quenching by a series of water photoreduction mediators. *Chem. Phys. Lett.* **1980,** *74* (2), 314-317.

22. Amouyal, E.; Zidler, B.,On the Effect of Electron Relay Redox Potential on the Electron Transfer Reactions in a Water Photo-reduction Model System. *Isr. J. Chem.* **1982,** *22* (2), 117-124.

23. Keller, P.; Moradpour, A.; Amouyal, E.; Kagan, H., Visible-Light Photo-Reduction of Water: Hydrogen Formation Yields as a Function of the structure of the Viologen-Dye Relays. *J. Mol. Catal.* **1980,** *7* (4), 539-542.

24. Amouyal, E.; Koffi, P., Photochemical production of hydrogen from water. *J. Photochem.* **1985,** *29* (1), 227-242.

25. Peterson, M. D.; Jensen, S. C.; Weinberg, D. J.; Weiss, E. A., Mechanisms for Adsorption of Methyl Viologen on CdS Quantum Dots. *ACS Nano* **2014,** *8* (3), 2826-2837.

26. Li, X.-B.; Li, Z.-J.; Gao, Y.-J.; Meng, Q.-Y.; Yu, S.; Weiss, R. G.; Tung, C.-H.; Wu, L.-Z., Mechanistic Insights into the Interface-Directed Transformation of Thiols into Disulfides and Molecular Hydrogen by Visible-Light Irradiation of Quantum Dots. *Angew. Chem., Int. Ed.* **2014,** *53* (8), 2085-2089.

27. Tajc, S. G.; Tolbert, B. S.; Basavappa, R.; Miller, B. L., Direct Determination of Thiol pKa by Isothermal Titration Microcalorimetry. *J. Am. Chem. Soc.* **2004,** *126* (34), 10508-10509.

28. Tang, S.-S.; Chang, G.-G., Kinetic Characterization of the Endogenous Glutathione Transferase Activity of Octopus Lens S-Crystallin1. *J. Biochem.* **1996,** *119* (6), 1182-1188.

29. Tsukahara, K.; Wilkins, R. G., Kinetics of reduction of eight viologens by dithionite ion. *J. Am. Chem. Soc.* **1985,** *107* (9), 2632-2635.

30. Han, Z.; Qiu, F.; Eisenberg, R.; Holland, P. L.; Krauss, T. D., Robust Photogeneration of H2 in Water Using Semiconductor Nanocrystals and a Nickel Catalyst. *Science* **2012,** *338* (6112), 1321-1324.

31. Zhu, H.; Song, N.; Lian, T., Wave Function Engineering for Ultrafast Charge Separation and Slow Charge Recombination in Type II Core/Shell Quantum Dots. *J. Am. Chem. Soc.* **2011,** *133* (22), 8762-8771.

32. Wu, K.; Rodríguez-Córdoba, W. E.; Liu, Z.; Zhu, H.; Lian, T., Beyond Band Alignment: Hole Localization Driven Formation of Three Spatially Separated Long-Lived Exciton States in CdSe/CdS Nanorods. *ACS Nano* **2013,** *7* (8), 7173-7185.

33. Utterback, J. K.; Grennell, A. N.; Wilker, M. B.; Pearce, O. M.; Eaves, J. D.; Dukovic, G., Observation of trapped-hole diffusion on the surfaces of CdS nanorods. *Nat. Chem.* **2016,** *8* (11), 1061-1066.

34. Greytak, A. B.; Allen, P. M.; Liu, W.; Zhao, J.; Young, E. R.; Popovic, Z.; Walker, B. J.; Nocera, D. G.; Bawendi, M. G., Alternating layer addition approach to CdSe/CdS core/shell quantum dots with near-unity quantum yield and high on-time fractions. *Chem. Sci.* **2012,** *3* (6), 2028-2034.

35. Yang, Y.; Wu, K.; Chen, Z.; Jeong, B.-S.; Lian, T., Competition of branch-to-core exciton localization and interfacial electron transfer in CdSe tetrapods. *Chem. Phys.* **2016,** *471*, 32-38.

36. Zhu, H.; Chen, Z.; Wu, K.; Lian, T., Wavelength dependent efficient photoreduction of redox mediators using type II ZnSe/CdS nanorod heterostructures. *Chem. Sci.* **2014,** *5* (10), 3905-3914.

37. Wuister, S. F.; de Mello Donegá, C.; Meijerink, A., Influence of Thiol Capping on the Exciton Luminescence and Decay Kinetics of CdTe and CdSe Quantum Dots. *The Journal of Physical Chemistry B* **2004,** *108* (45), 17393-17397.

38. Reynal, A.; Pastor, E.; Gross, M. A.; Selim, S.; Reisner, E.; Durrant, J. R., Unravelling the pH-dependence of a molecular photocatalytic system for hydrogen production. *Chem. Sci.* **2015,** *6* (8), 4855-4859.

39. Greene, B. L.; Wu, C.-H.; McTernan, P. M.; Adams, M. W. W.; Dyer, R. B., Proton-Coupled Electron Transfer Dynamics in the Catalytic Mechanism of a [NiFe]-Hydrogenase. *J. Am. Chem. Soc.* **2015,** *137* (13), 4558-4566.

40. Berndt, C.; Lillig, C. H.; Flohé, L., Redox regulation by glutathione needs enzymes. *Front. Pharmacol.* **2014,** *5*.

41. Kung, J. W.; Baumann, S.; von Bergen, M.; Müller, M.; Hagedoorn, P.-L.; Hagen, W. R.; Boll, M., Reversible Biological Birch Reduction at an Extremely Low Redox Potential. *J. Am. Chem. Soc.* **2010,** *132* (28), 9850-9856.

42. Martindale, B. C. M.; Joliat, E.; Bachmann, C.; Alberto, R.; Reisner, E., Clean Donor Oxidation Enhances the H_2 Evolution Activity of a Carbon Quantum Dot–Molecular Catalyst Photosystem. *Angew. Chem., Int. Ed.* **2016,** *55* (32), 9402-9406.

43. Bachmann, C.; Probst, B.; Guttentag, M.; Alberto, R., Ascorbate as an electron relay between an irreversible electron donor and Ru(II) or Re(I) photosensitizers. *Chem. Commun.* **2014,** *50* (51), 6737-6739.

44. Bachmeier, A.; Wang, V. C. C.; Woolerton, T. W.; Bell, S.; Fontecilla-Camps, J. C.; Can, M.; Ragsdale, S. W.; Chaudhary, Y. S.; Armstrong, F. A., How Light-Harvesting Semiconductors Can Alter the Bias of Reversible Electrocatalysts in Favor of H2 Production and CO2 Reduction. *J. Am. Chem. Soc.* **2013,** *135* (40), 15026-15032.

45. Hexter, S. V.; Esterle, T. F.; Armstrong, F. A., A unified model for surface electrocatalysis based on observations with enzymes. *Physical Chemistry Chemical Physics* **2014,** *16* (24), 11822-11833.

46. Milton, R. D.; Abdellaoui, S.; Khadka, N.; Dean, D. R.; Leech, D.; Seefeldt, L. C.; Minteer, S. D., Nitrogenase bioelectrocatalysis: heterogeneous ammonia and hydrogen production by MoFe protein. *Energy. Environ. Sci.* **2016,** *9* (8), 2550-2554.

47. Xiao, Y.; Chu, L.; Sanakis, Y.; Liu, P., Revisiting the IspH Catalytic System in the Deoxyxylulose Phosphate Pathway: Achieving High Activity. *J. Am. Chem. Soc.* **2009,** *131* (29), 9931-9933.

48. Peck, H. D.; Gest, H., A New Procedure for the Assay of Bacterial Hydrogenases. *J. Bacteriol.* **1956,** *71* (1), 70-80.

49. Wu, K.; Chen, Z.; Lv, H.; Zhu, H.; Hill, C. L.; Lian, T., Hole Removal Rate Limits Photodriven H_2 Generation Efficiency in CdS-Pt and CdSe/CdS-Pt Semiconductor Nanorod–Metal Tip Heterostructures. *J. Am. Chem. Soc.* **2014,** *136* (21), 7708-7716.

Chapter 4

Semiconductor Nanocrystals as Tools to Probe Enzyme Structure and Dynamics

Abstract: Efficient photochemical systems for hydrogen production have been widely studied to elucidate the factors controlling the stability and efficiency of photochemical hydrogen evolution. We exploit the photochemical system described in Chapter 3 to generate a highly versatile platform for mechanistic studies of H_2ase enzymes. We show that photoexcitation of this system with a short laser pulse can initiate sub-TOF catalytic dynamics in SHI which can be interrogated via time-resolved infrared and optical spectroscopies. We further show that using external excitation to photochemically activate aerobically inactivated samples of SHI and probing via tandem FTIR and UV-Vis spectroscopy we could completely resolve the activation process and provide strong evidence in support of a recent literature model.

4.1 - Introduction

Oxidoreductases represent some of nature's most efficient enzymes for performing critical energy conserving reactions such as proton reduction with faster rates and lower overpotential than most synthetic catalysts[1]. Their rapid turnover can present a significant challenge because it requires experimental methods with sufficient time resolution to observe dynamics occurring faster than the turnover rate. For example, rapid mixing studies of hydrogenase[2-3] have verified that the known steady states of the enzyme react with or are produced by reaction with H_2, but they have lacked the resolution to temporally separate these dynamics from the mixing time. The greatest promise lies with optical methods, where the fastest inherent time resolution is, in principle, available. While there has been progress in this area,[4-6] it remains a challenge to obtain convenient optical triggers of enzyme reactivity.

A recently emerging paradigm in this field has been the use of exogenous chromophores rationally appended to the protein framework. These complexes can then engage in a photochemical transformation such as electron or hole transfer at the protein surface and initiate reactivity with a short laser pulse[7-8]. Photo-uncaging of reducing species with a pump laser pulse has also shown promise as a means of triggering enzyme reactivity and protein folding.[5, 9]

There is also much interest in being able to resolve the response to the reduction potential since oxidoreductases often contain many redox active cofactors critical for their function. Protein film voltammetry provides a way to observe catalytic current generated by redox enzymes[10] and a convenient way to probe their response to perturbing environmental conditions such as oxygen oxposure.[11-12] Despite the advantages of this method, in particular its exquisite control over the reduction potential experienced by the enzyme, it has the significant drawback of being spectroscopically blind to the state of the enzyme active site and chemical and structural changes occurring there.

In this chapter, the photochemical system presented and characterized in Chapter 3 is applied to the study of the structure and function of the SHI protein itself. We demonstrate that, aside from its exceptional photochemical performance, this system has utility in photo triggering enzyme reactivity for studies of the catalytic mechanism. We also show that we can leverage this system to gain insight into the nature of reaction of oxygen with the SHI enzyme as well as its reductive reactivation.

4.2 - Results and Discussion

4.2.1 – CdSe/CdS nanorod photo-sensitization of sub-TOF H_2ase dynamics

A first effort has been directed at extending the potential jump methodology[5] to the new, highly efficient, photochemical system with CdSe/CdS dot-in-rod (DIR) photosensitizers and a low potential redox mediator (PDQ^{2+}, E^0= -550 mV vs. NHE) which was detailed in Chapter 3 of this thesis. Before any study on the full nanoparticle sensitized photochemical system was initiated, we first set out to examine the viability of the PDQ^{2+} mediator to drive turnover under the original NADH photolysis based scheme[5]. Figure 4.1 shows the results of comparison of NADH photolysis with either 5 mM MV^{2+} or 5mM PDQ^{2+} as the redox mediator to drive hydrogen evolution under 355 nm excitation from a tripled Nd:YAG laser. The superior performance of PDQ^{2+} in terms of amount of hydrogen evolved is clear, implying it is more efficient in delivering electrons to the SHI catalyst. UV-vis spectra pre- and post-photolysis reveal that all the NADH, identified by its absorption band centered at 340 nm, has been consumed in both cases. The large amount of $MV^{+\bullet}$ radical that remains at the end of the MV based photolysis experiment shows that a large amount of $MV^{+\bullet}$ radical is required to build up to start driving the H_2 production process. In contrast, $PDQ^{+\bullet}$ can drive catalysis directly without the requirement for a large amount of radical to build up due to its lower reduction potential.

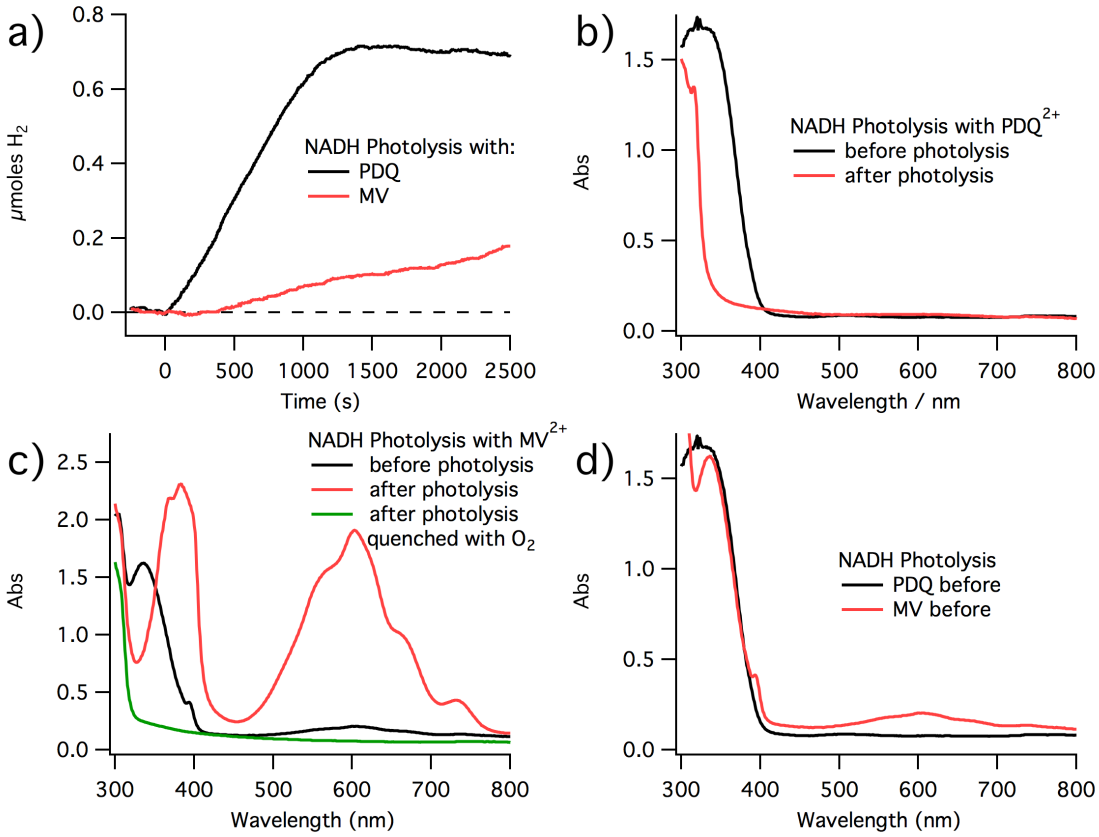

Figure 4.1 Comparison of different mediators for photocatalysis. a) Time dependent hydrogen production from NADH photolysis with 50 nM SHI and 10 mM phosphate buffer pH = 7 with either 5 mM MV^{2+} or 5 mM PDQ^{2+} in solution monitored by pressure changes in the headspace. b) UV-Vis spectra before and after photolysis in the PDQ^{2+} containing sample. c) UV-Vis spectra before and after photolysis in the MV^{2+} containing sample as well as a spectrum taken after exposure of the "after" sample to atmosphere to quench the $MV^{+\bullet}$ radicals. d) Overlays of the "before" photolysis spectra for both PDQ^{2+} and MV^{2+} containing samples.

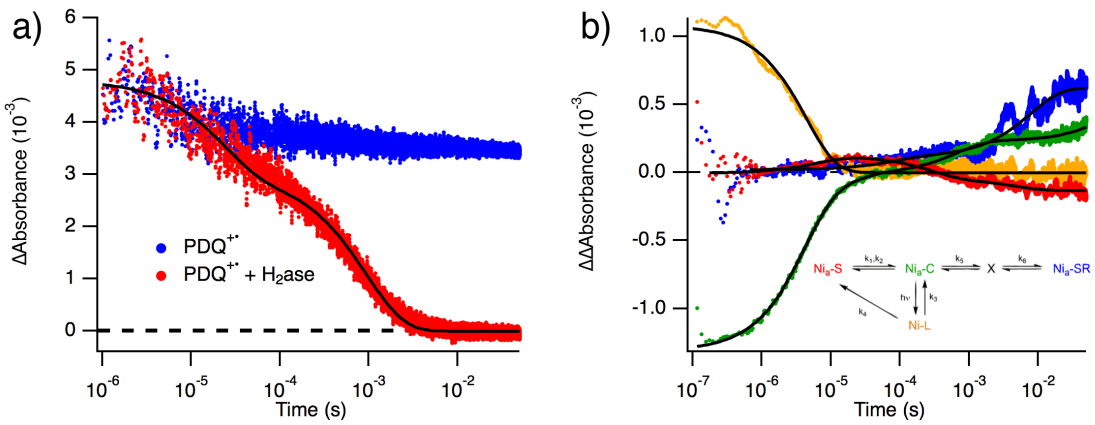

Figure 4.2 –Potential jump experiments. a) Time resolved visible signal at 808 nm showing the dynamics of the $PDQ^{+\bullet}$ radical in the presence (red) or absence (blue) of SHI. b) IR transients of SHI active site initiated by photoexcitation of CdSe/CdS nanorods and subsequent reduction of PDQ^{2+} to $PDQ^{+\bullet}$ showing sub-TOF dynamics of the SHI active site. Conditions: 500 μM SHI, 10 mM PDQ^{2+}, 50 mM sodium phosphate: pH = 7.2, 50 mM mercaptopropionic acid.

Preliminary time resolved infrared and visible experiments have demonstrated that we can generate larger potential jumps and leverage this system to observe sub-TOF dynamics in *Pf* SHI. Figure 4.2a shows the transient visible signal at 808 nm following photoexcitation of the DIR which is sensitive to $PDQ^{+\bullet}$. The effect of the lower redox potential of the mediator is immediately apparent in that complete consumption of the photo-generated radical is observed within the course of the experimental time window as opposed to the case with MV^{2+} where a stable population of reduced radical persists beyond 100's of milliseconds indicating the establishment of a new equilibrium[5] (See Figure 2b in reference 5) consistent with the observations in the NADH photolysis experiments. Faster ET dynamics are also observed, consistent with the greater driving

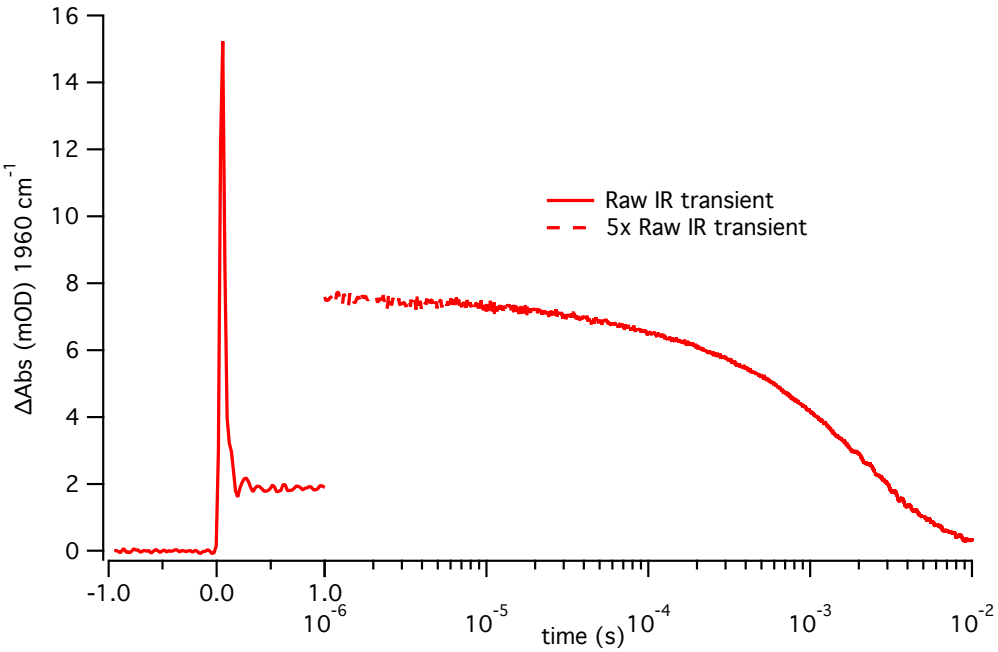

Figure 4.3 – Intraband absorption and heating signal Raw infrared transient of a sample containing CdSe/CdS nanorods and 10 mM PDQ^{2+} showing the instrument limited response of the infrared signal at early time corresponding to the intraband absorption

force for electron transfer. Transient IR spectroscopy, shown in Figure 4.2b, exhibits active site dynamics with features consistent with the previously published NADH photolysis experiments. These results further validate that the dynamics observed through NADH photolysis were limited by dynamics at the active site and not by ET from the redox mediator.[5] Some qualitative differences are observed in the distribution of states at late times which will be the subject of future investigation and are likely due to the more substantial potential jump enabled by the more negative reduction potential of the PDQ^{2+} mediator.

Previous attempts to perform TRIR in the CdTe based system[13] were unsuccessful for a variety of reasons. The QY of the system was relatively low, necessitating high

optical densities to achieve reasonable yields of productive electron transfer. Additionally, excited electrons in semiconductor nanostructures have strong intraband absorption[14-15] in the infrared that can cause large artifacts at early time in the transients. These can obscure the comparatively smaller signals arising from the H_2ase active site. Using redox mediators circumvents these shortcomings in several ways. Transfer of excited electrons from the nanoparticle to the redox mediator can occur on ultrafast timescales. This largely suppresses the contribution of the intraband absorption signal to the infrared transients, improving the quality of the signal. This intraband absorption signal is shown in Figure 4.3 in the raw infrared transient following excitation at 355 nm of a control sample not containing any hydrogenase. It manifests as the instrument limited spike at the beginning of the transient which is followed by the decay of the heating signal on a longer timescale. Additionally, photoreduction of small molecule mediators can be highly efficient[16] and can even achieve multiple reduction events per particle[17] within a single laser pulse.

We have shown that high QYs of hydrogen generation can be achieved in optimized systems (Chapter 3) using this photochemical system. We have leveraged this system to show that sub-TOF hydrogenase dynamics can be initiated by photoexcitation of DIR nanostructures. The inclusion of a sacrificial electron donor to regenerate the ground state of the sensitizer allows for regeneration of the original state of the sample by escape of photo-generated hydrogen from the sample cell, prolonging sample life and increasing the versatility of the technique.

4.2.2 – Insights into *Pf* SHI oxygen tolerance and spectroscopic characterization of photochemical reactivation

Many metalloenzymes that catalyze reactions of great importance such as H_2, CO_2 and nitrogen reduction show a strong sensitivity to inhibition and destruction by small molecules, particularly oxygen.[18-21] Hydrogenases exhibit a range of tolerances to oxygen ranging from irreversible inactivation in the [FeFe] H_2ases[22] to varying degrees tolerance in the [NiFe] H_2ases.[11, 23-24] The [NiFe] H_2ases are generally divided into two categories of oxygen tolerance depending on their response to oxygen exposure. The so called "standard" [NiFe] H_2ases are characterized by formation of two distinct inactive states Ni-A and Ni-B upon oxygen exposure. These states are denoted "ready" and "unready", respectively, referring to their reactivation kinetics; under reducing conditions Ni-B is reactivated within seconds while Ni-A is reactivated on a much longer timescale[23]. The second group of hydrogenases is referred to as "oxygen tolerant" and is characterized by forming only the Ni-B state upon inactivation by oxygen and requiring less reducing conditions for reactivation[25]. A recent discovery is a new, more complex, class of oxygen tolerance exhibited by SHI from *Pyrococcus furiosus*[11] which is the subject of the current study. Like the oxygen tolerant enzymes SHI can sustain some hydrogen oxidation activity under an aerobic atmosphere, especially at high temperatures. Unlike the oxygen tolerant class of enzymes, however, SHI was observed to form at least 3 distinct inactive states and it does not possess the unique high potential [4Fe3S] cluster that is thought to be critical to the function of the oxygen tolerant enzymes.[26]

The mechanism that imparts SHI with its unique resistance to oxygen is still unclear. Reports in the literature have suggested that reversible oxygenation of active site

cysteine residues may play a role[27] and although the involvement of multiple inactive states has been implicated[11] no unified picture has emerged to date. Elucidating the nature of the unique resistance of SHI to damage by oxygen represents a challenging problem in enzymology which can benefit from the development of novel experimental approaches.

To gain insight into this complex problem a new technique for spectroscopic observation of changes at the SHI active site during reductive photochemical activation was developed. The electrochemical potential in the system could be externally raised by diffusion of oxygen into the sample cell over an extended period, typically days. This facilitated the formation of the putative inactive states implicated in the oxygen tolerance mechanism. The reduction potential in the sample could them be systematically lowered by "titration" of light into the system initiating photochemical reduction of a soluble

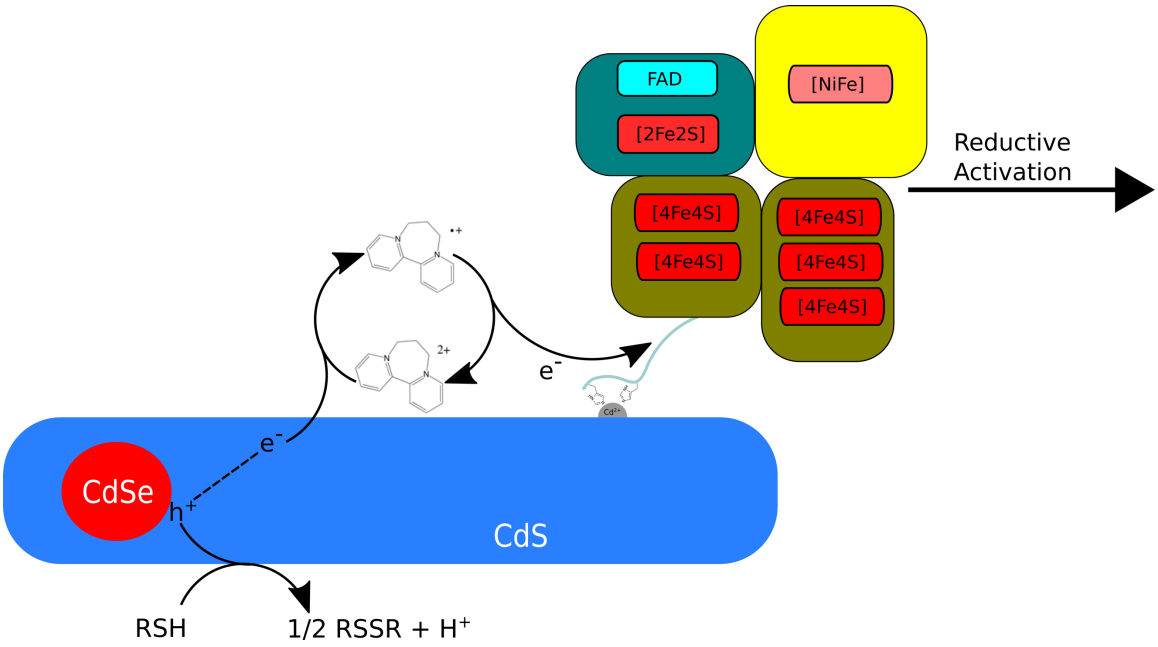

Scheme 4.1 –Photochemical reactivation of SHI from its aerobically inactivated states. Photoreduction of a PDQ^{2+} redox couple by CdSe/CdS DIR structures allows for reduction of the FeS clusters in the SHI enzyme. RSH represents the thiol sacrificial electron donor.

redox mediator. The basis for this technique is the photochemical system described in Chapter 3.

The essence of this method is the transport of electrons between redox couples. The critical insight is that the equilibration of electrochemical redox couples are restricted by their reaction kinetics. Electrons held in radical cations, for example, can engage in rapid electron transfer with the relevant FeS cluster redox integral to many oxidoreductases. An outline of the system utilized for the photochemical reactivation is presented in Scheme 4.1. The $PDQ^{2+}/PDQ^{+\bullet}$ redox couple (1) employed herein quantitatively transfers electrons to the FeS clusters of SHI within milliseconds (see for example Figure 4.2a) A thiol-disulfide redox couple (2) is utilized as a sacrificial electron donor system. These thiol redox couples generally exhibit sluggish kinetics in solution owing to the need to orchestrate multiple proton and electron transfers to facilitate redox reactions, which can be accomplished enzymatically or, as in this case, catalyzed by the nanoparticle cadmium chalcogenide surface.[28-29] This surface catalyzed process has the further advantage of sequestering the reactive thyil radical intermediates by confining them to the nanoparticle surface until they can couple to form the disulfides. This is ideal for a system to undertake mechanistic studies as it inhibits degradation of the enzyme by these reactive intermediates, ensuring that experimental observations correspond to the redox processes of interest and not to uncontrolled side reactions[30]. Unlike protein film voltammetry, the soluble redox couple ensures that all enzymes have equal probability of accepting reducing equivalents whereas in the former approach, some population of enzyme with weak electronic coupling to the electrode could be mistaken for a slowly reactivating state.

(1) $PDQ^{2+} + e^{-} \rightleftharpoons PDQ^{+\bullet}$

(2) $2\,RSH \rightleftharpoons RSSR + 2\,e^{-} + 2\,H^{+}$

Samples for photochemical reactivation were prepared in copper infrared cells with a 50 micron spacer and CaF_2 windows. These samples consisted of 0.7-1.5 mM SHI, ~1 μM CdSe/CdS DIR, 10 mM PDQ^{2+}, 100 μM phenosafranine ,50 mM mercaptopropionic acid in 10 mM phosphate buffer at pH = 7.2 prepared in an anaerobic chamber containing ~2-4% hydrogen gas. Samples prepared by this method are in a distribution of catalytically active states as observed by FITR, consistent with previous similarly prepared samples.[5] These samples, contained in standard copper infrared cells, could be aerobically inactivated by incubation in the dark at ambient conditions for several days. During this time oxygen diffused into the sample cell and reacted with SHI generating a mixture of the putative inactive states. The nature of the method used for generation of SHI inactive states necessarily introduces inhomogeneity in the sample due to the diffusive nature of oxygen transport in the sample cell. The diffusive nature of the oxygen mediated inactivation was confirmed by position dependent FTIR prior to any photo reactivation of the sample shown in Figure 4.4. The position dependence was probed by changing the location where the infrared beam was focused on the sample. Sample located closer to the outer rim of the CaF_2 window was the most oxygen exposed which manifested as a decline in the Ni-S and Ni-C peak (1951 cm^{-1} and 1967 cm^{-1} respectively) amplitudes relative to the amplitudes of inactive states at 1960 cm^{-1} and 1964 cm^{-1} towards the edge of the sample cell. Sample located closer to the center of the CaF_2 window experienced the least oxygen exposure.

To avoid the issue of sample heterogeneity light titrations were carried out by probing a single spatial point, generally in the middle of the sample cell. Excitation of the sample was carried out with a 450 nm diode laser as described in Chapter 2.4.2. FTIR spectra were baseline corrected and fit in a global model accounting for the known catalytically active states, (Ni-S, Ni-C, Ni-SR, Ni-SR', Ni-SR'') as well as 3 more states which formed upon oxidative inactivation and were observed to recover upon reductive reactivation. These were located at 1947.5 cm^{-1}, 1959.8 cm^{-1} and 1963.2 cm^{-1} and we will

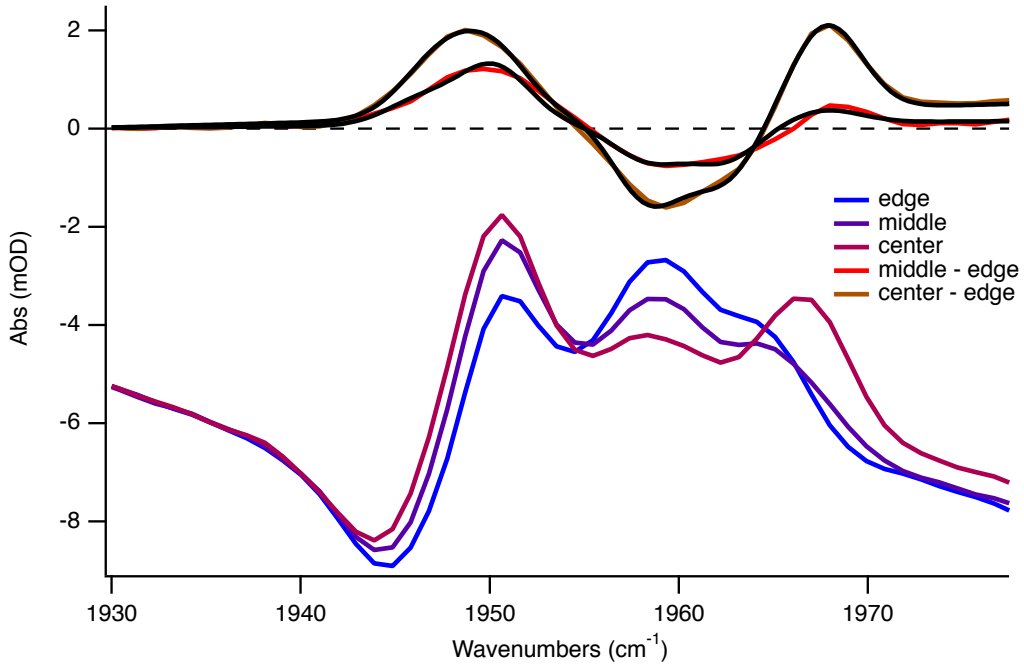

Figure 4.4 - Raw FTIR spectra (bottom, no baseline subtraction) of aerobically inactivated NR-SHI-PDQ^{2+} sample at 3 different spatial positions and difference spectra (top) showing the changes in the distribution of states at those locations. Solid black lines are fits to gaussians using the peak positions from global fits.

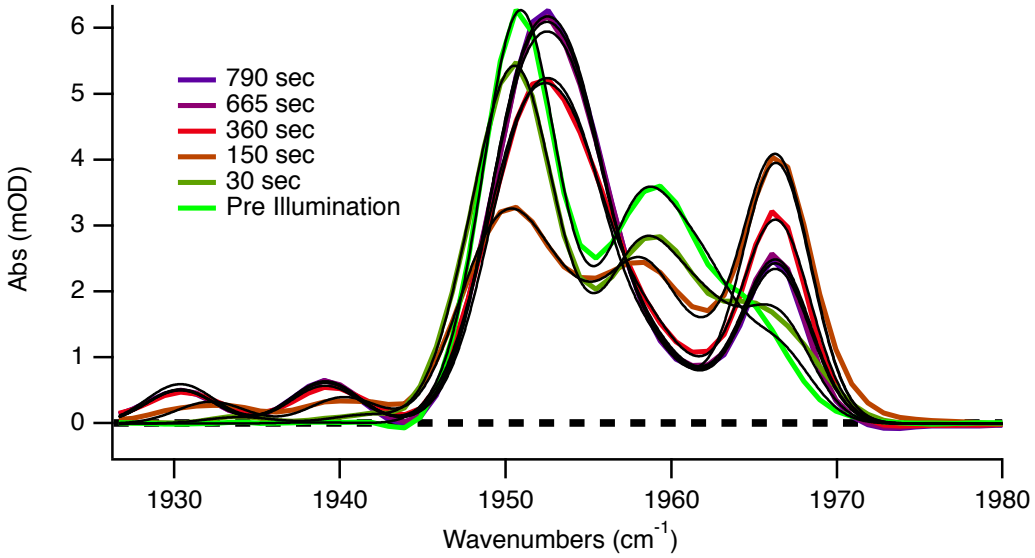

Figure 4.5 – Baseline corrected FTIR spectra for photochemical reactivation of oxygen exposed SHI. Global fits to the data using an 8-component (Gaussian) model are shown in black. Only selected spectra are shown for clarity.

refer to these states by the convention Ni-Inact$_1$, Ni-Inact$_2$ and Ni-Inact$_3$ (or simply as Inact$_n$)

Baseline corrected FTIR spectra following the progression of the light titration are shown in Figure 4.5 along with selected fits (for clarity) from the globally fit model. It is clear from the data that illumination of the sample shifts the equilibrium a more reduced environment. Notably the resonance due to Ni-S, the most oxidized state in the catalytic cycle, diminishes at early time with illumination followed by formation of Ni-C at intermediate time and at late time the sample becomes dominated by Ni-SR. However, overlap of the infrared resonances of the manifold states complicates visual inspection and interpretation of the data in this form.

To facilitate visual inspection, the data was also visualized and fit in the global model as difference spectra without the need for any baseline subtraction. The interconversion

of the states of SHI was also represented by extracting the amplitudes of the Gaussian components from the global model. This is valid since all the Gaussian components were constrained to a share a single width parameter, guaranteeing that the integrated area of the peaks is proportional to the amplitude and that they each represent a single CO resonance. The results of this analysis are shown in Figure 4.6 where the spectral evolution is broken down into the evolution of the amplitude of the individual states of SHI as a function of illumination time. The evolution of the main catalytically active states of SHI are shown in Figure 4.6B. The panel 4.6D shows Ni-SR evolution along with its protonation isomers Ni-SR' and Ni-SR'' for the sake of completeness although their behavior generally tracks that of Ni-SR on the timescale of this experiment.

The first notable process is a beaching Ni-S with a corresponding induced absorbance of Ni-C. These are connected by the proton coupled electron transfer (PCET) reaction (3).

(3) $\text{Ni-S} + e^- + H^+ \rightleftharpoons \text{Ni-C}$

This process is followed by conversion of Ni-C to Ni-SR via (4) at later time (100's of seconds).

(4) $\text{Ni-C} + e^- + H^+ \rightleftharpoons \text{Ni-SR}$

These reactions are represented in Scheme 4.2 along with structures depicting the chemical changes at the active site during the catalytic cycle. The double headed arrow to the right closes the cycle, indicating the binding or release of H_2.

Along with the interconversions between the catalytically active states, changes in infrared bands not associated with the catalytic cycle are also evident. These are likely associated with inactive states of the enzyme and further analysis of the data suggests that

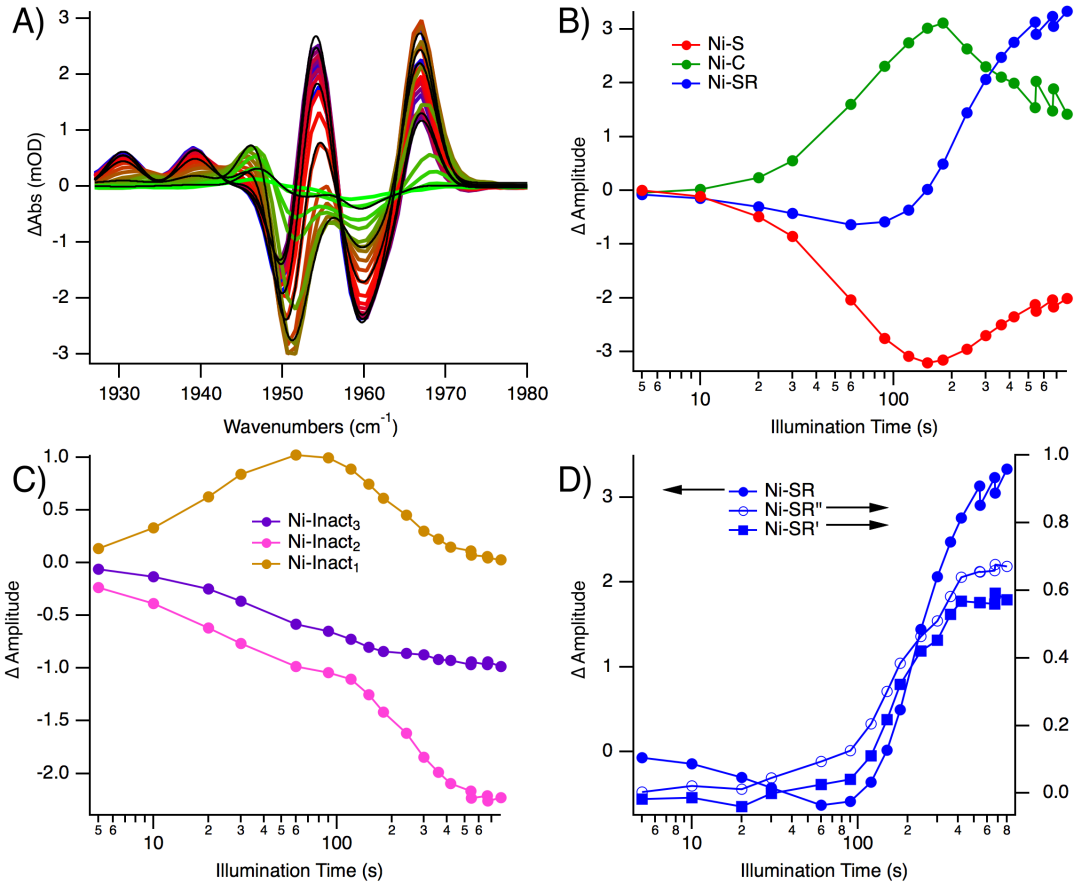

Figure 4.6 – Photochemical reactivation of SHI through light titration A) FTIR difference spectra of reductive photo-activation of SHI along with the fits from the global model. Changes in amplitude of: A) the primary states in the catalytic cycle of SHI, B) the putative inactive states formed by reaction of SHI with oxygen and C) The putative forms of the Ni-SR state, upon illumination of the aerobically inactivated sample

they likely correspond to the three inactive states observed by Jones and co-workers using protein film voltammetry[11] also labeled $Inact_{1\text{-}3}$ for consistency.

In the position-dependent FTIR in Figure 4.4 we see evidence of the different redox levels of the inactive states. In the center of the sample we see larger populations of the Ni-S and Ni-C catalytically active states. Along with these states, a larger population of $Inact_1$ is also present under these conditions. Towards the outer rim of the sample, under more oxidizing conditions, we observe loss of amplitude of both Ni-C and $Inact_1$. In the difference spectrum of "middle – edge" the positive band on the low energy side clearly blue shifts with respect to the "center – edge" indicating a larger contribution from Ni-S in this spectrum and a lesser contribution from $Inact_1$. These results strongly suggest that $Inact_1$ shares a redox level with Ni-C corresponding to the putative state also labeled $Inact_{1\text{-}3}$ by Jones and co-workers.[11] The light titration data are also consistent with

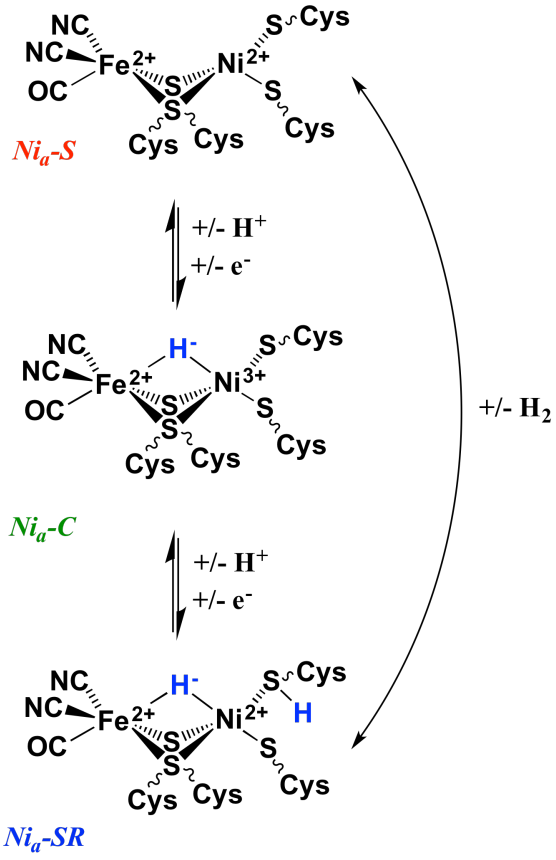

Scheme 4.2 – Elementary catalytic cycle of hydrogen production and oxidation in [NiFe] Hydrogenases.

this interpretation. Upon illumination of the oxygen inactivated sample we see the amplitude of the $Inact_1$ state increase. This increase also tracks the increase of the Ni-C state albeit with a slightly different rate while Ni-S is strongly bleaching during this time. This further supports the notion that $Inact_1$ and Ni-C share a similar redox level and the slight difference in their formation rate may reflect the effect of the oxygen concentration in the sample since, as $PDQ^{+\bullet}$ is generated, it will react with and reduce dissolved oxygen, eventually scrubbing it from the system.[31] Interestingly this brings up the issue of externally generated reactive oxygen species (ROS) in the inactivation of hydrogenase (in other words ROS not generated at the active site of the protein) such as may be generated by reaction with $PDQ^{+\bullet}$. It should be noted that such pathways may have biological relevance since reactivity of FeS clusters with molecular oxygen is known[32-33] and can generate a similar spectrum of ROS. Addressing whether these ROS species may play a role in generating these inactive states is beyond the scope of this work however and may be addressed in future work.

Further illumination leads to the bleaching of the $Inact_1$ state with a similar time profile to bleaching of Ni-C. This coincides with the growing in of the Ni-SR state and is consistent with rapid reactivation of $Inact_1$ under more reducing conditions.

The state $Inact_2$ begins the light titration by bleaching out amplitude at early illumination time points. The time dependence of the decrease in $Inact_2$ amplitude almost mirrors the increase in $Inact_1$ during the first 100 seconds. This further supports the model of Jones and co-workers where $Inact_1$ and $Inact_2$ are separated by PCET via (5)

(5) $Inact_2 + H^+ + e^- \rightleftharpoons Inact_1$

Further into the light titration, near the transition point where Ni-SR begins to grow in and $Inact_1$ starts to be bleach out, the depletion of $Inact_2$ begins to become more pronounced. A larger amplitude of $Inact_2$ ultimately bleaches out than is formed from $Inact_1$ consistent with the significant amount of $Inact_2$ present at the start of the experiment. Interestingly, conversion to $Inact_1$ is no longer a viable sink for the bleaching $Inact_2$ since it too begins significantly depleting beyond this point. Likely, the solution reduction potential becomes negative enough to rapidly reactivate $Inact_1$ and deplete the $Inact_1$ resulting from acceleration of process (5), increasing the pool of active enzyme. Also, the depletion of $Inact_1$ drives the depletion of $Inact_2$ through the principle of LeChatlier. Interestingly, in the NAD^+ reducing hydrogenase of *Ralstonia eutropha,* which bears some similarities to the *Pf* SHI enzyme, formation of a "Ni_r-B-like" state was observed upon oxygen exposure of whole cells[34] which could be readily reductively activated under H_2 incubation. It is likely that this state resembles $Inact_2$ given the instability of the Ni-C associated redox level in this enzyme.

The remaining inactive state, $Inact_3$, appears to sluggishly deplete through the course of the experiment. Unlike any of the other states, it does not experience a significant transition in its behavior near 100 s in the light titration. This suggests that the reactivation of $Inact_3$ is not under equilibrium control but rather is kinetically controlled. We assign this state the most oxidized inactive state observed by Jones and coworkers. Since the reduction potential of this state is more positive than the other two inactive states observed, the solution potential through the course of the titration was more than reducing enough to reactivate $Inact_3$, further supporting the hypothesis that reactivation of this state was kinetically limited. The model presented by Jones and co-workers[11], shown

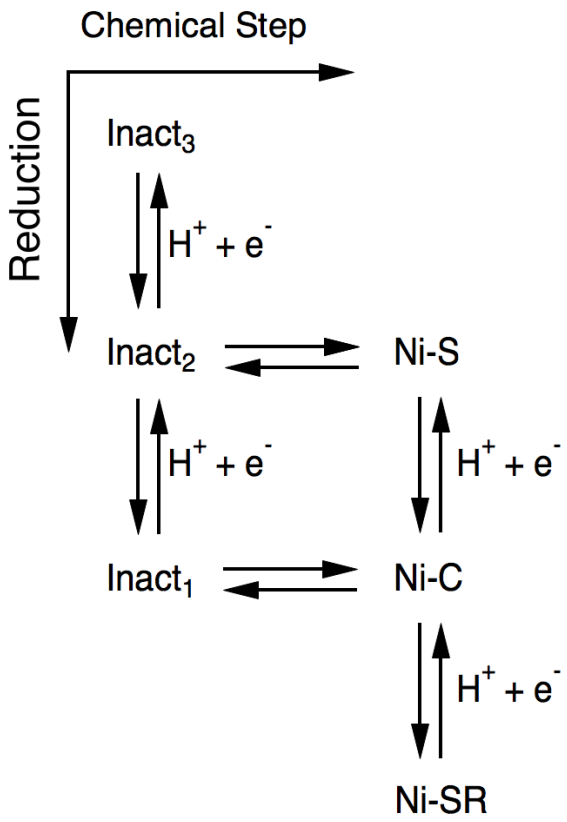

Figure 4.7 – Model of the inactive states of SHI and their interconversion with the catalytically active states of the SHI. Adapted from Jones and co-workers, reference 11.

in Figure 4.7, is largely consistent with our observations. In our experiments $Inact_1$ and $Inact_2$ are reactivated under equilibrium control on the timescale of the measurements (tens of minutes per spectrum) with both states rapidly reactivating once the environment is reducing enough to begin forming significant amounts of Ni-SR. It is unclear, however, why there exists such a high kinetic barrier to the $Inact_3$ to $Inact_2$ conversion. One possibility is a substantial chemical modification to the active site occurs such as sulfoxygenation of active site cysteine residues[27] or that this transition requires some large-scale protein motion that is rate limiting.

The nature of the light titration experiment allows for the use of complementary optical probes in addition to performing FTIR spectroscopy. UV-Vis absorption

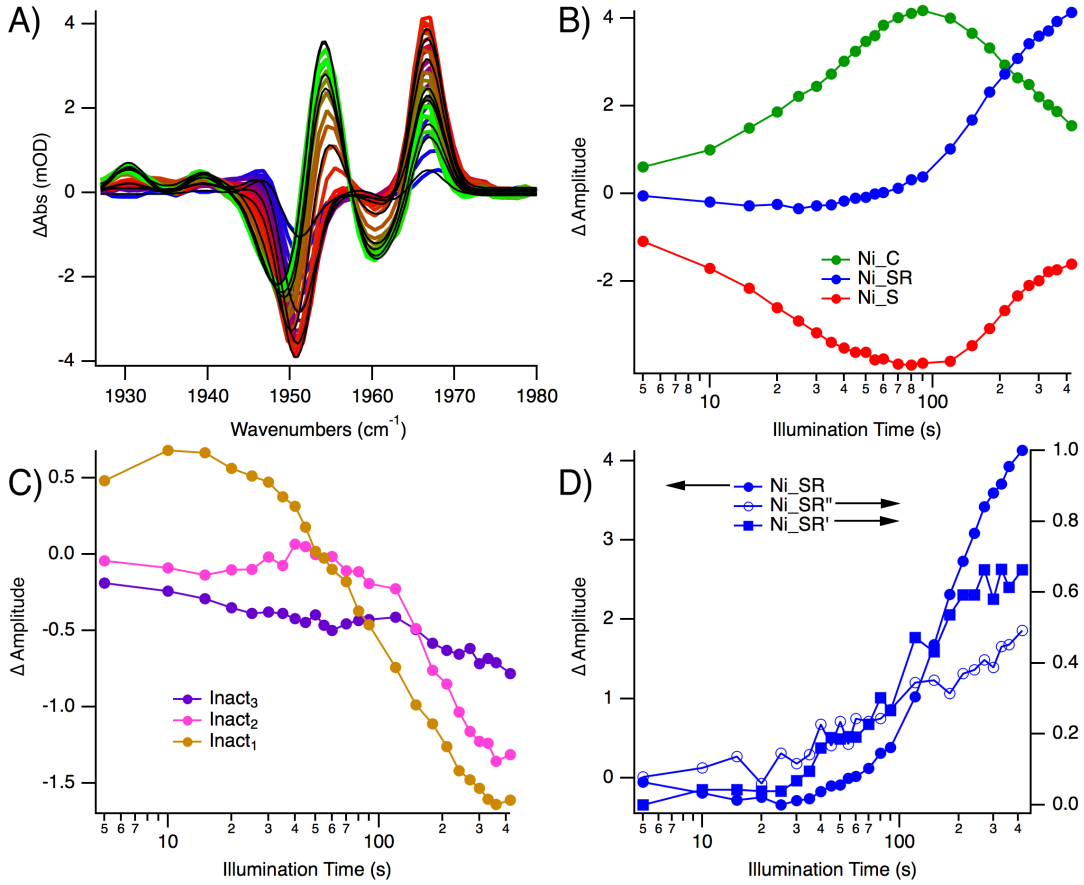

Figure 4.8 – Light titration with tandem UV-Vis Data for an FTIR light titration conducted in conjunction with collection of optical spectra through a fiber coupled UV-Vis spectrometer. Data are presented in the same format as Figure 4.6. Note: this sample was prepared without phenosafranine

spectroscopy can report sensitively on the changes in the oxidation state of FeS clusters in proteins[35] and difference measurements are ideally suited to detect small, subtle changes in absorption spectra. We anticipated this method could provide complementary information on the redox environment of SHI during the light titration experiment.

Figure 4.8 presents a light titration performed on an aerobically inactivated sample of SHI similar to the experiment previously discussed (Figure 4.6). Some minor qualitative differences between the two experiments, particularly in the behavior of the inactive states, likely arising from different initial conditions at the onset of the experiment such as the presence of a significant amount of $Inact_1$ prior to the start of the

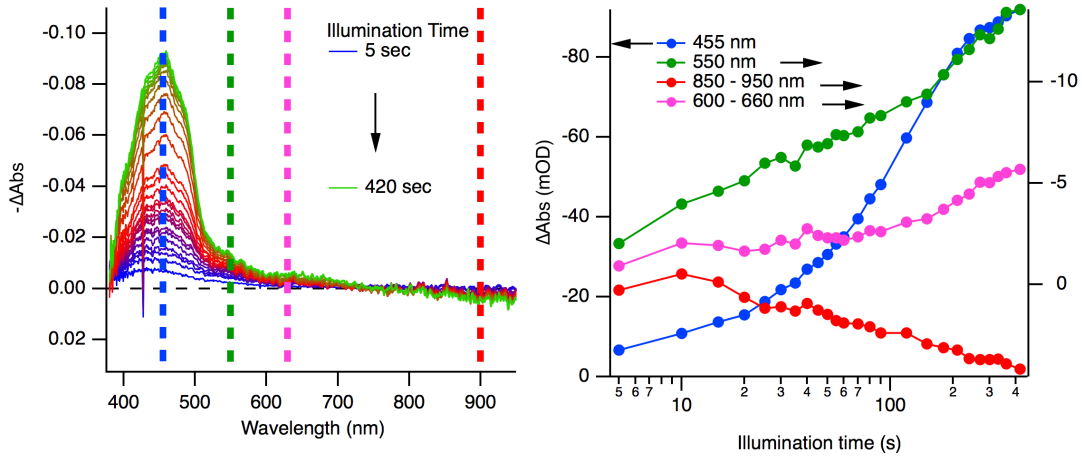

Figure 4.9 – Difference UV-Vis measurements during light titration (left side) collected during the light titration experiment in Figure 4.8 as a function of illumination time. Vertical dotted lines denote probe wavelengths and color coding of the time dependent changes in plotted on the right-side graph. The y axis in both graphs is inverted for clarity.

light titration in the latter experiment. Those differences will not be discussed further here. UV-Vis difference spectra were collected at the same sample spot as the FTIR data and are shown in Figure 4.9. The observed signal is dominated by bleaching centered at 455 nm. This signal corresponds to reduction of the SHI FeS clusters by $PDQ^{+\bullet}$ as the light titration progresses via loss of $S^{2-} \rightarrow Fe^{3+}$ charge transfer transitions.

In the first set of light titration data presented (Figure 4.6), rapid reactivation of $Inact_1$ and $Inact_2$ was gated by a shift in solution potential to more reducing potentials.

This was inferred from a shift in the active enzyme population to Ni-SR, Ni-SR' and Ni-SR'' from Ni-C. The optical probe provides an independent means of quantifying changes in the sample redox level. The larger the magnitude of the bleaching signal, the more reducing the environment in the sample. The signal at 455 nm continuously bleaches during the whole light titration, and the trace can be fit to an exponential decay with t = 131 ± 5 seconds. This lined up reasonably well with Ni-SR becoming a significantly populated state as well as the onset of rapid $Inact_1$ and $Inact_2$ reactivation, although the use of an exponential fit should not be given kinetic meaning, only as a means to quantify an average transition time. Interestingly, the difference spectra clearly resolve more than one spectral component. This is clearly seen in the changing shape of the spectrum near 455 nm and in the distinct temporal behavior of time slices at different wavelengths. There is likely contribution from the reduction of the oxidized form of the FAD cofactor.[36] Separating the spectral components into the evolution of the different species will likely require a more detailed analysis, likely singular value decomposition and comparison of spectra changes in the native with those in the SHI dimer in which the subunits containing the FAD cofactor are excluded. Those studies are ongoing.

4.3 - Conclusion

In summary, we have demonstrated the utility of this photochemical system for characterizing reduction potential dependent properties of H_2ase enzymes through light titrations probed by FTIR and UV-Vis spectroscopy. We have also demonstrated this photochemical system can initiate rapid potential jumps which can be probed by TRIR and visible transient absorbance. Photoexcitation of the CdSe/CdS nanocrystals provide a

means to initiate a reduction potential jump within microseconds enabling mechanistic studies over many orders of magnitude in time using a robust sensitization scheme which we have observed to be stable for over several months without noticeable degradation, even with repeated extended exposure to ambient conditions and repeated performance of many experiments on the same sample (>6 light titrations and >4 TRIR experimental sessions on a single sample typically). This chapter represents only an initial investigation into the potential applications of this methodology to understanding of SHI. The extension of this technique to other hydrogenases and other enzyme systems can greatly increase its utility.

Furthermore, this assignment of previously postulated[11] inactive states to specific infrared resonances and their mechanistic relationship to each other provides valuable guidance to theoreticians in elucidating the structures of these inactivated states.[37] Given the mechanistic distinctions between oxygen tolerance behavior in SHI and in the "standard" hydrogenases some caution is warranted in speculating about the structure of the inactive states of SHI and reasoning through analogy. That being said, some observations are warranted.

The observed rapidly reactivating inactive states of SHI all have lower reduction potentials than the prototypical Ni-A and Ni-B states in standard hydrogenases. Ni-A and Ni-B are generally at more positive potentials than Ni-S. In addition, the Ni-B states are typically considered to not be distinguishable from Ni-A through IR spectroscopy and their structures remain controversial.[38] It was claimed by Jones and coworkers that the states $Inact_1$ shares a redox level with the Ni-C state while $Inact_2$ is on par with Ni-S. Which is consistent with our observations. However, we note that the peak of $Inact_1$

population occurs at slightly higher reduction potential (shorter illumination time) than the peaking in the Ni-C population (Figure 4.6B-C). This suggests that $Inact_1$ has a slightly higher reduction potential than Ni-C although it is quite close.

Additionally, it has been suggested that formation of the inactive states is not due to reactivity of molecular oxygen with the active site of H_2ase but rather simply its properties as an electron acceptor with a very positive reduction potential.[39] Even so it has been suggested that an active site cysteine likely has oxidative modifications to a sulfenate in the Ni-A state.[38] This is consistent with the slow reactivation kinetics of $Inact_3$, which suggests that this state has undergone active site sulfoxygenation. This leaves the structures of the $Inact_{1-2}$ states unresolved although, given their rapid reactivation kinetics, it is tempting to speculate that these states are analogous to those found in other oxygen tolerant H_2ases which would render $Inact_2$ a "Ni-B like" state and $Inact_1$ and EPR silent divalent nickel state analogous to Ni-SI_r[40] although it raises the question what may cause the dramatic negative shift in the reduction potentials of these putative species. This method provides a clear path forward for probing these questions through the use of light to control the distribution of active and inactive states and the solution reduction potential. Future experiments coupling this technique to EPR and Raman spectroscopy as well as isotopic enrichment with deuterium and O^{18} sources will allow the definitive assignment of these states and elucidation of their structure.

4.4 - References

1. Helm, M. L.; Stewart, M. P.; Bullock, R. M.; DuBois, M. R.; DuBois, D. L., A Synthetic Nickel Electrocatalyst with a Turnover Frequency Above 100,000 s−1 for H_2 Production. *Science* **2011,** *333* (6044), 863-866.

2. Happe, R. P.; Roseboom, W.; Albracht, S. P. J., Pre-steady-state kinetics of the reactions of [NiFe]-hydrogenase from Chromatium vinosum with H2 and CO. *European Journal of Biochemistry* **1999,** *259* (3), 602-608.

3. George, S. J.; Kurkin, S.; Thorneley, R. N. F.; Albracht, S. P. J., Reactions of H2, CO, and O_2 with Active [NiFe]-Hydrogenase from Allochromatium vinosum. A Stopped-Flow Infrared Study. *Biochemistry* **2004,** *43* (21), 6808-6819.

4. Callender, R.; Dyer, R. B., Advances in Time-Resolved Approaches To Characterize the Dynamical Nature of Enzymatic Catalysis. *Chem. Rev.* **2006,** *106* (8), 3031-3042.

5. Greene, B. L.; Wu, C.-H.; McTernan, P. M.; Adams, M. W. W.; Dyer, R. B., Proton-Coupled Electron Transfer Dynamics in the Catalytic Mechanism of a [NiFe]-Hydrogenase. *J. Am. Chem. Soc.* **2015,** *137* (13), 4558-4566.

6. Lubner, C. E.; Jennings, D. P.; Mulder, D. W.; Schut, G. J.; Zadvornyy, O. A.; Hoben, J. P.; Tokmina-Lukaszewska, M.; Berry, L.; Nguyen, D. M.; Lipscomb, G. L.; Bothner, B.; Jones, A. K.; Miller, A.-F.; King, P. W.; Adams, M. W. W.; Peters, J. W., Mechanistic insights into energy conservation by flavin-based electron bifurcation. *Nat. Chem. Biol.* **2017,** *13* (6), 655-659.

7. Olshansky, L.; Greene, B. L.; Finkbeiner, C.; Stubbe, J.; Nocera, D. G., Photochemical Generation of a Tryptophan Radical within the Subunit Interface of Ribonucleotide Reductase. *Biochemistry* **2016,** *55* (23), 3234-3240.

8. Nocera, D. G.; Winkler, J. R.; Yocom, K. M.; Bordignon, E.; Gray, H. B., Kinetics of intermolecular and intramolecular electron transfer from ruthenium(II) complexes to ferricytochrome c. *J. Am. Chem. Soc.* **1984,** *106* (18), 5145-5150.

9. Telford, J. R.; Wittung-Stafshede, P.; Gray, H. B.; Winkler, J. R., Protein Folding Triggered by Electron Transfer. *Accounts of Chemical Research* **1998,** *31* (11), 755-763.

10. Léger, C.; Elliott, S. J.; Hoke, K. R.; Jeuken, L. J. C.; Jones, A. K.; Armstrong, F. A., Enzyme Electrokinetics: Using Protein Film Voltammetry To Investigate Redox Enzymes and Their Mechanisms. *Biochemistry* **2003,** *42* (29), 8653-8662.

11. Kwan, P.; McIntosh, C. L.; Jennings, D. P.; Hopkins, R. C.; Chandrayan, S. K.; Wu, C.-H.; Adams, M. W. W.; Jones, A. K., The [NiFe]-Hydrogenase of Pyrococcus furiosus Exhibits a New Type of Oxygen Tolerance. *J. Am. Chem. Soc.* **2015,** *137* (42), 13556-13565.

12. Armstrong, F. A.; Evans, R. M.; Hexter, S. V.; Murphy, B. J.; Roessler, M. M.; Wulff, P., Guiding Principles of Hydrogenase Catalysis Instigated and Clarified by Protein Film Electrochemistry. *Accounts of Chemical Research* **2016,** *49* (5), 884-892.

13. Greene, B. L.; Joseph, C. A.; Maroney, M. J.; Dyer, R. B., Direct Evidence of Active-Site Reduction and Photodriven Catalysis in Sensitized Hydrogenase Assemblies. *J. Am. Chem. Soc.* **2012,** *134* (27), 11108-11111.

14. Pandey, A.; Guyot-Sionnest, P., Slow Electron Cooling in Colloidal Quantum Dots. *Science* **2008,** *322* (5903), 929-932.

15. Jeong, K. S.; Guyot-Sionnest, P., Mid-Infrared Photoluminescence of CdS and CdSe Colloidal Quantum Dots. *ACS Nano* **2016,** *10* (2), 2225-2231.

16. Zhu, H.; Song, N.; Lv, H.; Hill, C. L.; Lian, T., Near Unity Quantum Yield of Light-Driven Redox Mediator Reduction and Efficient H2 Generation Using Colloidal Nanorod Heterostructures. *J. Am. Chem. Soc.* **2012,** *134* (28), 11701-11708.

17. Zhu, H.; Song, N.; Rodríguez-Córdoba, W.; Lian, T., Wave Function Engineering for Efficient Extraction of up to Nineteen Electrons from One CdSe/CdS Quasi-Type II Quantum Dot. *J. Am. Chem. Soc.* **2012,** *134* (9), 4250-4257.

18. Hoffmann, M.-C.; Müller, A.; Fehringer, M.; Pfänder, Y.; Narberhaus, F.; Masepohl, B., Coordinated Expression of fdxD and Molybdenum Nitrogenase Genes Promotes Nitrogen Fixation by Rhodobacter capsulatus in the Presence of Oxygen. *J. Bacteriol.* **2014,** *196* (3), 633-640.

19. Gallon, J. R., The oxygen sensitivity of nitrogenase: a problem for biochemists and micro-organisms. *Trends in Biochemical Sciences* **1981,** *6*, 19-23.

20. Reda, T.; Plugge, C. M.; Abram, N. J.; Hirst, J., Reversible interconversion of carbon dioxide and formate by an electroactive enzyme. *Proc. Natl. Acad. Sci.* **2008,** *105* (31), 10654-10658.

21. Wakerley, D. W.; Reisner, E., Oxygen-tolerant proton reduction catalysis: much O2 about nothing? *Energy. Environ. Sci.* **2015,** *8* (8), 2283-2295.

22. Kubas, A.; Orain, C.; De Sancho, D.; Saujet, L.; Sensi, M.; Gauquelin, C.; Meynial-Salles, I.; Soucaille, P.; Bottin, H.; Baffert, C.; Fourmond, V.; Best, R. B.; Blumberger, J.; Léger, C., Mechanism of O2 diffusion and reduction in FeFe hydrogenases. *Nat. Chem.* **2017,** *9* (1), 88-95.

23. Jones, A. K.; Lamle, S. E.; Pershad, H. R.; Vincent, K. A.; Albracht, S. P. J.; Armstrong, F. A., Enzyme Electrokinetics: Electrochemical Studies of the Anaerobic Interconversions between Active and Inactive States of Allochromatium vinosum [NiFe]-hydrogenase. *J. Am. Chem. Soc.* **2003,** *125* (28), 8505-8514.

24. Bleijlevens, B.; van Broekhuizen, F. A.; De Lacey, A. L.; Roseboom, W.; Fernandez, V. M.; Albracht, S. P. J., The activation of the [NiFe]-hydrogenase from Allochromatium vinosum. An infrared spectro-electrochemical study. *J Biol Inorg Chem* **2004,** *9* (6), 743-752.

25. Vincent, K. A.; Parkin, A.; Lenz, O.; Albracht, S. P. J.; Fontecilla-Camps, J. C.; Cammack, R.; Friedrich, B.; Armstrong, F. A., Electrochemical Definitions of O2 Sensitivity and Oxidative Inactivation in Hydrogenases. *J. Am. Chem. Soc.* **2005,** *127* (51), 18179-18189.

26. Pandelia, M.-E.; Nitschke, W.; Infossi, P.; Giudici-Orticoni, M.-T.; Bill, E.; Lubitz, W., Characterization of a unique [FeS] cluster in the electron transfer chain of the oxygen tolerant [NiFe] hydrogenase from Aquifex aeolicus. *Proc. Natl. Acad. Sci.* **2011,** *108* (15), 6097-6102.

27. Horch, M.; Lauterbach, L.; Mroginski, M. A.; Hildebrandt, P.; Lenz, O.; Zebger, I., Reversible Active Site Sulfoxygenation Can Explain the Oxygen Tolerance of a NAD+-Reducing [NiFe] Hydrogenase and Its Unusual Infrared Spectroscopic Properties. *J. Am. Chem. Soc.* **2015,** *137* (7), 2555-2564.

28. Berndt, C.; Lillig, C. H.; Flohé, L., Redox regulation by glutathione needs enzymes. *Front. Pharmacol.* **2014,** *5*.

29. Li, X.-B.; Li, Z.-J.; Gao, Y.-J.; Meng, Q.-Y.; Yu, S.; Weiss, R. G.; Tung, C.-H.; Wu, L.-Z., Mechanistic Insights into the Interface-Directed Transformation of Thiols into Disulfides and Molecular Hydrogen by Visible-Light Irradiation of Quantum Dots. *Angew. Chem., Int. Ed.* **2014,** *53* (8), 2085-2089.

30. Martindale, B. C. M.; Joliat, E.; Bachmann, C.; Alberto, R.; Reisner, E., Clean Donor Oxidation Enhances the H2 Evolution Activity of a Carbon Quantum Dot–Molecular Catalyst Photosystem. *Angew. Chem., Int. Ed.* **2016,** *55* (32), 9402-9406.

31. Mira, D.; Brunk, U.; Boveris, A.; Cadenas, E., One-electron transfer reactions of diquat radical to different reduction intermediates of oxygen. *Free Radical Biology and Medicine* **1988,** *5* (3), 155-163.

32. Imlay, J. A., Iron-sulphur clusters and the problem with oxygen. *Molecular Microbiology* **2006,** *59* (4), 1073-1082.

33. Misra, H. P.; Fridovich, I., The Generation of Superoxide Radical during the Autoxidation of Ferredoxins. *J. Biol. Chem.* **1971,** *246* (22), 6886-6890.

34. Horch, M.; Lauterbach, L.; Saggu, M.; Hildebrandt, P.; Lendzian, F.; Bittl, R.; Lenz, O.; Zebger, I., Probing the Active Site of an O2-Tolerant NAD+-Reducing [NiFe]-Hydrogenase from Ralstonia eutropha H16 by In Situ EPR and FTIR Spectroscopy. *Angew. Chem., Int. Ed.* **2010,** *49* (43), 8026-8029.

35. Greene, B. L.; Wu, C.-H.; Vansuch, G. E.; Adams, M. W. W.; Dyer, R. B., Proton Inventory and Dynamics in the Nia-S to Nia-C Transition of a [NiFe] Hydrogenase. *Biochemistry* **2016,** *55* (12), 1813-1825.

36. Kao, Y.-T.; Saxena, C.; He, T.-F.; Guo, L.; Wang, L.; Sancar, A.; Zhong, D., Ultrafast Dynamics of Flavins in Five Redox States. *J. Am. Chem. Soc.* **2008,** *130* (39), 13132-13139.

37. Krämer, T.; Kampa, M.; Lubitz, W.; van Gastel, M.; Neese, F., Theoretical Spectroscopy of the NiII Intermediate States in the Catalytic Cycle and the Activation of [NiFe] Hydrogenases. *ChemBioChem* **2013,** *14* (14), 1898-1905.

38. Volbeda, A.; Martin, L.; Barbier, E.; Gutiérrez-Sanz, O.; De Lacey, A. L.; Liebgott, P.-P.; Dementin, S.; Rousset, M.; Fontecilla-Camps, J. C., Crystallographic studies of [NiFe]-hydrogenase mutants: towards consensus structures for the elusive unready oxidized states. *J. Biol. Inorg. Chem.* **2015,** *20* (1), 11-22.

39. Abou Hamdan, A.; Burlat, B.; Gutiérrez-Sanz, O.; Liebgott, P.-P.; Baffert, C.; De Lacey, A. L.; Rousset, M.; Guigliarelli, B.; Léger, C.; Dementin, S., O_2-independent formation of the inactive states of NiFe hydrogenase. *Nat Chem Biol* **2013,** *9* (1), 15-17.

40. Breglia, R.; Ruiz-Rodriguez, M. A.; Vitriolo, A.; Gonzàlez-Laredo, R. F.; De Gioia, L.; Greco, C.; Bruschi, M., Theoretical insights into [NiFe]-hydrogenases oxidation resulting in a slowly reactivating inactive state. *J Biol Inorg Chem* **2017,** *22* (1), 137-151.

Chapter 5

Charge Transfer in Cytochrome C-Quantum Rod Conjugates

5.1 - Introduction

Protein-nanoparticle hybrid systems engaging in interfacial charge transfer reactions have found important roles in understanding and development of systems for light harvesting and energy conversion.[1-3] Understanding how the protein framework and interactions with nanoparticle surfaces control properties such as the efficiency of charge transfer[4] and stability are critical for rational optimization of these systems. Understanding these interactions with proteins as well as other classes of molecules is an important component in designing and increasing the efficiency of solar fuel producing systems relying on charge transfer across interfaces to operate.[1, 5-8]

Cytochrome c (CytC) is an important electron transfer protein in the mitochondria of eukaryotic organisms where it plays critical roles in oxidative phosphorylation and apoptosis. It has also served as a paradigm for understanding mechanisms of electron transfer in biological and hybrid bio-inorganic systems owing to its many remarkable properties.[9-11] It is highly robust, small, hydrophilic and expresses well in yeast and e-coli. The remarkable optical properties of the prosthetic c-type heme group provide many useful spectral handles for experimentalists to interrogate the state of the protein with a variety of physical methods.

We set out to design a system incorporating cytochrome c with semiconductor nanocrystals as a model to understand interfacial photo-induced electron transfer and how it could be manipulated through engineering of the protein structure and the nanoparticle surface chemistry. Formation of electron transfer complexes of CytC with its native redox partners is largely controlled by electrostatic interactions between the highly charged basic patches localized at the heme periphery in CytC and acidic patches on its

redox partner protiens.[12] Figure 5.1a shows the structure of yeast iso-1-cytochrome c and panel b presents the structure with a surface rendered around any His, Lys and Arg residues, highlighting the basic region surrounding the exposed edge of the prosthetic heme group that guides electron transfer reactions.

The highly positively charged CytC and its engineered binding site suggest a strategy for promoting electron transfer with semiconductor nanoparticles. Interactions with nanoparticles with anionic surface ligands has proven a viable strategy for promoting self-assembly of nanocrystals and redox active proteins such as [FeFe] hydrogenases[1, 5, 13] into electron transfer active geometric configurations.[8] An alternative strategy for promoting efficient charge transfer interactions between a nanoparticle surface and a protein is the incorporation of linker groups to anchor the protein to the

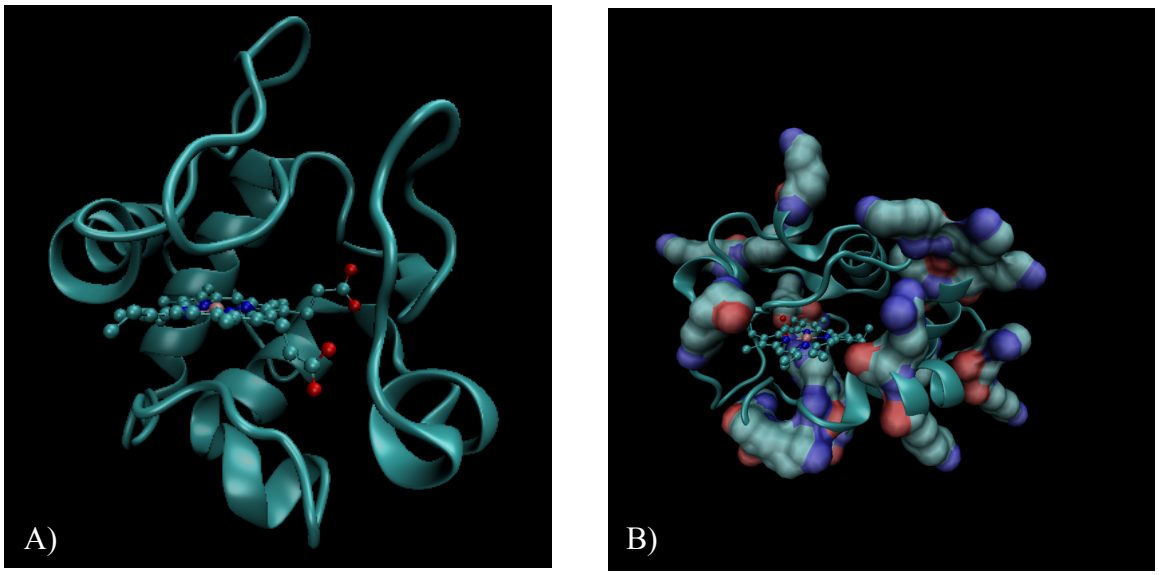

Figure 5.1 – Structure and properties of CytC A) Crystal Structure of iso-1-cytochrome c from *Saccharomyces cerevisiae* (PDB code: 1YCC). B) Structure of iso-1-cytochrome c with the basic residues rendered as surfaces. Color scheme of the surface denotes atom type. Blue: nitrogen; red: oxygen and teal regions: carbon

nanoparticle surface via coordinative or covalent bonds. The latter approach can generally be partitioned into two categories. One aspect is the incorporation of unnatural linkers through synthetic modification of amino acid side chains or protein cofactors, for example, functionalization of free amines or thiols with alkylating agents or introduction of a synthetic heme with a linker group included.[14] Alternatively, modification of the protein sequence itself through mutagenesis can provide linkers through appropriately placed reactive side chains. Incorporation of surface exposed cysteine, for example, could bind a wide range of substrates including gold and semiconductor surfaces and the histidine tag, included in many cases to increase ease of purification has strong interactions with metal and semiconductor surfaces.[15]

5.2 – Results and Discussion

5.2.1 – Reduction Potential Control Through Heme Ligation

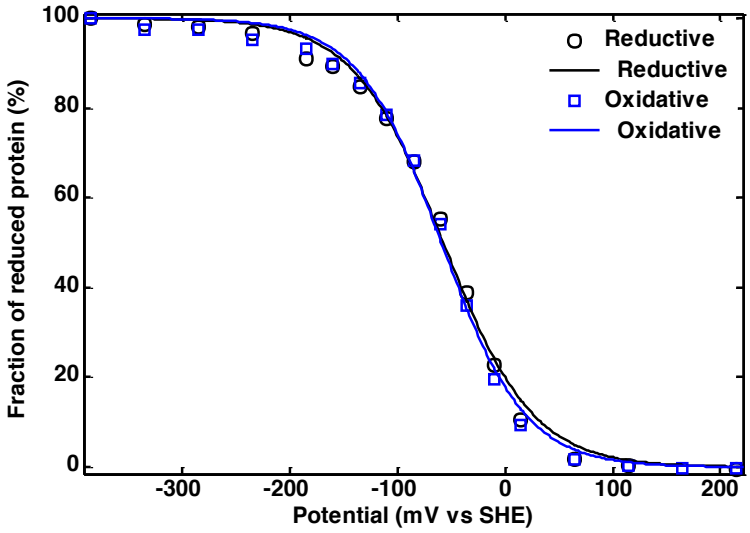

Figure 5.2 – Spectroelectrochemical measurement of the M80C reduction potential at pH = 7.

Unfortunately, there was a significant obstacle to the intended scheme of studying photo-induced electron transfer from the nanoparticle to a model redox protein. The reduction potential of the ferric to ferrous transition in wild type CytC is +290 mV vs NHE which is positive enough to spontaneously oxidize the ligands on the nanoparticle surface,[16] meaning that the Fe(III) state is not stable on the nanoparticle surface. We thus turned to site directed mutagenesis to shift the CytC reduction potential to a more tractable value. A wide range of interrelated factors control the reduction potentials of metalloproteins, with heme containing proteins in particular spanning a range from nearly - 400 mV to + 350mV vs. NHE.[17] The major determinant, however, is the nature of the axial ligation of the heme provided by the protein scaffold[18] which can be changed through site directed mutagenesis. To exploit this property, we obtained mutants of yeast iso-1-cytochrome c from the lab of Dr. Ekaterina Pletneva. We obtained M80C along

with H33C/M80C and E66C/M80C variants which additionally contain surface accessible cysteine residues. Ferric M80C has been reported to exist in two isomeric forms.[18-19] Isomer II results from isolating the protein under oxidizing conditions avoiding the formation of the ferrous state in the presence of oxygen and corresponds to a thiolate ligated state. Reduction and reoxidation of M80C in open air or isolation under reducing conditions results in the formation of a different ferric state dubbed isomer I. Those set of observations suggest that isomer I forms through oxidative damage to Cys 80 by activation of oxygen of the ferrous heme which blocks the ability to reform isomer II through cysteine oxygenation.[20] We received and used the M80C as isomer II, which has a reported reduction potential of -65 mV vs SHE.[18] Figure 5.2 shows a spectroelectrochemical measurement of the M80C reduction potential which yielded values of -57± 5 mV and -59 ± 4 mV vs SHE for reductive and oxidative directions respectively, consistent with the literature value.[18]

5.2.2 – Photoreduction of M80C

With the M80C mutant in hand it became possible to assess its interaction with semiconductor nanoparticles. We used glutathione stabilized CdSe/CdS dot-in-rod (DIR) particles in this study. Figure 5.3 shows the optical absorption spectrum of the ferric M80C protein and the spectral changes over time upon mixing with 50 nM CdSe/CdS DIR in the absence of photoexcitation of DIR. We find that ferric M80C does not oxidize the ligands at the surface of the DIR. Thus, the change in the axial ligation of CytC

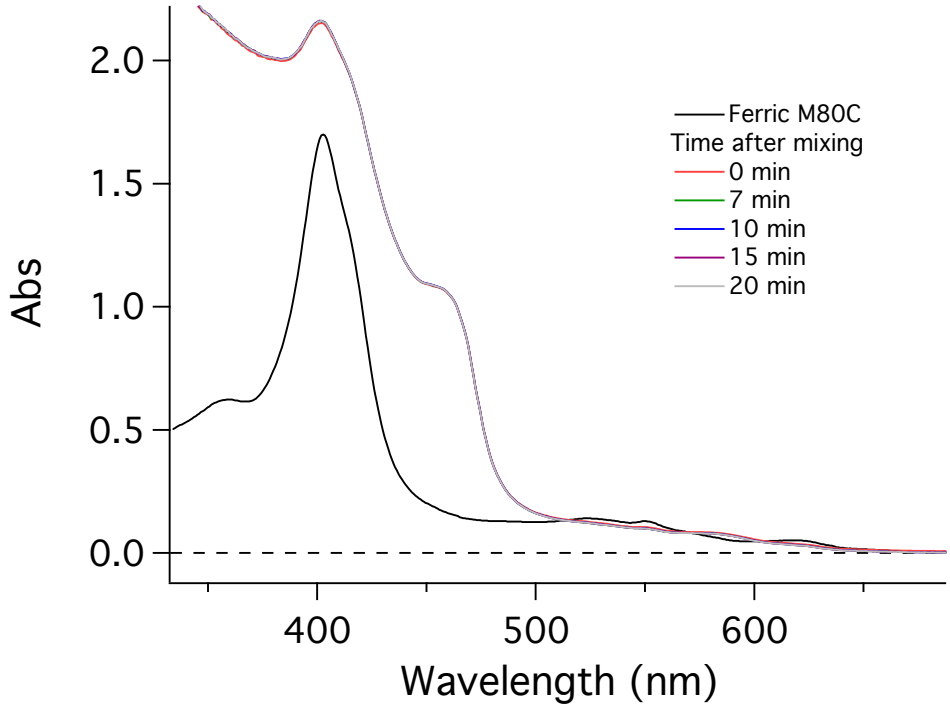

Figure 5.3 – M80C stability on DIR surfaces UV-Vis spectral characterization of ferric M80C CytC and mixing of M80C CytC with DIR in the dark.

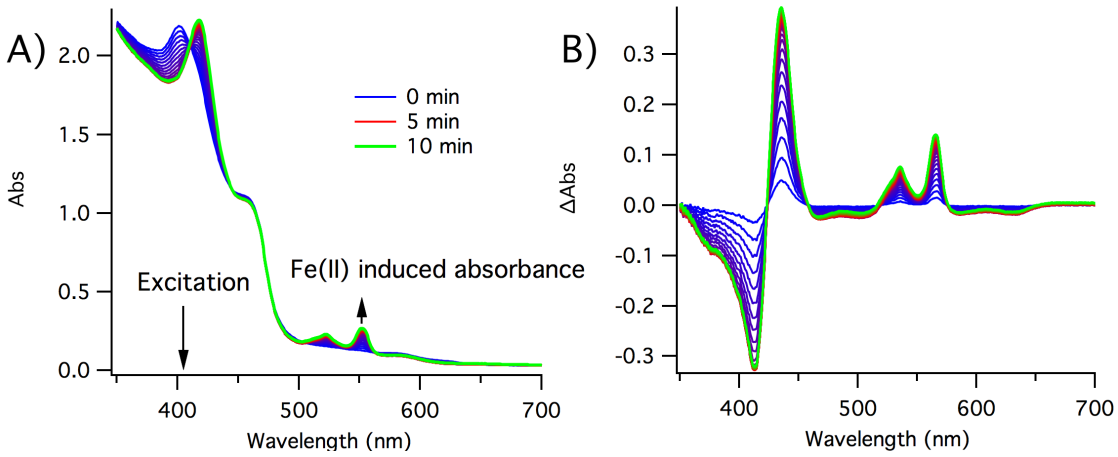

Figure 5.4 – Photoreduction of ferric M80C by photoexcitation of DIR structures. A) UV-Vis spectra following the photoreduction B) Difference spectra of the photoreduction process.

achieved the goal of sufficiently lowering the reduction potential of the heme to confer stability to ferric M80C on the DIR surface.

We then investigated the possibility of photo-induced electron transfer from DIR to M80C. UV-vis spectra in tandem with excitation of the sample with a 405nm laser diode is shown in Figure 5.4. Smooth conversion from ferric to ferrous M80C was observed consistent with photo-induced electron transfer from the DIR to M80C heme. With this observation in hand, we investigated the effect different methods of enforcing the DIR –M80C interaction would have on this charge transfer process. The CytC mutants M80C/H33C and M80C/E66C have surface accessible cysteine residues at different locations on the protein structure. Figure 5.5 shows the CytC cartoon ribbon structure along with the positions of the H33 and E66 residues. H33 is positioned on a loop near the exposed heme crevice, while E66 is positioned on a helix on the other side of the protein from the exposed heme crevice site. The cysteine mutants allow direct

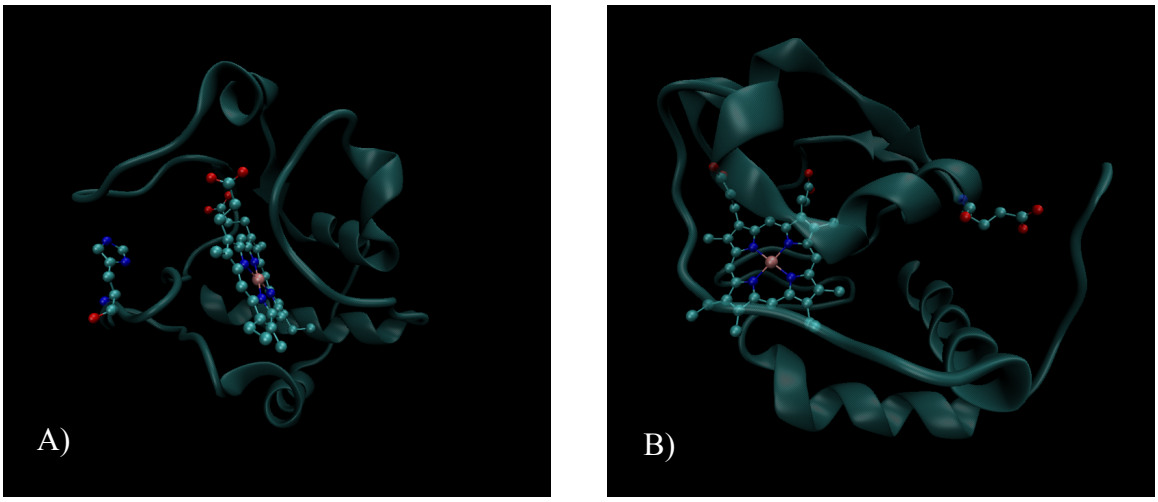

Figure 5.5 – Structure of iso-1 CytC showing the position of the mutated residues A) His 33 and B) Glu 66 and their positions relative to the heme group.

attachment of the protein in different orientations to the semiconductor surface by forming a covalent Cd-S bond. Thus, it is possible to observe this photoreduction process as a function of differing orientation of the CytC on the nanoparticle surface which may have a strong effect on the forward or reverse rates of the charge transfer processes as well as affect the stability of the structures overall.[21-22]

Photoreduction of the three mutants is shown in Figure 5.6 on three samples, prepared identically except for the identity of the mutant. The photoreduction is probed by following the change in absorbance of the ferric heme band at 403 nm as a function of time. Photoexcitation is carried out for 600 seconds and then turned off and subsequent spectral changes in the sample were continuously probed. These experiments were all performed under anaerobic conditions.

The behavior of the initial photoreduction process shows a strong dependence on covalent vs. electrostatic attachment. Interestingly, for the case of covalent attachment, the amount of protein reduced saturates before all the protein in the sample has been

reduced while for the electrostatically bound case the reduction process essentially goes to completion. This suggests that the covalently linked CytC on the particle surface has formed a layer blocking adsorption of additional protein from solution. Since it is covalently attached, the reduced protein cannot desorb to allow adsorption of an oxidized CytC from solution. The electrostatically bound case allows for the photo-reduced proteins to desorb from the particle surface and dynamically exchange with proteins in solution. Indeed, this process may be favored by a change in Fe oxidation state from 3+ to 2+ slightly lowering the affinity of the protein for the anionic nanoparticle surface. The initial rate of photo-reduction also shows dependence on the mode of attachment to the particle. Linear fits to the first 50 seconds of photoreduction give rates of 405 ± 8 μOD s^{-1}, 369 ± 7 μOD s^{-1} and 219 ± 11 μOD s^{-1} for E66C, H33C and M80C respectively. The efficiency of photoreduction is not particularly high, owing to the need for the photo-excited electron to tunnel through the glutathione ligand shell and the protein matrix within in competition with the rapid exciton localization and recombination processes in these nanostructures (see Chapter 3.2.2). Clearly covalent attachment facilitates more efficient reduction at early illumination times, however this rate rapidly falls off as ferric protein is depleted at the particle surface. There may be some significance to the difference in initial rate between H33C and E66C, however, this data set is not enough to confirm if the difference is significant given the relative similarity of the rates.

After photo-excitation of the sample ceases, the reduced protein begins to recover to the ferric state in a manner that depends strongly on the nature of the interaction with the DIR surface. Recovery rates were fit to an exponential process to compare their

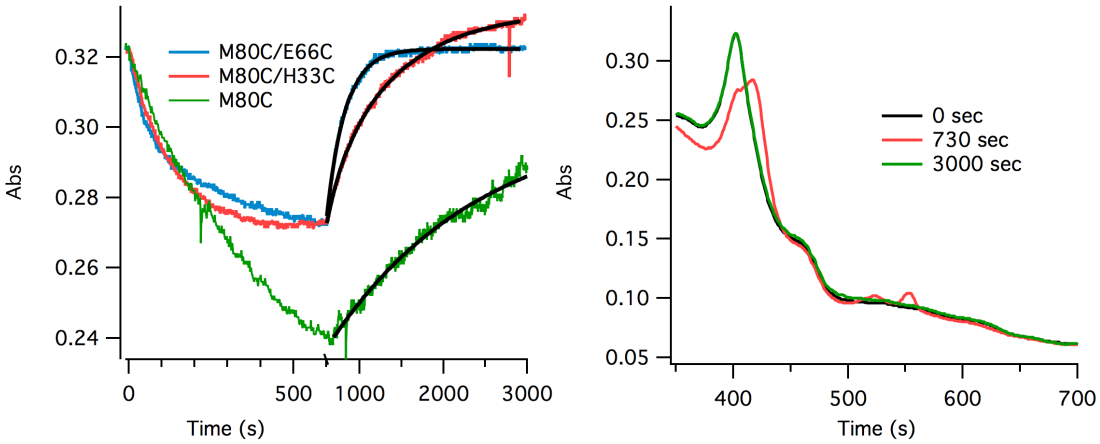

Figure 5.6 – Photoreduction of M80C mutants by photoexcitation of DIR structures probed by A) absorbance change at 403 nm. Excitation beam on from 1-600 seconds and then switched off. The time axis has a compressed linear scaling between 600 and 3000 seconds for ease of viewing. B) Typical changes in optical spectra for the samples in A) E66C is shown.

timescales. Notable, the recovery for both M80C and E66C were well fit by single exponential processes with lifetimes of 1808 ± 20 s and 223 ± 0.6 s respectively while the H33C recovery required two exponentials with 23% having 210 ± 11 s lifetime and 77% having 923 ± 75 s lifetime. At least part of the recovery of H33C is due to time dependent aggregation of the sample after photoreduction which is evident from the 403 nm absorbance trace since it crosses over to a value higher than it started at in the fully oxidized state. This is due to a rising baseline from aggregation induced scattering. Interestingly, E66C smoothly recovers to its starting value and it is evident from the spectra that there is no significant baseline shift from beginning to end of the experiment. It is not clear what causes this large disparity between the two covalent binding sites and the loss of colloidal stability in H33C. It may be that binding through the cysteine of

H33C destabilizes the protein structure although it might be expected to see a stronger response in the heme spectrum if, for example, H33C unfolded on the DIR surface. Of all the mutants, E66C seems to show the highest rates for both photoreduction and reoxidation processes as well as much greater stability than the H33C variant. The reoxidation process in the M80C variant was much slower than either of the cysteine bound variants. This suggests that the reoxidation is a process that takes place on the nanoparticle surface and like the photoreduction process for M80C it is also dependent on the adsorption/desorption equilibrium with unbound protein.

The nature of the reoxidation process has not yet been entirely revealed. It is interesting that it takes place at all. The typical fate of oxidizing equivalents in a system where electrons have been transferred to an acceptor is hole transfer to surface bound thiolate ligands and coupling of the so-formed thyil radicals on the surface to yield disulfides.[23] Once disulfides have formed it is difficult to image that they may be reduced by the ferrous heme as they are quite inert and typically require strong reducing agents to transform to sulfides. It is possible that in this system disulfide coupling is slow and thyil radicals or other intermediate remained trapped on the nanoparticle surfaces which may then slowly recombine with the ferrous heme. Surface species on quantum dot surfaces can also participate in redox chemistry and show noninnocent behavior.[24-25]

5.3 - Conclusions

Through these studies, we have designed a system for understanding the effects orientation of a redox protein on a quantum dot surface has on photo-induced charge transfer processes. Control over axial ligation of the heme allowed raising of the protein

reduction potential to enable stability of the ferric state of the protein on the nanoparticle surface. Mutation of surface residues of the protein enabled control of the orientation of the protein on the particle surface. Either through electrostatic interactions with surface ligands or binding directly to surface Cd^{2+} ions via a cysteine donated thiolate. The mutations succeeded in changing the efficiency of photoreduction of the protein and subsequent rate of reoxidation. More work is needed to understand the factors governing stability of this system and uncovering the factors controlling the rates of the forward and reverse charge transfer processes as well as the mechanism responsible for the reoxidation process. Understanding these things has the potential to reveal much about neglected aspects of photocatalytic systems using quantum dots as photosensitizers.

5.4 - References

1. Brown, K. A.; Wilker, M. B.; Boehm, M.; Dukovic, G.; King, P. W., Characterization of Photochemical Processes for H_2 Production by CdS Nanorod–[FeFe] Hydrogenase Complexes. *J. Am. Chem. Soc.* **2012,** *134* (12), 5627-5636.

2. Sakai, T.; Mersch, D.; Reisner, E., Photocatalytic Hydrogen Evolution with a Hydrogenase in a Mediator-Free System under High Levels of Oxygen. *Angew. Chem., Int. Ed.* **2013,** *52* (47), 12313-12316.

3. Hutton, G. A. M.; Reuillard, B.; Martindale, B. C. M.; Caputo, C. A.; Lockwood, C. W. J.; Butt, J. N.; Reisner, E., Carbon Dots as Versatile Photosensitizers for Solar-Driven Catalysis with Redox Enzymes. *J. Am. Chem. Soc.* **2016,** *138* (51), 16722-16730.

4. King, P. W., Designing interfaces of hydrogenase–nanomaterial hybrids for efficient solar conversion. *Biochimica et Biophysica Acta (BBA) - Bioenergetics* **2013,** *1827* (8), 949-957.

5. Greene, B. L.; Joseph, C. A.; Maroney, M. J.; Dyer, R. B., Direct Evidence of Active-Site Reduction and Photodriven Catalysis in Sensitized Hydrogenase Assemblies. *J. Am. Chem. Soc.* **2012,** *134* (27), 11108-11111.

6. Brown, K. A.; Dayal, S.; Ai, X.; Rumbles, G.; King, P. W., Controlled Assembly of Hydrogenase-CdTe Nanocrystal Hybrids for Solar Hydrogen Production. *J. Am. Chem. Soc.* **2010,** *132* (28), 9672-9680.

7. Brown, K. A.; Harris, D. F.; Wilker, M. B.; Rasmussen, A.; Khadka, N.; Hamby, H.; Keable, S.; Dukovic, G.; Peters, J. W.; Seefeldt, L. C.; King, P. W., Light-driven dinitrogen reduction catalyzed by a CdS:nitrogenase MoFe protein biohybrid. *Science* **2016,** *352* (6284), 448-450.

8. Hwang, E. T.; Orchard, K. L.; Hojo, D.; Beton, J.; Lockwood, C. W. J.; Adschiri, T.; Butt, J. N.; Reisner, E.; Jeuken, L. J. C., Exploring Step-by-Step Assembly of Nanoparticle:Cytochrome Biohybrid Photoanodes. *ChemElectroChem* **2017**.

9. Telford, J. R.; Wittung-Stafshede, P.; Gray, H. B.; Winkler, J. R., Protein Folding Triggered by Electron Transfer. *Accounts of Chemical Research* **1998,** *31* (11), 755-763.

10. Gray, H. B.; Winkler, J. R., Electron Transfer in Proteins. *Annual Review of Biochemistry* **1996,** *65* (1), 537-561.

11. Winkler, J. R.; Gray, H. B., Electron Flow through Metalloproteins. *Chem. Rev.* **2014,** *114* (7), 3369-3380.

12. Williams, P. A.; Fulop, V.; Leung, Y.-C.; Chan, C.; Moir, J. W. B.; Howlett, G.; Ferguson, S. J.; Radford, S. E.; Hajdu, J., Pseudospecific docking surfaces on electron transfer proteins as illustrated by pseudoazurin, cytochrome c550 and cytochrome cd1 nitrite reductase. *Nat Struct Mol Biol* **1995,** *2* (11), 975-982.

13. Brown, K. A.; Wilker, M. B.; Boehm, M.; Hamby, H.; Dukovic, G.; King, P. W., Photocatalytic Regeneration of Nicotinamide Cofactors by Quantum Dot–Enzyme Biohybrid Complexes. *ACS Catal.* **2016,** *6* (4), 2201-2204.

14. Onoda, A.; Himiyama, T.; Ohkubo, K.; Fukuzumi, S.; Hayashi, T., Photochemical properties of a myoglobin-CdTe quantum dot conjugate. *Chem. Commun.* **2012,** *48* (65), 8054-8056.

15. Aldeek, F.; Safi, M.; Zhan, N.; Palui, G.; Mattoussi, H., Understanding the Self-Assembly of Proteins onto Gold Nanoparticles and Quantum Dots Driven by Metal-Histidine Coordination. *ACS Nano* **2013,** *7* (11), 10197-10210.

16. Gerhards, C.; Schulz-Drost, C.; Sgobba, V.; Guldi, D. M., Conjugating Luminescent CdTe Quantum Dots with Biomolecules†. *The Journal of Physical Chemistry B* **2008,** *112* (46), 14482-14491.

17. Liu, J.; Chakraborty, S.; Hosseinzadeh, P.; Yu, Y.; Tian, S.; Petrik, I.; Bhagi, A.; Lu, Y., Metalloproteins Containing Cytochrome, Iron–Sulfur, or Copper Redox Centers. *Chem. Rev.* **2014,** *114* (8), 4366-4469.

18. Wallace, C. J.; Clark-Lewis, I., Functional role of heme ligation in cytochrome c. Effects of replacement of methionine 80 with natural and non-natural residues by semisynthesis. *J. Biol. Chem.* **1992,** *267* (6), 3852-3861.

19. Smulevich, G.; Bjerrum, M. J.; Gray, H. B.; Spiro, T. G., Resonance raman spectra and the active site structure of semisynthetic Met80Cys horse heart cytochrome c. *Inorganic Chemistry* **1994,** *33* (21), 4629-4634.

20. Wang, Z.; Ando, Y.; Nugraheni, A. D.; Ren, C.; Nagao, S.; Hirota, S., Self-oxidation of cytochrome c at methionine80 with molecular oxygen induced by cleavage of the Met-heme iron bond. *Molecular BioSystems* **2014,** *10* (12), 3130-3137.

21. Aubin-Tam, M.-E.; Hwang, W.; Hamad-Schifferli, K., Site-directed nanoparticle labeling of cytochrome c. *Proc. Natl. Acad. Sci.* **2009,** *106* (11), 4095-4100.

22. Valušová, E.; Švec, P.; Antalík, M., Structural and thermodynamic behavior of cytochrome c assembled with glutathione-covered gold nanoparticles. *J Biol Inorg Chem* **2009,** *14* (4), 621-630.

23. Li, X.-B.; Li, Z.-J.; Gao, Y.-J.; Meng, Q.-Y.; Yu, S.; Weiss, R. G.; Tung, C.-H.; Wu, L.-Z., Mechanistic Insights into the Interface-Directed Transformation of Thiols into

Disulfides and Molecular Hydrogen by Visible-Light Irradiation of Quantum Dots. *Angew. Chem., Int. Ed.* **2014,** *53* (8), 2085-2089.

24. Tsui, E. Y.; Hartstein, K. H.; Gamelin, D. R., Selenium Redox Reactivity on Colloidal CdSe Quantum Dot Surfaces. *J. Am. Chem. Soc.* **2016,** *138* (35), 11105-11108.

25. Braten, M. N.; Gamelin, D. R.; Mayer, J. M., Reaction Dynamics of Proton Coupled Electron Transfer from Reduced ZnO Nanocrystals. *ACS Nano* **2015**.

26. Greene, B. L.; Wu, C.-H.; McTernan, P. M.; Adams, M. W. W.; Dyer, R. B., Proton-Coupled Electron Transfer Dynamics in the Catalytic Mechanism of a [NiFe]-Hydrogenase. *J. Am. Chem. Soc.* **2015,** *137* (13), 4558-4566.

27. Kwan, P.; McIntosh, C. L.; Jennings, D. P.; Hopkins, R. C.; Chandrayan, S. K.; Wu, C.-H.; Adams, M. W. W.; Jones, A. K., The [NiFe]-Hydrogenase of Pyrococcus furiosus Exhibits a New Type of Oxygen Tolerance. *J. Am. Chem. Soc.* **2015,** *137* (42), 13556-13565.

Chapter 6

Conclusions

6.1 - Conclusion

Assembly and characterization of redox protein-DIR complexes has been exploited in a wide range of areas in this work. Through control of the energetic landscape experienced by photoexcited electrons, a highly efficient and robust photocatalytic system for hydrogen production was realized in Chapter 3. This system showed quantum yields of up to 77% for hydrogen production, an unprecedented efficiency in photochemically driven hydrogenases systems. Better than 10^6 turnovers over the course of 16 days demonstrated the high stability of the catalyst and photosensitizer and the innocent nature of the sacrificial electron donating redox couple.

Time resolved spectroscopic techniques revealed the mechanistic underpinnings of the high efficiency of mediator photoreduction. While extraction of additional free energy by PDQ^{2+}, as compared to MV^{2+}, did result in slower photo induced electron transfer in the former case, it was still able to quantitatively outcompete exciton recombination resulting in unity yield of electron injection into PDQ^{2+}. Subsequent recombination dynamics were also more rapid in the case of ET to PDQ^{2+}, however the charge separation lifetime was still substantially longer than the measured hole extraction time resulting in equal steady state photoreduction efficiency to MV^{2+} photoreduction.

Subsequent work focused on using this novel photochemical system to perform photo-triggered mechanistic studies on *Pf* SHI. Previous results on sub-TOF dynamics of the SHI active site using pump-probe nanoseconds visible and infrared spectroscopy were reproduced, demonstrating that the nanoparticle sensitized system provides a viable method for triggering enzyme dynamics while achieving larger electrochemical potential jumps than had been previously possible.

The utility of the photochemical system as a novel method for reductively activating aerobically inactivated SHI was also demonstrated. This generated insight into the nature of the inactive states of SHI not possible in reported protein film voltammetry experiments. Three inactive states were assigned to specific infrared resonances and two were confirmed to be rapidly reactivating and sit at lower reduction potentials than analogous states in standard oxygen tolerant [NiFe] H_2ases and a third state was assigned to a slowly reactivating state with a sulfoxygenated active site. These results demonstrate the power and versatility of the technique and suggest that it will have a wide range of applicability in other enzyme and catalysts systems.

The concept of metalloproteins-DIR complexes was further explored using CytC mutants as a model system. Stable DIR-CytC complex formation was enabled by control over the axial heme ligation in a M80C variant of CytC. Site directed mutagenesis was further exploited to engineer specific M80C-DIR contacts via introduction of surface cysteines. We then found strong evidence that both photoreduction efficiency and subsequent charge recombination rate were strongly perturbed by changes in the surface interaction between M80C and DIR. This provides a platform for understanding the effects of orientation on charge transfer dynamics in hybrid protein-nanoparticle constructs as well as the chemical nature of surface confined oxidizing equivalents in these systems subsequent to electron transfer.